Evidence for Top Quark Production in $\bar{p}p$ Collisions at $\sqrt{s} = 1.8$ TeV

by

Gordon Thomas Watts

Submitted in Partial Fulfillment
of the
Requirements for the Degree

Doctor of Philosophy

Supervised by

Professor Paul Tipton

Department of Physics and Astronomy
The College
Arts and Sciences

University of Rochester

Rochester, New York

1994

Curriculum Vitae

The author was born in Boston, Massachusetts on July 22, 1966. He attended the University of Texas from 1984 to 1989, and graduated with a Bachelor of Science degree in Physics and Math in 1989. He came to the University of Rochester in the fall of 1989 and began graduate studies in physics. He received a Department of Education fellowship in the years 1989-1992. He pursued his research in high energy physics under the direction of Professor Paul Tipton, and received the Master of Arts degree in Spring of 1991.

Acknowledgements

Although this thesis has one name on it, its existence is possible only because of the help and support of many people. I would like to thank the entire CDF Rochester group for their valuable advice and support, and in particular my advisor Paul Tipton for keeping me on the path that leads from student to physicist. Thanks to Brian Winer and Richard Hughes who kept this analysis on track, and thanks to Phil Koehn and Kirsten Tollefson for their support. I would also like to thank the rest of the CDF collaboration for their helpful comments and aid, and the Fermilab staff for running the accelerator so well. I would like to thank my friends on the 7:10 express train for their help in reminding me there is more to life than physics. Finally, my thanks go to my parents for their support and encouragement and for putting up with missed holidays.

Abstract

We present the results of a search for the top quark in 19.3 pb^{-1} of $p\bar{p}$ collisions at $\sqrt{s} = 1.8$ TeV. The data were collected using the Collider Detector at Fermilab (CDF). We search for $t\bar{t}$ production in the final states e+ν+jets and μ+ν+jets. We require at least three high energy jets in the event as a way of reducing the QCD W background. One of the three or more jets is required to contain a secondary vertex, indicating the possible presence of a b quark from a t-quark decay. The efficiency of the secondary-vertex b-quark tag is measured and the $t\bar{t}$ acceptance is estimated. We estimate approximately 85% of the background directly from data, and use a Monte Carlo calculation to verify the result. The remaining backgrounds are estimated using a combination of Monte Carlo calculations and data. We find six events in the data, with a background of 2.3±0.3 events. The probability of the background fluctuating up to the observed six events is 3.2%. Two other top searches performed by CDF, a second b-quark tagging method similar to the one described above, and a search looking for the $t\bar{t}$-final states $\ell\ell\nu\bar{\nu}$ (where ℓ is an e or a μ) are briefly described. The probability that the combined excess of the three searches is due to background is 0.26%. The statistics are too limited to firmly establish the existence of the top quark. Assuming the excess is due to $t\bar{t}$ production, the $t\bar{t}$ cross section and t-quark mass are estimated.

Contents

1 Theory **1**

1.1 Introduction 1

1.2 The Standard Model 3

1.3 Proton-Antiproton Collisions 7

1.4 Top Quark Production and Decay 9

1.5 Bottom Quark Decay 12

1.6 Overview of the Analysis 15

2 The Collider Detector At Fermilab **17**

2.1 The Tevatron 17

2.2 The CDF Detector 21

2.2.1 The Tracking Detectors 21

2.2.2 The Calorimeters 27

2.2.3 The Muon Detectors 31

2.2.4 The Silicon Vertex Detector 33

2.2.5 The Trigger System 37

2.3 Data Reconstruction 38

3 The Event Samples **43**

3.1 The Generic Jet Sample 44

3.2 The Inclusive Central Electron Sample 45
3.3 High P_T Lepton Identification 49
3.4 The W Sample 51
3.5 The Z Sample 55

4 The b-Tagging Algorithm 58
4.1 The JETVTX Algorithm 61
4.1.1 The $c\tau$ of the JETVTX Tags 69
4.2 The b-tagging Efficiency 71
4.2.1 The Data/Monte Carlo Scale Factor 74
4.3 The $t\bar{t}$ Acceptance 77
4.4 The Tags in the $W+\geq 3$ jet Sample 78

5 The Background Calculation 85
5.1 Mistags, $Wb\bar{b}$, and $Wc\bar{c}$ Backgrounds 86
5.1.1 The Procedure 87
5.1.2 Checks in Control Samples 93
5.1.3 The Tag Rate Parameterization 96
5.1.4 The Monte Carlo Check 99
5.2 The Remaining Backgrounds 107
5.2.1 Wc Contributions 107
5.2.2 Non-W Contributions 108
5.2.3 $Z \rightarrow \tau\tau$ Contributions 110
5.2.4 Diboson Contributions 112
5.3 Summary of the Backgrounds 115

6 Results and Conclusions 117
6.1 The Counting Experiment 117

6.2 Checks in the Z Sample 121

6.3 The $t\bar{t}$ Production Cross Section 122

6.4 Mass Determination of Tagged Events 125

6.5 Conclusion 133

Bibliography **136**

A SVX Cooling and Interlock Subsystems **139**

List of Figures

1.1 The fundamental particles that make up the Standard Model. Quarks and gluons carry color (Red, Green, and Blue), while the leptons, $W^{\pm}$, Z^0, and γ are colorless. The quarks and leptons also have antiparticle counterparts. Interactions between the fermions (quarks and gluons) are mediated by the second group, the bosons ($W^{\pm}$, Z^0, gluons, and γ). 4

1.2 A (a) quark-gluon strong vertex and a (b) gluon-gluon strong vertex. The gluons can interact with themselves, unlike photons, because gluons carry a color charge. The flavor of a quark at a gg vertex will not change, though its color may. 5

1.3 At the Tevatron the most interesting $p\bar{p}$ interactions involve an energetic interaction between a constituent of the proton and one of the antiproton. The remaining partons in the p and $\bar{p}$ are called spectators. The products of the interaction fragment into hadrons, or in the case of the W boson decay, into leptons. 8

1.4 Feynman Diagrams for top production by (a) quark-antiquark annihilation, (b) gluon-gluon fusion, and (c) single top production via W-gluon fusion. W-gluon fusion is not considered here as it is expected to occur at a relatively small rate[9], about one fifth the $t\bar{t}$ production rate. 11

1.5 The P_T distribution for b-quarks from t-quark decays with M_{top}= 160 GeV/c^2. 14

1.6 The Feynman diagram for QCD W-jet production, one of the backgrounds for the top search. 15

2.1 The Tevatron. H^- ions are accelerated by the Cockcroft-Walton and the LINAC to 200 MeV. Bare protons, stripped from the H^- ions, are accelerated by the Booster and injected into the main ring. To make antiprotons, the protons are accelerated to 120 GeV and focused on a copper target. The resulting antiprotons are collected in the accumulator. When enough antiprotons have been collected, both protons and antiprotons are accelerated (separately) in the main ring to 150 GeV and injected into the Tevatron, rotating in opposite directions. There the two beams collide at the B0 and D0 interaction regions. 18

2.2 A schematic layout of the CDF detector, both a side view and perspective view. 22

2.3 The CTC endplate. Each ring is a superlayer. The thicker rings are axial superlayers, the thiner rings are stereo super layers. The slots are the points where wires that exit the chamber are attach to electronics normally mounted on the endplate. The stereo superlayers have 6 wires, and the axial superlayers have 12. 25

2.4 The tower segmentation and calorimeter coverage in $\eta - \phi$ space of the CDF detector. The hatched area has reduced depth coverage because room had to be made for the low beta quadrupole magnets. The solid sections have no coverage at all. 28

2.5 A single Central Calorimeter wedge. There are 12 wedges to an arch, and a total of four arches. The top of the wedge, in this picture, is positioned at the outside of an arch, radially. 30

2.6 One of the two SVX barrels. The barrel is split into 12 pie shaped wedges, and each wedge has four layers. Each layer of each wedge has a ladder on which three silicon detectors are mounted. 34

2.7 One of the 96 ladders in the SVX. The ladders are stacked into four layers, a wedge. 12 wedges make up each of the two barrels of the SVX. 35

2.8 The SVX-CTC track χ^2 for found tracks in data (solid histogram) and in a Monte Carlo simulation (dashed histogram). 40

2.9 The impact parameter (d) resolution for SVX tracks as a function of track's P_T. 41

2.10 The x and y resolutions of a fit primary vertex. 42

3.1 The E_T spectra of the JET50 sample. One jet with E_T>50 GeV or more is required by the trigger in each event. This trigger causes the second peak in the sample. Jets with E_T less than 50 GeV are volunteers in multijet events. 44

3.2 Mass of unlike-sign (solid histogram) and like-sign (points) e-μ pair. Bins below 4 GeV/c^2 are used to determine the number of e-μ pairs due to B hadrons by subtracting the like-sign from the unlike-sign distribution. 48

3.3 The transverse mass distribution for $W \rightarrow e\bar{\nu}$ and $W \rightarrow \mu\bar{\nu}$. . 53

4.1 The Fraction of events passing the W selection criteria in a $t\bar{t}$ Monte Carlo simulation with M_{top}=120 GeV/c^2 (dashed histogram), and a $t\bar{t}$ Monte Carlo simulation with M_{top}=180 GeV/c^2 (solid histogram), as a function of the number of jets in the event, N_{JET}. 59

4.2 Cartoon depicting a t-quark decay. The b-quark fragments, creating a number of tracks, and a B hadron. The B hadron travels a short distance, L_{xy}, before it decays as well. The decay products are used to reconstruct the position of the secondary vertex. 60

4.3 The L_{xy} distribution for B hadrons created by t-decays in ISAJET Monte Carlo generated events. Detector effects are removed. . 61

4.4 The impact parameter, d, distribution for tracks in (a) the JET50 sample, which is not expected to have a large heavy flavor content, and (b) in $t\bar{t}$ Monte Carlo generated events with M_{top}= 160 GeV/c^2. Only tracks from a B hadron decay are shown in the Monte Carlo simulation distribution. 64

4.5 The vertex fit χ^2. All tracks that contribute more than 50 to the vertex χ^2 are removed from the fit. This histogram is made before the χ^2 requirement has been applied. 65

4.6 The JETVTX b-tagging efficiency in $t\bar{t}$ M_{top}=160 GeV/c^2 Monte Carlo simulated events as a function of the b-quark jet E_T. . . 68

4.7 $c\tau_{eff}$ of tags in the Inclusive Central Electron (ICE) sample. . 70

4.8 The E_T of jets in the $t\bar{t}$ ISAJET Monte Carlo simulation (solid histogram) and in ICE data sample (dashed histogram). . . . 76

4.9 The scale factor F^{tag}_{scale} as a function of jet E_T. The systematic uncertainty on F^{tag}_{scale} is calculated by doing a straight-line fit to the data in this plot, and evaluating it at the average jet E_T for jets in $t\bar{t}$ Monte Carlo generated events. 76

4.10 The number of expected $t\bar{t}$ events and number of observed W observed as a function of the jet multiplicity. Note that for ≥ 3 jets, the top signal is still overwhelmed by the W+jet rate. This is why a b-tag is required. 79

4.11 Event display for one of the SVX tagged W+jet events; (a) displays the observed calorimeter E_T in the $\eta - \phi$ plane, (b) shows muon hits in the CMP detector (circular detector just outside the tracking chamber) and CMU detector muon hits (the square detector outside the CMP) as well as the charged tracks found by the CTC. Details of tracks found by the SVX as well as the complete SVX event display are shown in (c). The dashed tracks form the displaced vertex (extraneous tracks have been removed from the enlargement). Track lengths of in the SVX display are proportional to the track's P_T. 83

4.12 The $c\tau_{eff}$ distribution for jets with a secondary-vertex tag in the W+jets data sample (points) compared to b-quark tags from a Monte Carlo simulation (histogram, normalized to data). The shaded histogram represents the tags in the $W+\geq 3$ jet sample. Two tags, with $c\tau_{eff}$ = 1.2 cm and -0.41 cm are not shown. They are a W+2 and a $W+1$ jet event, respectively. 84

5.1 The $c\tau_{eff}$ of the JET50 sample. The JET50 sample does have an appreciable heavy flavor content, though small compared to the ICE sample. The points are the observed tags. The histogram is the sum of $c\bar{c}$, $b\bar{b}$, and background Monte Carlo simulations. The background Monte Carlo generated events contain no long lived particles. The shaded area, $b\bar{b}$ and $c\bar{c}$ contributions, is about 75% of the area under the histogram. Note the $c\tau_{eff}$ distribution of the background Monte Carlo generated tags is symmetric about zero. 88

5.2 The three Feynman diagrams for heavy flavor production in the JET50 data sample, (a) flavor excitation, (b) gluon splitting, and (c) direct $b\bar{b}$ production. 90

5.3 The $+L_{xy}$ tags in the JET50 sample as a function of (a) P_T and (b) the number of good tracks in a jet (N_{SVX}) showing correlations with the tag rate in each of the two variables. The open circles are the $+L_{xy}$ tag rate, and the closed triangles are the $-L_{xy}$ tag rate. 92

5.4 The $\sum E_T$ for the JET50 sample (dashed histogram), the W+jets signal sample (dot shading), and for the $\sum E_T$ sample (cross hatch). The arrows are $\sum E_T$ values for the tagged W+jet events, as described in Section 4.4 95

5.5 Correlations between $+L_{xy}$ tagging rates and (a) the $\sum E_T$ variable and (b) the N_{JET} variable. The points are the observed tags in the JET50 sample and the histogram is the predicted tags using the standard tag matrix. Note the systematic shift high of the predicted tags for large jet multiplicities. The differences are accounted for in the systematic uncertainty of the background measurement. 97

5.6 Results using the 12 tag matrices to predict background tags in the $W+\geq 3$ jet sample (points). See text for description of each of the 12 variables. The central solid line is the predicted background tags from the standard tag matrix, and the surrounding solid lines are the error bars on that prediction, both statistical and systematic uncertainties are included. 100

5.7 The lowest order (a) $Wb\bar{b}$ and $Wc\bar{c}$ production diagram that is calculated by the modified HERWIG Monte Carlo calculation. A second, higher order, diagram is also shown in (b). 102

5.8 The observed excess tags (solid triangles) and the Monte Carlo predicted tags (open circles) in the JET50 sample, shown as a function of jet E_T and N_{JET}. The prediction uses the HERWIG Monte Carlo calculation for the heavy flavor prediction. 103

5.9 The Feynman diagrams for Wc production. Gluon fusion with a strange quark (a) and the other first order, but Cabibbo suppressed diagram (b). 108

5.10 The lowest order WW and WZ production diagrams. 112

5.11 The results of the secondary vertex search in the W+jets data sample, binned by number of jets. The open circles are before secondary vertex tagging, and the solid triangles are after tagging. The cross-hatched boxes are the two after tagging background estimates. 116

6.1 The sum of SVX and SLT tags observed in the W+jets sample (solid triangles). Events tagged by both algorithms are counted twice. The shaded area is the sum background predictions. . . 119

6.2 The CDF calculated $t\bar{t}$ production cross section shown as a function of top mass (points) and the theory curve (line) by Laenen et al[1]. The dashed lines represent the uncertainty in the theory calculation. 126

6.3 The distribution of reconstructed top mass for Monte Carlo events generated with $M_{top} = 170$ GeV/c^2. The full histogram corresponds to the best fit obtained by the fitting program when requiring that one of the b jets is a b in the fit. The dashed histogram is obtained if the correct assignment for each of the jets is made. 129

6.4 Fit top mass distribution for the data (solid histogram) and the background of 1.4 events (dots) obtained from the W+ multijets VECBOS events. The dashed histogram represents the sum of 5.6 $t\bar{t}$ Monte Carlo events (from the M_{top}=175 GeV/c^2 Monte Carlo simulation) plus the 1.4 background events. 130

6.5 The results of the maximum likelihood fit to the top mass. The vertical error bars represent the uncertainties due to the statistics in the Monte Carlo event samples. 134

A.1 A schematic diagram for one barrel of the SVX water cooling system. About 1.5 gallons of water are held and cooled to 9°C in the reservoir. The cold water is pumped through a filter, and to the bypass and SVX valves. Most of the water travels through the bypass valve, the deionizer, and returns to the reservoir. A small amount of water travels through the SVX valve and into the SVX carrying away heat generated by the electronics. Pressures are measured (transducers are marked by the *PT* symbol) in the reservoir and just before the entrance to the SVX. 141

A.2 Functional schematic of the SVX interlock system. The interlock system is controlled by a TI 435 RLL processor, labeled the "Interlock Box" here. It monitors SVX temperatures and pressures, and controls enables for the SVX power supplies, the SVX valve, and the chiller pump. The temperatures are measured by current devices, and the currents are converted to voltages by the "Temperature Box". Status lights and a key switch are the user interface. There is one system for each barrel, though the barrels share the Interlock Box and the Temperature Box. . . 142

List of Tables

1.1 Decay modes for a $t\bar{t}$ pair and their approximate branching ratios (to lowest order), assuming charged-current decays. The symbol q stands for one of the quarks, u, d, c, or s. 13

2.1 Physical properties of the Central Tracking Chamber. 26

2.2 Characteristics of the central and end wall calorimeter. 29

2.3 Summary of the physical properties for the plug calorimeters. 31

3.1 The selection requirements for a good ICE electron. 46

3.2 The selection requirements for a good soft muon. E_{HAD}, the hadronic calorimeter energy and E_{EM}, the electromagnetic calorimeter energy, both refer to only the tower the muon goes through. δx and δz refer to the difference is distance between a matched CTC track and the muon stub. 47

3.3 The numbers of like-sign and unlike-sign e-μ combinations with a mass less than 4 Gev/c^2 in the ICE sample. Uncertainties are statistical only. 48

3.4 The high-P_T electron selection criteria. 50

3.5 The high-P_T muon selection criteria. 50

3.6 The number of events passing the W sample selection criteria. The Good Lepton requirement includes all quality selection, fiducial requirements, E_T requirements, and conversion removal. 53

3.7 The final W sample as a function of jet multiplicity. Each jet is required to have $E_T \geq 15$ GeV and $|\eta| < 2.0$. The signal region consists of all events with 3 or more jets. 54

3.8 The expected background contributions in the $W+ \geq 3$ jet sample due to non-W, Z, and divector boson sources. The uncertainty in the total background takes into account the correlations in uncertainties in the various background sources. . . . 55

3.9 Selection criteria for the second electron in a $Z \rightarrow ee$ event. . . 56

3.10 Selection criteria for the second muon in a $Z \rightarrow \mu\mu$ event. . . . 57

4.1 The composition of the tags in $t\bar{t}$ Monte Carlo generated events. All numbers have an error of 10% associated with them due to statistics. 68

4.2 Tagging results in the ICE sample and ISAJET $b\bar{b}$ Monte Carlo generated events. The predictions are used for background subtraction. 73

4.3 The raw numbers used to calculate $F_{scale}^{taggable}$. 75

4.4 The acceptance and expected event yield of $t\bar{t}$ events for M_{top} of 120, 160, and 180 GeV/c^2 in 19.3 pb^{-1} of data. 78

4.5 The expected number of tagged events and ϵ_{tag} for various top masses. 80

4.6 Details of the six JETVTX tagged events in the $W+ \geq 3$ jet signal sample. A $\surd$ indicates the jet tagged by JETVTX. . . . 82

5.1 Tags in the JET50 sample. The 15 GeV jet requirement matches the 15 GeV jet requirement in the W signal sample by design. 89

5.2 The predicted mistags from the $+L_{xy}$ tag matrix in the W+jet event sample. The uncertainties are due both statistical and systematic uncertainties. 93

5.3 JETVTX tags and predictions in the control samples. 94

5.4 The predicted mistags calculated by the $-L_{xy}$ tag matrix in the W+jet event sample. The largest uncertainty is due to the mismatch in $-L_{xy}$ tag rates in the $\sum E_T$ sample. 101

5.5 The number of $Wb\bar{b}$ events predicted by HERWIG's calculation as well as standard HERWIG in the W+1 and 2 jet data samples. The complete detector simulation and the analysis (excluding the b-tag requirement) are used. Only the $W \rightarrow e\bar{\nu}$ channel is shown. The default HERWIG prediction, both raw and normalized to the number of $W + 1$ jets observed in the data, is also listed for comparison. 104

5.6 Fraction of W+jet events with at least one b-quark jet. The numbers are from the standard HERWIG calculation. A scale factor of 1.4 ± 0.8 is applied to make the $W + 1$ jet bin match the modified HERWIG calculation. 105

5.7 Predicted $Wb\bar{b}$ and $Wc\bar{c}$ tags in W+1, 2, and 3 or more jet events by the modified HERWIG calculation. 106

5.8 Estimated non-W events in the electron and muon W event samples. Estimates are made using the I *vs.* $\not{E}_T$ scaling. . . . 109

5.9 The tagging rates in the region I < 0.1 and $\not{E}_T < 15$ GeV, and the excess tagging rate (over the predicted background from the JET50 sample). 110

5.10 The calculated tags in excess of the predicted tags from the tag matrix in the signal region due to non-W events. 110

5.11 ϵ_W and ϵ_Z, efficiency for $Z \rightarrow \tau\tau$ and $W \rightarrow e\bar{\nu}$ events to pass the W+1 jet event selection requirements. 112

5.12 Expected $Z \rightarrow \tau\tau$ events in the W+1 jet bin before and after tagging has been applied. Only the $W+1$ jet case is examined, as there is expected to be negligible contributions to the higher jet multiplicities. The tagging rate is $0.016 \pm 0.012\%$. 112

5.13 The diboson kinematic selection efficiencies, in percent. 114

5.14 The diboson cross section in pb before tagging for the various decay channels, listed by jet multiplicity. 114

5.15 The event tagging rates for the diboson backgrounds. 114

5.16 The total background tags expected in each jet bin in the W+jet sample. 115

6.1 The results of the soft lepton top quark search. The W sample is the same as used in the secondary-vertex search. 118

6.2 The probability of the expected background fluctuating up to the observed events in each of the three top searches detailed in CDF's recent top PRD[2]. 121

6.3 Summary of the rate of Z candidates both with and without b tags, and the expected backgrounds. 122

6.4 The expected number of tags due to non-$t\bar{t}$ sources when the $W+\geq 3$ jet sample is assumed to have some $t\bar{t}$ content. $N_{t\bar{t}}$ is the estimated number of $t\bar{t}$ events in the $W+\geq 3$ jet sample. . 123

6.5 The corrected tagging efficiency. ϵ_{tag} does not take into account the probability that a non-b quark jet will be tagged in a $t\bar{t}$ event. 124

6.6 SVX cross section for four different top masses. The σ^{ALL} is calculated as described in the text. σ^{SVX} is calculated by the simple relation $n_i = \epsilon_i \cdot \int \mathcal{L}dt \cdot \sigma^{SVX}$. 124

6.7 The fit masses of the SVX and SLT tagged events. The run and event number are listed, along with the type of high-P_T lepton, the algorithm that tagged the jet, the mass fit and its uncertainty, and the χ^2 of the fit. 131

6.8 The sources of systematic errors in the top quark mass determination. 132

Chapter 1

Theory

1.1 Introduction

In the past century physicists have explored the interactions and properties of fundamental particles. The definition of a fundamental particle has changed with time, progressing from the relatively large atom to the much smaller constituents of protons and neutrons, the quarks. The interactions of fundamental particles are governed by the four basic forces of nature: the strong force, the electromagnetic force, the weak force, and the gravitational force. Physicists have combined three of the four forces into a single model, the Standard Model, which describes the fundamental particles and how they interact. The Standard Model has enjoyed great success, as it has predicted both unobserved particles and particle decays. Since the Standard Model has gained acceptance, physicists have tried to measure the many parameters in the theory, such as the quark masses. The goal is to test the Standard Model by comparing the measurements of these parameters with values allowed by the Standard Model. This thesis describes the search for one of the unobserved quarks, called the *top* quark, which must exist in the Standard Model.

Special techniques are required to observe and explore the fundamental particles of the Standard Model. The most common method is to use one particle as a probe to explore another. Rutherford used this technique in 1911 in his discovery of the atomic nucleus. His famous scattering experiment used alpha particles (He nuclei) emitted from a radioactive source to probe the structure of a thin gold foil. After passing through the metal foil, the alpha particles hit a scintillating screen and the light patterns were used to judge what path the alpha particles had taken, and how they had been deflected by the metal foil. The pattern of deflections were consistent with being caused by a small massive charged sphere, surrounded by empty space, instead of the then popular large homogeneous model of the atom. This was the discovery of the atomic nucleus.

The Rutherford experiment is analogous to present day fixed-target experiments. Generally, a fixed-target experiment has a high-energy particle beam (typically electrons, protons, or pions) focused on a stationary target. The fixed-target detector is built around the target to capture the resulting debris. The data used for this thesis were taken at the Collider Detector at Fermilab (CDF). Unlike a fixed target experiment, CDF is at the collision point of two opposing beams of high energy particles, one composed of protons and the other of antiprotons. The CDF detector collects debris from collisions of the two beams.

There are two main types of colliders operating today. The first type is the electron-positron collider, such as LEP at CERN in Switzerland, Tristan at Tsukuba in Japan, or the SLC at Stanford in California. Secondly, there are hadron colliders in operation, the largest one (for some time to come now since the demise of the SSC) is the Tevatron at Fermi National Accelerator Laboratory (FNAL) in Batavia, Illinois, where CDF is located. It collides

protons (p) with antiprotons ($\bar{p}$) at a center of mass energy of $\sqrt{s} = 1.8$ TeV. The high center-of-mass collision energy enables the probing of high energy and small distance scales, even the quark structure of the proton.

1.2 The Standard Model

The particle physics field has been dominated by the Standard Model for the past 16 years. It represents the unification of three of the four basic forces: the strong force, described by Quantum Chromodynamics (QCD), and the weak and electromagnetic forces, jointly described by the electroweak model. Gravity, the fourth force, is too weak to play a role in fundamental particle interactions described in this thesis. Since 1978, when the Standard Model was first proposed as a cohesive theory[3], it has met with wide acceptance in the physics community. There have been no major inconsistencies between its predictions and the experimental data.

Figure 1.1 is the Standard Model at a glance. Fundamental particles in the Standard Model can be divided into two classes, the fermions and the bosons. The fermions are the quarks and leptons, with intrinsic spin $\frac{1}{2}$. The quarks come in six flavors: up (u), down (d), charm (c), strange (s), top (t), and bottom (b). There is experimental evidence for all but the t-quark, which is the subject of this thesis. The quarks are grouped in weak isospin doublets, as shown in Figure 1.1. Each quark also carries an additional quantum number, color, the charge of the strong force. The color can be red (R), green (G), or blue (B).

The leptons are the second set of fermion particles and are also grouped into three weak isospin doublets. The leptons are the electron (e), the muon (μ), the tau (τ), and their corresponding neutrinos (ν_e, ν_μ, ν_τ). The e, μ, and

Fermions			Bosons
Quarks	Q/e	Weak Isospin	$\begin{pmatrix} W^+ \\ Z^0 \\ W^- \end{pmatrix}$
$\begin{pmatrix} u \\ d \end{pmatrix} \begin{pmatrix} c \\ s \end{pmatrix} \begin{pmatrix} t \\ b \end{pmatrix}$	$\begin{pmatrix} +\frac{2}{3} \\ -\frac{1}{3} \end{pmatrix}$	$\begin{pmatrix} +\frac{1}{2} \\ -\frac{1}{2} \end{pmatrix}$	8 Gluons (g) Higgs (h)
Leptons			
$\begin{pmatrix} e \\ \nu_e \end{pmatrix} \begin{pmatrix} \mu \\ \nu_\mu \end{pmatrix} \begin{pmatrix} \tau \\ \nu_\tau \end{pmatrix}$	$\begin{pmatrix} -1 \\ 0 \end{pmatrix}$	$\begin{pmatrix} -\frac{1}{2} \\ +\frac{1}{2} \end{pmatrix}$	Photon (γ)

Figure 1.1: The fundamental particles that make up the Standard Model. Quarks and gluons carry color (Red, Green, and Blue), while the leptons, $W^{\pm}$, Z^0, and γ are colorless. The quarks and leptons also have antiparticle counterparts. Interactions between the fermions (quarks and gluons) are mediated by the second group, the bosons ($W^{\pm}$, Z^0, gluons, and γ).

τ all carry a negative electric charge, while the neutrinos carry no charge.

The bosons have an intrinsic integer spin, instead of spin $\frac{1}{2}$. The bosons are the mediators of force in the Standard Model. They include the photon (γ), the W^+, the W^-, the Z^0, and the eight gluons (g). When electrodynamics was combined with the weak force, Glashow, Weinberg and Salam used a theory with four massless mediators: the W^+, the W^-, the Z^0, and the γ. Spontaneous symmetry breaking and the Higgs mechanism give mass to the first three bosons and add another boson to the theory, the Higgs boson (h). There has been no experimental evidence for the Higgs to date. The SSC had been designed, in part, to look for the Higgs. Finally, the gluons are the mediators of the strong force.

Hadrons are quark-antiquark or three quark bound states held together by the strong force. No free object is allowed to have net color; the hadrons are all color singlets. The quark-antiquark states are called mesons, and the three

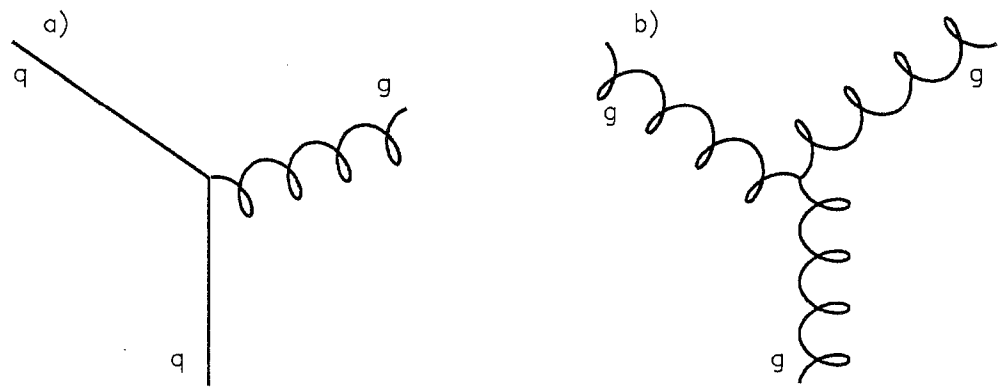

Figure 1.2: A (a) quark-gluon strong vertex and a (b) gluon-gluon strong vertex. The gluons can interact with themselves, unlike photons, because gluons carry a color charge. The flavor of a quark at a gg vertex will not change, though its color may.

quark states are called baryons. The hadrons are the most commonly observed particles in the CDF detector. Two examples of hadrons are the pion (the pion quark content is $u\bar{d}$, $u\bar{u}$, and $d\bar{u}$) and the kaon (the kaon quark content is $s\bar{d}$ and $s\bar{u}$). In QCD, color plays the roll that electric charge plays in electrodynamics. At a strong vertex (see Figure 1.2a) the quark flavor cannot change, though the color of the quark can. Color is conserved in strong interactions, thus the gluon must carry a color and an anticolor ($r\bar{g}$ for example). All eight gluons carry two colors; there is no color singlet gluon. Since gluons have color, they can interact with each other at a strong vertex (see Figure 1.2b). It is important to note that the strong force does not interact with the leptons or the vector bosons (the W, the Z, or the γ), as they do not carry color.

Since the quarks are colored, they are never observed on their own. Unlike the electromagnetic force which is proportional to $1/r^2$, where r is the distance between two interacting particles, the strong force is proportional to r. The reason is charge screening. In the quantum theory of electromagnetism, charge screening occurs because e^+e^- pairs are spontaneously created from

the vacuum. In QCD, $q\bar{q}$ pairs and gg pairs are created from the vacuum. The screening due to $q\bar{q}$ and gg creation have opposite effects on the strength of the strong force, which is represented in the theory by the α_s parameter. At short interaction distances, $q\bar{q}$ pair creation increases the value of α_s, while gg pair creation reduces it. The opposite effect occurs at large interaction distances and gg pair creation increases the value of α_s. In QCD, it is the gg pair creation that dominates. The strong force increases at large distances of separation; its typical interaction range is $\sim 10^{-15}$m. Intuitively, this is the reason a quark is never seen on its own. Proof of this effect, called *quark confinement*, is difficult because the required approximations break down at large r.

Most hadrons, unlike the proton, are not stable. The lifetime for the proton is $\geq 10^{31}$ years. Most hadrons, however, are unstable, with lifetimes of 10^{-5} to 10^{-20} seconds.

Jets are ubiquitous in hadron colliders, and $q\bar{q}$ pair creation is responsible for their formation. A loose definition of a jet is a collimated collection of particles spawned from a single quark or gluon from the primary interaction. The quark or gluon is called a parton because it is "part" of the proton. Conceptually, a quark gets knocked out of a proton by another quark. As it travels farther and farther from its partners (which remain in the "proton") the strong force between them increases. Eventually the force between the quark and its partners is so strong it becomes energetically favorable to create a $q\bar{q}$ pair from the vacuum. One of the quarks is attracted back towards the proton and the other towards the escaping quark:

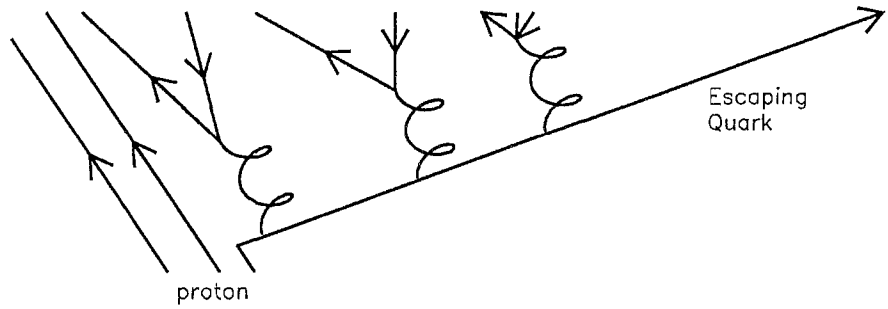

This process continues as the proton and quark move apart. The result is the formation of a large number of particles, often dozens. The production of hadrons by this process is called hadronization. Jets observed in the CDF detector are created by this process. Figure 4.11b, an event picture in the CDF detector, shows what typical jets look like in CDF's charged tracking detectors.

1.3 Proton-Antiproton Collisions

Protons and antiprotons are not fundamental particles. Like other baryons, they consist mainly of 3 quarks, called the valence quarks. The proton's valence quarks are uud, and the antiproton's are $\bar{u}\bar{u}\bar{d}$. Other quarks are continually being created and destroyed in the proton. These quarks are called the *sea* quarks. The sea quarks appear as virtual pairs such as $u\bar{u}$ or $d\bar{d}$ being quickly created and annihilate in the vacuum. Lastly, the proton also consists of gluons that bind the proton together. At the high collision energies of the Tevatron, $\sqrt{s} = 1.8$ TeV, the proton and antiproton rarely interact as a unit, but rather a constituent, such as a valence quarks of the proton and antiproton, interact.

Most of the proton-antiproton ($p\bar{p}$) collisions involve low energy $q\bar{q}$ or gg scattering; only occasionally does an interesting interaction involving large momentum transfer occur. W boson and t-quark production occur by a process

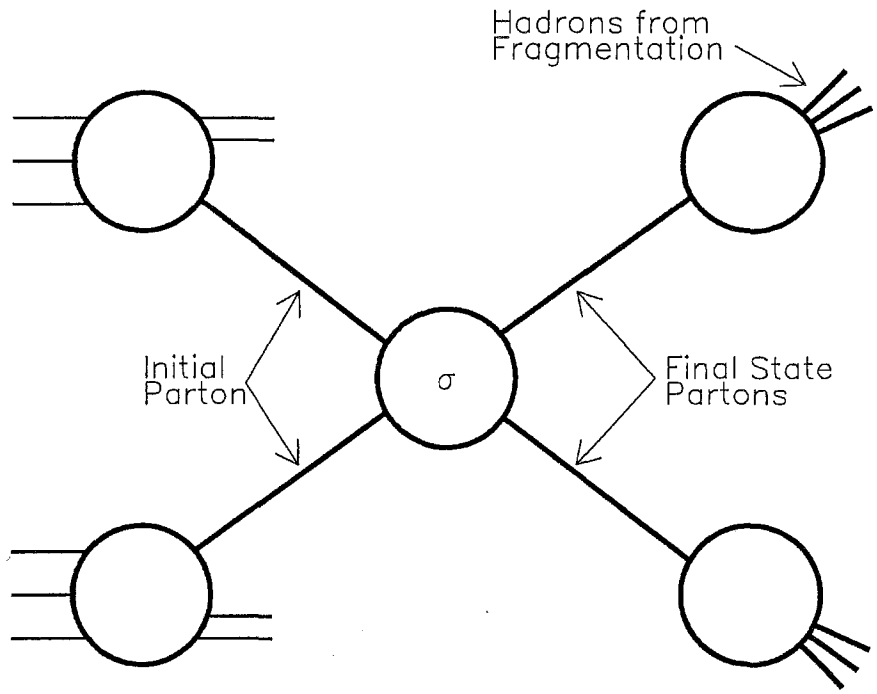

Figure 1.3: At the Tevatron the most interesting $p\bar{p}$ interactions involve an energetic interaction between a constituent of the proton and one of the antiproton. The remaining partons in the p and $\bar{p}$ are called spectators. The products of the interaction fragment into hadrons, or in the case of the W boson decay, into leptons.

similar to the diagram in Figure 1.3. In W boson production, the initial partons (quarks, gluons) form a real W boson which subsequently decays to the final state partons. The quarks, along with the gluons, hadronize and decay to other leptons and hadrons in the final state. The final state hadrons form jets whose momenta is nearly collinear with that of the final state partons.

In addition to the basic process, gluons are often emitted.from the intial or final state partons. The gluons then hadronize to form additional jets in the event. This process is called initial or final state radiation, depending on the parton from which the gluon radiates.

Before going further it is best to define a few terms. In $p\bar{p}$ collisions, the component of the momentum parallel to the beam pipe of the initial partons is not known because the initial z momenta of the valence quarks and the

composition of the proton sea are unknown. Therefore, the momenta parallel to the beam pipe is not a useful quantity in $p\bar{p}$ collisions, rather, the transverse momenta is used since it is assumed to be zero in the intial state. Some useful quantities and their definitions are:

- P_T, the transverse momentum of a particle, is the momentum perpendicular to the beam direction.
- E_T, the transverse energy, is the energy perpendicular to the beam direction of a particle. $E_T = E \sin\theta$ where E is the total energy of a particle, and θ is the angle the particle makes with the beam axis, $\theta = 0$ is parallel and in the same direction as the proton beam (θ is the polar angle).
- $\not{E}_T$, missing E_T, is the energy that is missed by the detector. Neutrinos do not interact, and thus cannot be easily detected, and do not leave energy deposition in the calorimeters. Their energy contributes to $\not{E}_T$. $\not{E}_T$ is the negative of the vector sum of all energy in the calorimeter, such that $\not{E}_T$ plus the total calorimeter energy sum to zero.
- η, pseudorapidity, is defined as

$$\eta = -\ln\tan(\theta/2)$$

1.4 Top Quark Production and Decay

The top quark is the only one of the six quarks in the Standard Model for which direct decay products have not been observed. The masses of the first

five quarks are all less than 6 GeV/c^2, while the lower limit on the top quark mass is much heavier, 131 GeV/c^2[4].

There is strong circumstantial evidence that the top quark exists. The JADE collaboration observed a forward backward asymmetry in $e^+e^- \rightarrow b\bar{b}$ decays[5]. This is predicted by the Standard Model. The asymmetry implies a b-quark isospin of $-\frac{1}{2}$. Since the other quarks are already paired in isospin doublets, the b-quark's isospin partner is presumed to be the undiscovered top. LEP has confirmed the measurement of the b-quark's isospin[6].

The non-observation of Flavor Changing Neutral Currents (FCNC) in B hadron decay gives further evidence that the top quark exists. Cabibbo suggested skewing the quark generations, mixing a small amount of s in with d for the purposes of weak interactions. In 1970 Glashow, Illiopoulos, and Maiani (GIM) extended it to neutral current decays, which involve a Z boson instead of the W boson. In 1973 Kobayashi and Maskawa (KM) extended the theory to three quark generations. The extended GIM mechanism describes why there are no FCNC decays of the b-quark. B decays via FCNC have not been observed[7]. The extension to the GIM mechanism relies on the existence of the t-quark. Kobayashi and Maskawa used a matrix notation to describe the mixing of the quark states,

$$\begin{pmatrix} d' \\ s' \\ b' \end{pmatrix} = \begin{pmatrix} V_{ud} & V_{us} & V_{ub} \\ V_{cd} & V_{cs} & V_{cb} \\ V_{td} & V_{ts} & V_{tb} \end{pmatrix} \begin{pmatrix} d \\ s \\ b \end{pmatrix}.$$

The diagonal elements are close to 1, and the off diagonal elements are close to 0 ($0.9747 < V_{ud} < 0.9759$, $0.997 < V_{tb} < 0.999$, and $0.004 < V_{td} < 0.015$ for example)[8]. The matrix with elements $V_{qq'}$ is referred to as the CKM matrix.

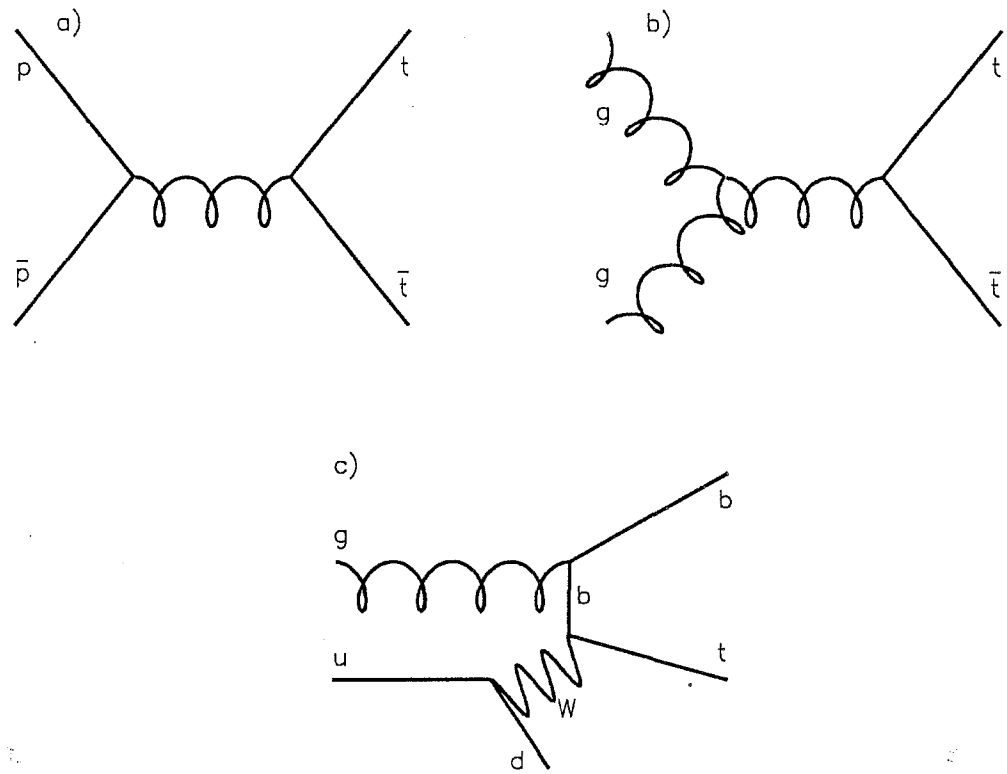

Figure 1.4: Feynman Diagrams for top production by (a) quark-antiquark annihilation, (b) gluon-gluon fusion, and (c) single top production via W-gluon fusion. W-gluon fusion is not considered here as it is expected to occur at a relatively small rate[9], about one fifth the $t\bar{t}$ production rate.

A major effort in the high energy physics community has been to measure all the elements of the CKM matrix.

In $p\bar{p}$ collisions, top quarks are expected to be produced by both gluon-gluon fusion and $q\bar{q}$ annihilation. Figure 1.4 shows the Feynman diagrams for the two processes. For top masses above 100 GeV/c^2 and center of mass energies near the $\sqrt{s} = 1.8$ TeV, $q\bar{q}$ production is expected to be the dominate $t\bar{t}$ production process.

In the Standard Model a top quark decays almost exclusively to a W boson and a b-quark. There are other decays possible, but they are suppressed, as the off diagonal elements of the CKM matrix are close to zero. There are

additional theories that add to the Standard Model and provide for other t-quark decay channels, but only the minimal Standard Model t-quark decay is considered in this thesis. This search for the top quark looks in the decay channel $t \rightarrow Wb$ only.

The W boson decays weakly to leptons or to quarks. The quarks will subsequently hadronize to jets. Table 1.1 lists the final states of $t\bar{t}$ production, tabulated by the W boson's decay. Though the all-jet channel $t\bar{t} \rightarrow (q\bar{q}'b)(q\bar{q}'\bar{b})$ has the largest branching fraction (44%), it is plagued by a large background from QCD multi-jets events, making a top search in this channel very difficult. The dilepton channel (both W bosons decay to a lepton-neutrino pair) has very small backgrounds, but also a very small rate (5%). A full treatment of the dilepton analysis can be found in Reference [2]. This analysis concentrates on the lepton+jets decay mode of the $t\bar{t}$ pair in which one of the W bosons decays to a lepton-neutrino pair and the other W decays to quark jets:

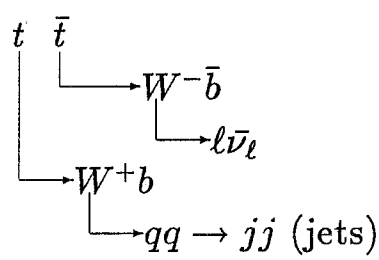

The top quark is searched for in a large data sample of events containing W bosons. The dominate background is QCD W production.

1.5 Bottom Quark Decay

Unfortunately, the top signal is not large enough to be seen as a significant excess in the W+jet production rate. (This argument will be made in greater detail in Section 3.4 and in Chapter 4). It is therefore necessary to further

Decay Mode	Branching Ratio
$t\bar{t} \longrightarrow (q\bar{q}'b)(q\bar{q}'\bar{b})$	36/81
$t\bar{t} \longrightarrow (q\bar{q}'b)(e\nu\bar{b})$	12/81
$t\bar{t} \longrightarrow (q\bar{q}'b)(\mu\nu\bar{b})$	12/81
$t\bar{t} \longrightarrow (q\bar{q}'b)(\tau\nu\bar{b})$	12/81
$t\bar{t} \longrightarrow (e\nu b)(\mu\nu\bar{b})$	2/81
$t\bar{t} \longrightarrow (e\nu b)(\tau\nu\bar{b})$	2/81
$t\bar{t} \longrightarrow (\mu\nu b)(\tau\nu\bar{b})$	2/81
$t\bar{t} \longrightarrow (e\nu b)(e\nu\bar{b})$	1/81
$t\bar{t} \longrightarrow (\mu\nu b)(\mu\nu\bar{b})$	1/81
$t\bar{t} \longrightarrow (\tau\nu b)(\tau\nu\bar{b})$	1/81

Table 1.1: Decay modes for a $t\bar{t}$ pair and their approximate branching ratios (to lowest order), assuming charged-current decays. The symbol q stands for one of the quarks, u, d, c, or s.

differentiate $t\bar{t}$ events from QCD W+jet production. The b-quark in the $t \rightarrow Wb$ allows the two types of events to be differentiated.

The top quark, if its mass is greater than 130 GeV/c^2, decays so quickly that it does not have time hadronize (it decays in $\sim 10^{-23}$ s)[10]. The b quark, however, does have a long lifetime, and does hadronize to a B hadron. The average B hadron lifetime is $c\tau = 453$ μm[11]. The B hadron that forms from the b-quark plays a key role in this analysis. Figure 1.5 shows the P_T distribution for b-quarks from a top decay in a Monte Carlo simulation with M_{top}= 160 GeV/c^2. The Lorentz boost and long B hadron lifetime means bottom hadrons from top decays can travel as far as 1 mm or 2 mm from the t-quark decay position (or vertex) before they also decay. There are an average of 5.75 charged particle tracks from a B hadron decay[12]. It is possible for a detector to resolve the secondary decay from the primary interaction event vertex (called the *primary vertex*) if the detector efficiently reconstructs the charged particle tracks and has a high spatial resolution.

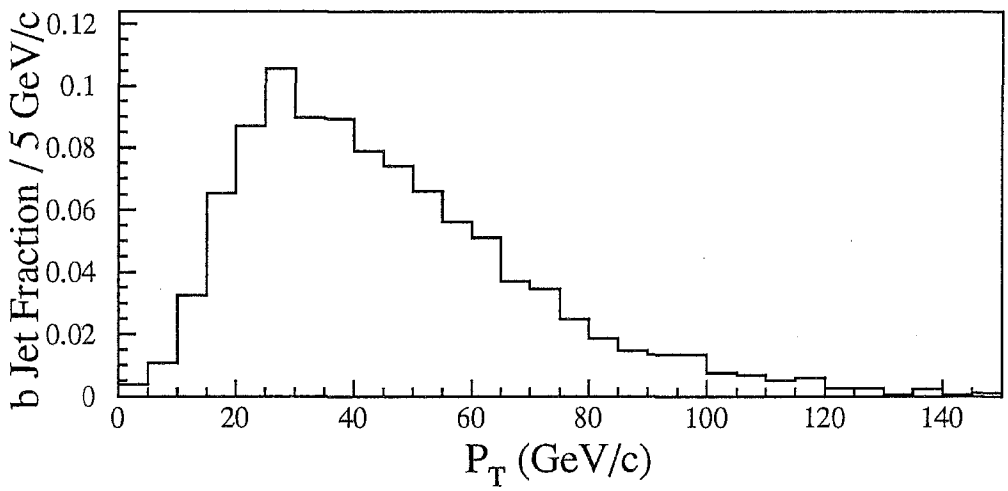

Figure 1.5: The P_T distribution for b-quarks from t-quark decays with M_{top}= 160 GeV/c^2.

Unfortunately, there are other sources of b-quark jets in the W+jet sample besides top. Worse, because the algorithm used looks for only displaced decay vertices, it is sensitive to any long lived particle, like a charmed hadron. Backgrounds due to other sources of long lived particles (heavy flavor) must be carefully estimated. The primary source of heavy flavor in the W sample are $Wb\bar{b}$ and $Wc\bar{c}$ events, a W with a gluon jet that has split into a heavy flavor pair. Figure 1.6, with the symbol "q" representing b-quarks or c-quarks, is a good example of this process.

Since both B and charmed hadrons have a long lifetime and may decay some distance from the primary vertex, both $Wb\bar{b}$ and $Wc\bar{c}$ events will be identified as top candidates. The $Wb\bar{b}$ and $Wc\bar{c}$ backgrounds cannot be separated from the $t\bar{t}$ signal, and must be carefully estimated from the data. As a check, a Monte Carlo calculation has been performed of the heavy flavor content of the W+jet sample to the leading order, and concludes the pre-tagging heavy flavor rate is far below the 10% level [13] .

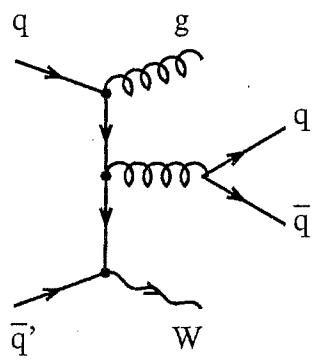

Figure 1.6: The Feynman diagram for QCD W-jet production, one of the backgrounds for the top search.

1.6 Overview of the Analysis

Searching for the top quark by looking for displaced vertices is a complex physics analysis. First, a sample of events containing W bosons with three or more jets are selected from CDF's large event sample. The selection requires a high quality, high-P_T lepton ($P_T >$ 20 GeV/c) and high-P_T neutrino ($\not{E}_T >$ 20 GeV) from a $W \rightarrow \ell\bar{\nu}$ decay. Three or more jets with jet $E_T > 15$ GeV are also required. This sample is called the $W+ \geq 3$ jet sample. Chapter 3 describes the sample selection of the $W+ \geq 3$ jet sample and other samples used in this analysis.

The secondary-vertex finder, described in Chapter 4, attempts to find a displaced vertex in a jet by constraining several charged particle tracks associated with the jet to a common vertex. The distance between the found secondary and primary vertices is defined as L_{xy}. The jet is called a *tagged jet* if the constraint is successful and the 2d uncertainty in the fitted vertex position is small compared to the displacement from the primary vertex.

The efficiency of the tagging algorithm is determined by counting tags in a control sample which is enriched in b-quarks. The fraction of jets in the

control sample which come from b-quark decays is known independently of the b-tagging algorithm, and so can be used to determine the b-tagging efficiency.

The $W+\geq 3$ jet sample has sources of long lived particles that are not due to top quark decays. The tagging algorithm will tag these, as well as tag a small number of jets which are not heavy flavor, i.e. mistakes or mistags. Chapter 5 describes the background calculation, where the contributions to the tags due to non-top sources are estimated. The primary sources of backgrounds in the $W+\geq 3$ jet sample are B and charm hadrons from W events, and mistags. A sample of inclusive jets is used to model the rate at which a jet will be mistagged as a b-jet in the absence of a $t\bar{t}$ signal. Each jet in the $W+\geq 3$ jet data sample is then scaled by this rate to predict the number of tags expected in the absence of a $t\bar{t}$ signal. This method means the calculation of the largest background does not depend directly on a Monte Carlo simulation. This prediction is checked, however, with Monte Carlo calculations. Other backgrounds due to non-W events in the signal sample are calculated using a combination of Monte Carlo simulation and the data. They represent about 15% of the total background.

The concluding chapter, Chapter 6, calculates the probability that the observed result is due to non-$t\bar{t}$ backgrounds and summarizes the $t\bar{t}$ cross section calculation and top quark mass determination of tagged events. The results of the secondary-vertex top quark search should be discussed in the context of the two other top searches performed by CDF. This chapter briefly introduces the dilepton search and the soft-lepton search and discusses their results and the combined significance.

Chapter 2

The Collider Detector At Fermilab

The Collider Detector at Fermilab (CDF) is located in one of two high luminosity interaction regions of Fermilab's Tevatron $p\bar{p}$ collider (Figure 2.1). Six bunches of protons and six bunches of antiprotons rotate in opposite directions around the Tevatron, colliding in the two interaction points, B0 and D0. The CDF detector sits at B0, and the DØ detector occupies the D0 interaction region.

2.1 The Tevatron

The process of loading the Tevatron with protons and antiprotons is called *shot setup*. Each shot results in a *store* of protons and antiprotons that will collide in the Tevatron for $\sim$ 15 hours, unless a problems occur. Collecting enough antiprotons for a store can take in excess of a full day. The protons start out as ionized hydrogen atoms, H^-. The H^- ions are accelerated to 750 KeV in a Cockcroft-Walton, and injected into the LINAC, a linear accelerator. The

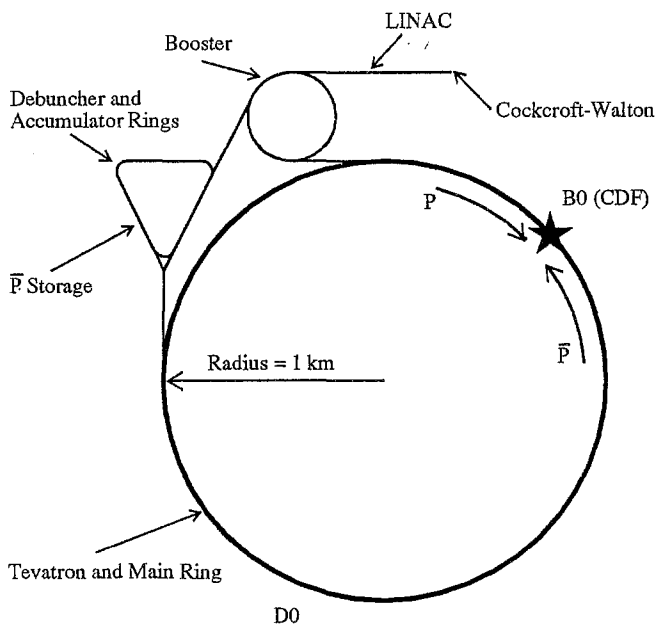

Figure 2.1: The Tevatron. H^- ions are accelerated by the Cockcroft-Walton and the LINAC to 200 MeV. Bare protons, stripped from the H^- ions, are accelerated by the Booster and injected into the main ring. To make antiprotons, the protons are accelerated to 120 GeV and focused on a copper target. The resulting antiprotons are collected in the accumulator. When enough antiprotons have been collected, both protons and antiprotons are accelerated (separately) in the main ring to 150 GeV and injected into the Tevatron, rotating in opposite directions. There the two beams collide at the B0 and D0 interaction regions.

LINAC accelerates the H^- ions to 200 MeV. The 200 MeV stream of H^- ions is focused on a thin carbon foil. As the ions pass through the foil, the two electrons of the H^- are stripped off, leaving a bare proton.

The bare protons are injected into the Booster, a small accelerator (radius of 75.45 m), where they are accelerated to 8 GeV. The protons in the booster are grouped in 7 bunches of approximately 2×10^{10} protons each. From the booster the protons are moved into the Main Ring (radius = 1 km), and accelerated.

To make antiprotons, the protons are accelerated to 120 GeV in the Main Ring. The protons are extracted from the Main Ring and focused on a copper target. 8 GeV antiprotons are selected from the decays caused by the Cu-proton interaction, and are collected and "stacked" in the Accumulator. This process continues the at rate of 4×10^{10} antiprotons per hour until approximately 100×10^{10} antiprotons have been stacked. Stacking enough antiprotons for a shot can take a day, however under ideal conditions, stacking occurs while the previous store is colliding in the Tevatron. Simultaneous collisions and stacking are feasible because the Tevatron is not required for antiproton production. Once the stack is large enough, one-by-one, six bunches of antiprotons (10^{10} per bunch) are extracted from the accumulator and reverse-injected into the Main Ring. They are accelerated to 150 GeV and injected into the Tevatron (rotating counter clockwise). Transfer efficiency between the accumulator and the Tevetron is low for antiprotons; by the time a bunch reaches the Tevatron it contains only 30×10^9 protons.

A single proton bunch for the Tevatron starts out as the same 7 bunches in the Main Ring used for antiproton production, except they are accelerated to 150 GeV, coalesced into a single bunch, and injected into the Tevatron (rotating clockwise).

Once six bunches of antiprotons and protons have been injected into the Tevatron, they are accelerated to 900 GeV. Once accelerated and any beam halo has been removed (through a process called scraping), quadrapole focusing magnets near the interaction regions (B0 and DØ) focus the two beams near the center of the detectors at B0 and D0. The two beams travel around the Tevatron in a double helix and only intersect at the two interaction points. The resulting collisions are recorded by the CDF and DØ detectors. Ideally, the collisions take place at the center of the detectors, however the actual collision point is a gaussian distribution with $\sigma_x = \sigma_y = 35$ μm, and $\sigma_z = 30$ cm, where z is along the beam pipe (see Figure 2.2).

There are two accelerator quantities that we make use of in the top search: the center of mass energy ($\sqrt{s}$) and the integrated luminosity ($\mathcal{L}$). The center of mass energy, equal to twice the beam energy, is fixed at $\sqrt{s} = 1.8$ TeV. The integrated luminosity is defined as

$$N = \mathcal{L}\sigma, \tag{2.1}$$

where N is number of times a given process occurs and σ is the production cross section for that process. $\mathcal{L}$ is expressed in units of barns (1 barn = 10^{-24} cm^2).

Total integrated luminosity is measured at CDF by counting the most basic $p\bar{p}$ interaction, the very weak (feeble) interaction of two partons. This is called a *minimum bias* event. It is the most frequent type of $p\bar{p}$ interaction at the Tevatron, accounting for almost all interactions. The minimum bias interaction generates a spray of particles that leave the interaction point at small angles relative to the beam axis. At CDF these interactions are counted by the small angle scintillators, the Beam Beam Counters (BBC). The BBC

detectors (see Figure 2.2) cover the angular region of 0.32° to 4.47° in both the forward and backward directions ($3.24 < |\eta| < 5.88$). The BBC detectors look for at least one track on opposite sides of the detector at small angles to the beam pipe. Coincident hits in the forward and backward BBCs are used to calculate the instantaneous luminosity, and this is integrated over time to find the total luminosity delivered[14]. The data for this top quark search was gathered between August 1992 and May 1993 (Run IA) at the Tevatron. The integrated luminosity written to tape by CDF during Run IA is $\mathcal{L}$= 19.3 pb^{-1}.

2.2 The CDF Detector

The CDF detector is a large multi-purpose detector, and the data collected from it are used in many different analyses. For the top quark search in the lepton+jets mode, good lepton identification and good b-quark jet tagging are required. A W boson that has decayed leptonically is identified by a lepton with P_T of about half the W mass (M_W = 80 GeV/c^2) and a similar amount of $\not{E}_T$ in the event. Tagging a B hadron decay requires precision track measurement. Figure 2.2 is an overview of the complete CDF detector. The coordinate system is defined by z in the beam pipe direction ($+z$ in the proton direction) and x horizontal, pointing towards the center of the ring, and positive y pointing upwards. The following sections describe the detector in more detail. A large amount of material describing the CDF detector has already been published and can be found in Reference [15].

2.2.1 The Tracking Detectors

The tracking subsystem of the CDF detector consists of three tracking chambers: the Silicon Vertex Detector (SVX) which is closest to the beam pipe, the

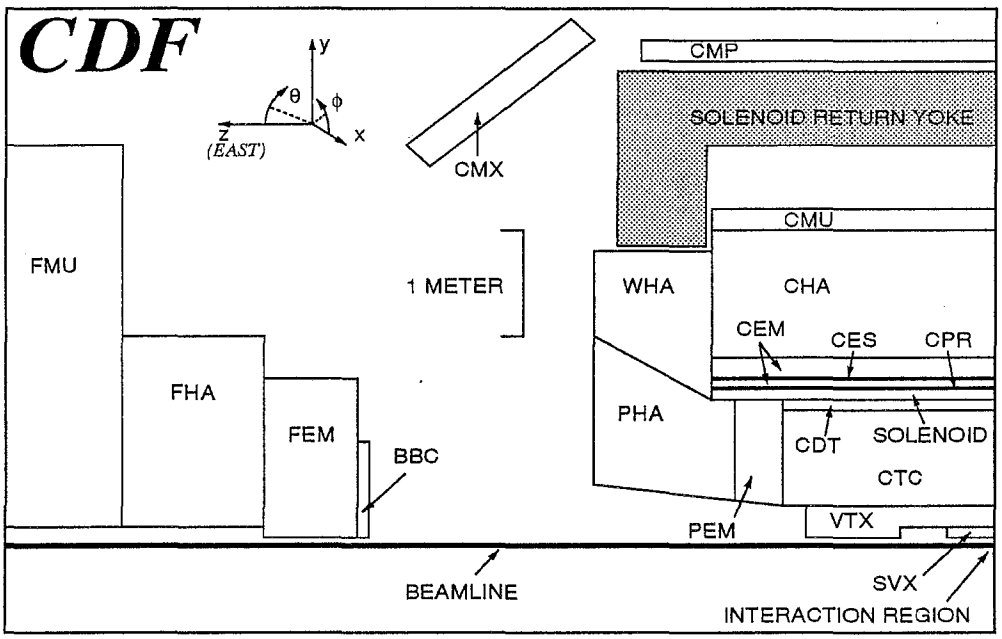

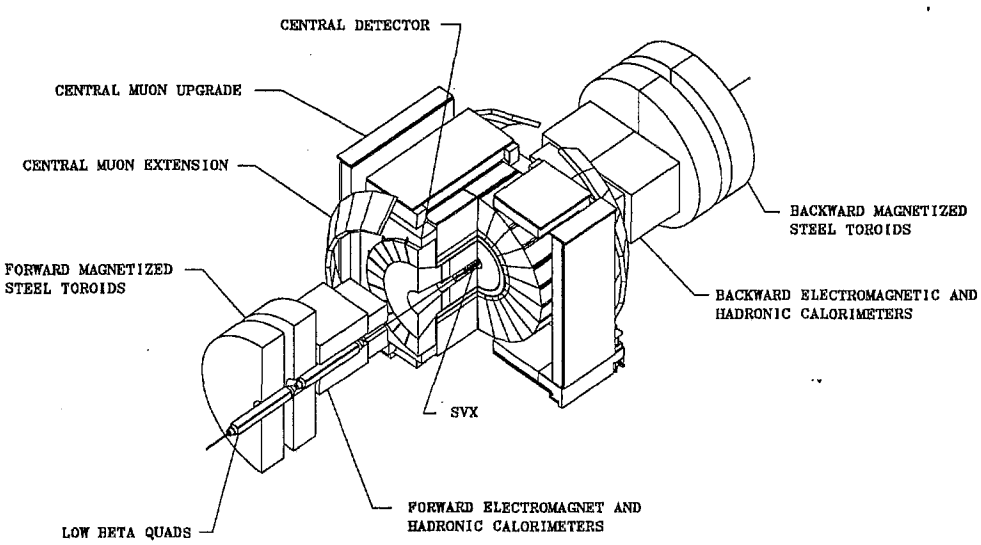

Figure 2.2: A schematic layout of the CDF detector, both a side view and perspective view.

Vertex Time Projection Chamber (VTX) which surrounds the SVX, and the Central Tracking Chamber (CTC) which surrounds the VTX (see Figure 2.2). Because the SVX plays a very important role in b-quark tagging, it will be described separately, in Section 2.2.4.

All tracking takes place within the volume of the CDF solenoidal magnet. The magnet is superconducting, with a 1.5 m radius, and it is 5 m long. During Run IA, the magnet current was 4650 Amps producing an axial magnetic field of 1.4 Tesla. The nonuniformity of the field was measured with a Hall probe in 1986 at a slightly higher current of 5000 Amps. The scaled results of this survey are used during track reconstruction. The corrections were studied and verified using the $J/\Psi \rightarrow \mu\mu$ mass peak.

The VTX resides between the CTC and the SVX. It has an η coverage of $|\eta| < 3.5$. The VTX detector's track resolution in z is 1 mm. It is constructed in eight octagonal modules with sense wires running perpendicular to the beam. Each module is divided in two by a high voltage grid. The drift regions in the VTX are 15 cm long.

The primary use of the VTX in the top search is the determination of the z coordinate of the vertex. There is frequently more than one interaction per event because the Tevatron runs at high luminosity. In W boson events (the signal sample for this analysis; details of its selection will be explained later) it is calculated that 40% of the events containing a W boson also contain one additional interaction. The cross section for minimum-bias events makes it by far the most common type of interaction. Since both interactions produce tracks, care must be taken to associate the correct track with the correct vertex. The VTX efficiency separates the z coordinate of the multiple interactions.

The CTC is a wire drift chamber designed for the precise measurement of a track's momentum and good two-track separation. The CTC covers $|\eta| < 1.0$

and is divided into 9 superlayers: 5 axial layers and 4 stereo layers. The stereo layers have sense wires strung $\pm 3°$ off the z axis for a small angle stereo z measurement. Figure 2.3 is the side view of the CTC, and Table 2.1 lists the physical properties of the CTC.

The track parameters used in this analysis combine information from two of the three tracking chambers. Tracks are found in the CTC, and are used to point back into the SVX detector. The associated track stubs found in the SVX and CTC are combined into one set of track parameters by weighting each detector's contribution according to its uncertainties. The VTX detector is used to seed the CTC tracking algorithm. CDF describes a track with five parameters, some of them have already been mentioned.

- d, the impact parameter (the distance of closest approach in the x-y plane) is measured relative to the primary vertex.
- ϕ, the angle the track makes with the x axis in the x-y plane.
- η, the pseudo-rapidity (defined in Section 1.3) which measures the angle the track makes with respect to the z axis.
- C, the curvature, which describes the bending of the charged track in CDF's magnetic field. It is related to transverse momentum by

$$P_T = 0.000149898 \times 1.4 \text{ Tesla}/C$$

- z_0, the track's z coordinate at the point of closest approach to the primary vertex.

To the first order, the CTC is used to measure the curvature and z position of a track, and the SVX is used to measure the impact parameter (see

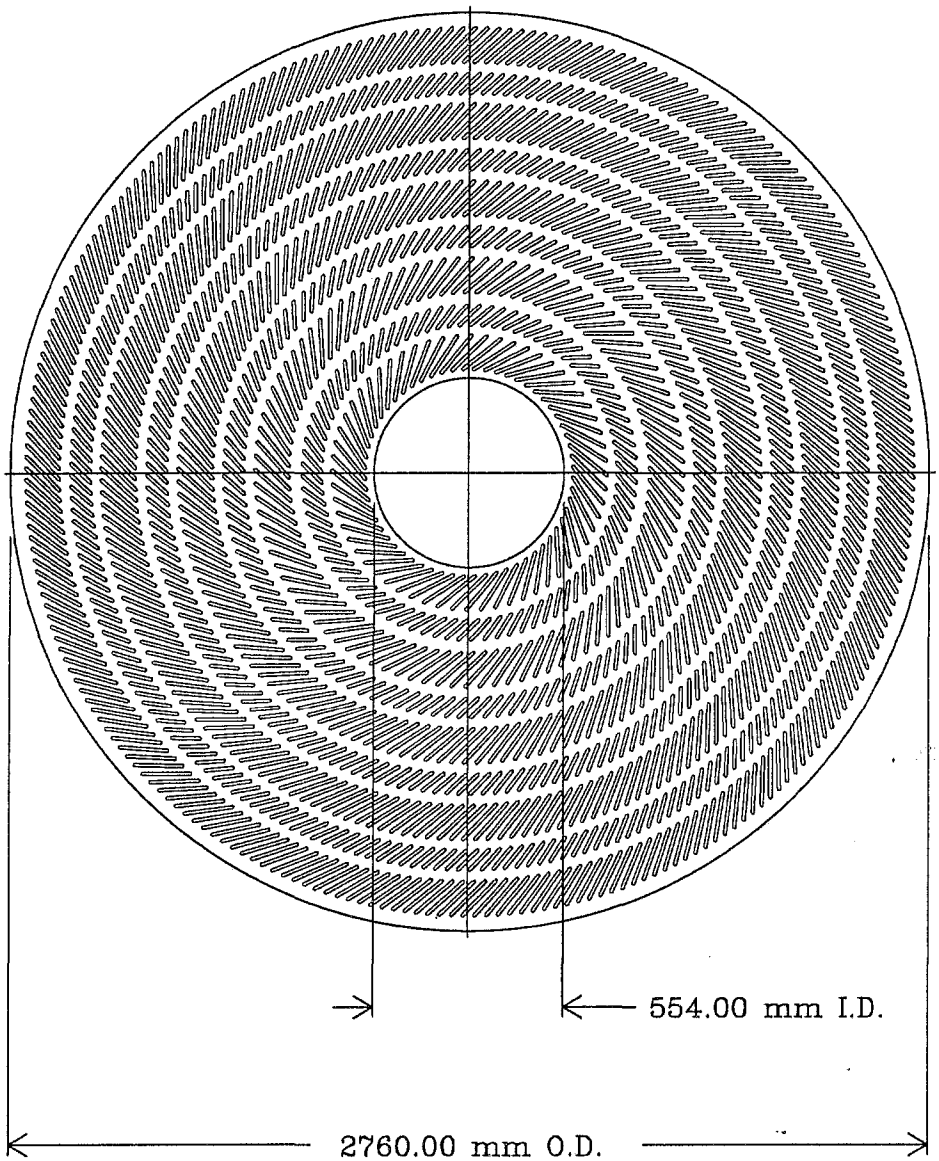

Figure 2.3: The CTC endplate. Each ring is a superlayer. The thicker rings are axial superlayers, the thiner rings are stereo super layers. The slots are the points where wires that exit the chamber are attach to electronics normally mounted on the endplate. The stereo superlayers have 6 wires, and the axial superlayers have 12.

Coverage:	
Inner Layer	$15° < \theta < 165°$
	$-2.0 < \eta < 2.0$
Outer Layer	$40° < \theta < 140°$
	$-1.0 < \eta < 1.0$
Mechanical:	
Superlayers	9
Axial Layers	5
Wires / Axial Layer	12
Stereo Layers	4
Wires / Stereo Layer	6
Inner Radius (Active)	30.9 cm
Outer Radius (Active)	132.0 cm
Wire Length	321.4 cm
Total Wires	36,504
Drift Length	15.25 cm
E Drift Field	1350 V/cm
Gas	Ar (49.6%)
	Ethane (49.6%)
	Alcohol (0.8%)
Resolution:	
Spatial	200 μm (r-ϕ)
	6 mm (z)
2-track	3.5 mm
Momentum	$\delta P_T/P_T = 0.0020 \times P_T$
Momentum (Beam Constrained)	$\delta P_T/P_T = 0.0011 \times P_T$

Table 2.1: Physical properties of the Central Tracking Chamber.

Section 2.2.4).

2.2.2 The Calorimeters

Calorimetry in the CDF detector comes in two types, hadronic and electromagnetic. In the top analysis, the calorimeters determine the energies of the jets, their directions, the event's $\not{E}_T$, and aid in the electron and muon selection.

The CDF calorimetry is arranged in $\eta - \phi$ segments called towers. Each tower projects back to the geometric center of the detector. The calorimeter can be split into four regions. Figure 2.4 shows the layout of the calorimeter in $\eta - \phi$ space. The central and endwall calorimeters cover $|\eta| < 1.1$, the plug calorimeter covers $1.1 < |\eta| < 2.4$, and the forward calorimeter covers the low angle region, $2.3 < |\eta| < 4.2$. The forward calorimeters are not used in the top search, except for in the determination of the $\not{E}_T$.

Central and End Wall Calorimeter

The central and endwall calorimeters are split into the electromagnetic (CEM) and hadronic (CHA, WHA) detectors. The CEM provides coverage in $|\eta| < 1.1$, and the combination of the CHA and WHA provide hadronic coverage over the same η. The electromagnetic calorimeter is constructed in alternating layers of lead and scintillator, while the hadronic calorimeter is iron and scintillator. Both the central and endwall calorimeters are segmented in $\Delta\phi = 15°$ wedges.

A single central calorimeter wedge is shown in Figure 2.5. Light from scintillator is fed by wave shifters from the scintillator to acrylic lightguides. The photomultiplier tubes that collect and measure the light are found at the back of the wedge. Resolution and other parameters of the central and endwall

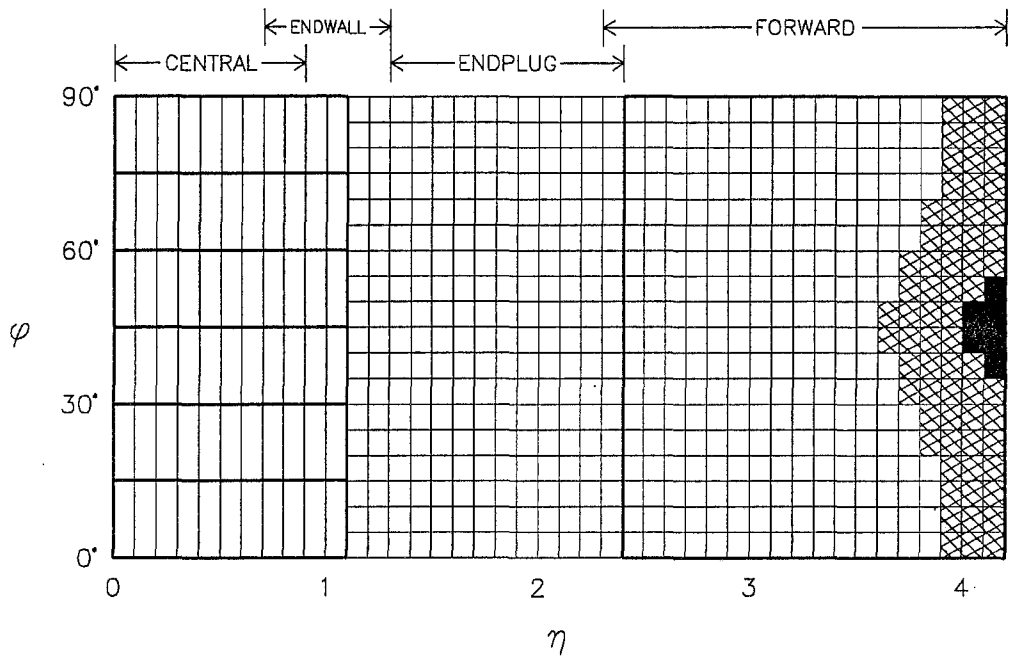

Figure 2.4: The tower segmentation and calorimeter coverage in $\eta - \phi$ space of the CDF detector. The hatched area has reduced depth coverage because room had to be made for the low beta quadrupole magnets. The solid sections have no coverage at all.

	Central (EM)	Central (Had)	Endwall (Had)
Coverage ($\|\eta\|$)	0 – 1.1	0 – 0.9	0.7 – 1.3
Tower Size ($\delta\eta \times \delta\phi$)	$0.1 \times 15°$	$0.1 \times 15°$	$0.1 \times 15°$
Module Length	250 cm	250 cm	100 cm
Module Width	15°	15°	80 cm
Number of Modules	48	48	48
Active Medium	SCSN-38 polytyrene Scintillator	PMMA doped Scintillator	PMMA doped Scintillator
Thickness	5mm	1.0 cm	1.0 cm
# Layers	21 – 31	32	15
Absorber	Pb	Fe	Fe
Thickness	1/8 in	2.5 cm	5cm
# Layers	20 – 30	32	15
Energy Resolution ($\sigma/E(Gev)$)	$13.5\%/\sqrt{E}$	11% (50 GeV π)	14% (50 GeV π)

Table 2.2: Characteristics of the central and end wall calorimeter.

calorimeters are detailed in Table 2.2.

Proportional wire chambers (CES) are located 6 radiation lengths into the central electromagnetic calorimeter. Six radiation lengths is the approximate position of the maximum electron shower deposition. Anode wires provide r-ϕ position information, and cathode strips provide the z information of electromagnetic showers.

Accuracy of the calorimeter is maintained to within $\pm 0.5\%$. Almost all of the CDF detector undergoes recalibration between $p\bar{p}$ stores, about once per day. Three different calibrations are employed for the central calorimeters, targeting specific parts of the data path from scintillator to phototube. This setup allows each section of the hardware to be independently checked and calibrated.

The response of the electromagnetic calorimeter was mapped during con-

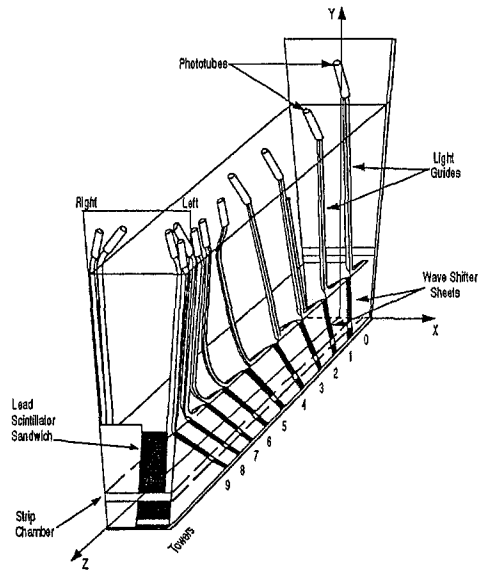

Figure 2.5: A single Central Calorimeter wedge. There are 12 wedges to an arch, and a total of four arches. The top of the wedge, in this picture, is positioned at the outside of an arch, radially.

struction, using a test beam. Also, $p\bar{p}$ collisions taken during the run are used to calibrate the calorimeters (Υ, Ψ, and $Z \rightarrow \mu\mu$ decays). The Υ and $\Psi \rightarrow \mu\mu$ decays are used to calibrate the momentum measurement. The calorimeter E distribution is calibrated by looking at $W \rightarrow e\nu$ decays and comparing the energy in the calorimeter with the momentum of the electron's track.

Plug Calorimeter

The plug calorimeter is used in this analysis to find the jet energy of forward jets, as well as aid in calculating the event's $\not{E}_T$. As with the central calorimeter, the plug calorimeter is split into hadronic (PHA) and electromagnetic (PEM) calorimeters. The active medium of the plug calorimeter is different from that of the central; it is a gas calorimeter. The PEM is made up of 34 layers of proportional tube chambers which use a 50%-50% gas mix of argon

	Plug (EM)	Plug (Had)
Coverage ($\|\eta\|$)	1.1 – 2.4	1.3 – 2.4
Tower Size ($\delta\eta \times \delta\phi$)	$0.1 \times 5°$	$0.1 \times 5°$
Active Medium	Proportional Chambers with cathode pads	
Tube Size (cm^2)	1.0×0.7	1.5×1.0
Absorber	94% Pb, 6% Sb	Fe
Thickness	0.48 cm	5.1 cm
Energy Resolution (σ/E at 50 GeV)	4%	20%

Table 2.3: Summary of the physical properties for the plug calorimeters.

and ethane as the active medium. Each tube contains a wire (the anode) at high voltage inside a resistive plastic tube. The cathode is made of copper pads mounted on G-10 board. The copper pads form the tower segmentation for the calorimeter. Table 2.3 lists the physical characteristics of the plug calorimeters.

Calibration for the plug calorimeter was done with a test beam of pions and electrons of known energy. Both pressure and temperature of the gas are monitored during operation because the gas calorimeter's response depends on the density of the gas. Response is monitored during the run with small proportional chamber tubes, containing an Fe^{55} source, mounted in the chambers, and small adjustments are made in the high voltage to keep the detector's gain constant. The calibration is checked with $Z \rightarrow e^+e^-$ data in situ.

2.2.3 The Muon Detectors

Central Muon Detector

CDF's central muon detectors (CMU) and central upgrade muon detectors (CMP) are used to detect high-P_T muons that signal a $W \rightarrow \mu\bar{\nu_\mu}$ candidate.

The CMU is located behind the central hadronic calorimeters (CHA) in the calorimeter wedges (see Figure 2.5). The CMU covers $|\eta| < 0.6$, with 85% ϕ coverage. The uninstrumented regions are due to gaps between detector modules. The lead and steel in the central calorimeters act as a filter for hadrons, preventing most non-muon particles from getting to the CMU (a non-muon is said to punch-through when it goes through the lead and steel colorimeter and leaves a signal in the muon chambers). The steel and lead amount to ≈ 5 absorption lengths.

Each drift cell of the central muon chamber is a rectangular aluminum box with a stainless steal resistive sense wire in the center. The chamber is operated in limited streamer mode. The gas is the same as used for the plug calorimeter, 50%-50% argon ethane, but with an additional 0.7% ethanol. The drift cells are grouped together into three modules. Each module has four layers, which contain four cells. Each layer is offset from the next by half a cell width.

Central Muon Upgrade Detector

In 1991 0.6 m of steel were installed for further hadron absorbtion, and an additional four layers of drift chambers were added behind the steel to detect muons. This new detector is called the central muon upgrade (CMP). For $|\eta| < 0.6$, 85% of the solid angle is covered by the CMU, 63% by the CMP, and 53% by both.

Muon detection was also extended in the $0.6 < |\eta| < 1.0$ rage with the addition of four free standing conical arches of drift tubes, called the central muon extension (CMX). The CMX covers 71% of the solid angle in the $0.6 < |\eta| < 1.0$ range, but was not used in this analysis.

The forward section of the detector, in the range $2 < |\eta| < 3.6$, is covered by the forward muon detectors. They are not used in this analysis due to

larger non-muon backgrounds and trigger inefficiencies.

2.2.4 The Silicon Vertex Detector

The Silicon Vertex Detector (SVX) was installed just prior to Run 1A. A recent publication [16] explains, in detail, the SVX's construction, operation, and performance.

The SVX resides at the center of the CDF detector, surrounding the beryllium beampipe (radius of 1.9 cm), and is supported by the surrounding VTX detector. The device consists of two barrels each 25.5 cm of active silicon in the z direction. Each barrel is built in 12 pie shaped wedges, and each wedge has four layers. On each layer of each wedge a ladder is mounted (see Figure 2.6). The silicon detectors are mounted on the rohacell carbon fiber supports that provide the mechanical structure for a ladder. Figure 2.7 is an isometric drawing of a ladder. The inner-most layer is mounted at a radius of 3.005 cm from the center of the beam pipe and the outer-most layer is mounted at a radius of 7.866 cm. The SVX has an η coverage of $|\eta| < 1.9$. There is an uninstrumented gap of 2.15 cm centered at $z = 0$, where the barrels join. Because the beam spread is 30 cm, the acceptance of the SVX is about 60%.

The detectors are high quality single-sided DC coupled detectors made from four inch silicon wafers. The bulk silicon is n-doped, and 300 μm thick. p-doped channels run along the surface length wise, and Al readout strips (to carry away the charge) are mounted on the p-doped channels:

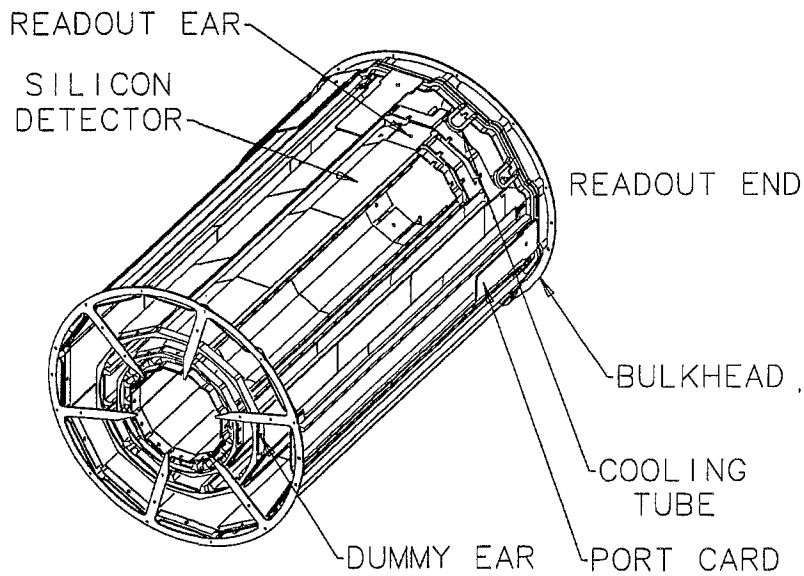

Figure 2.6: One of the two SVX barrels. The barrel is split into 12 pie shaped wedges, and each wedge has four layers. Each layer of each wedge has a ladder on which three silicon detectors are mounted.

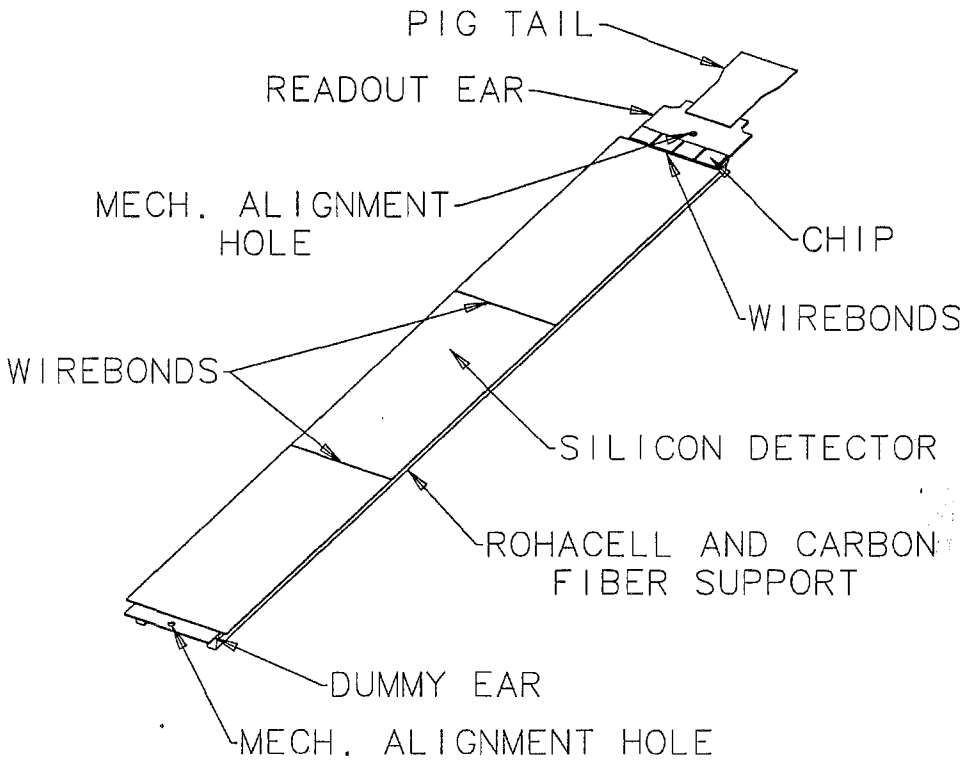

Figure 2.7: One of the 96 ladders in the SVX. The ladders are stacked into four layers, a wedge. 12 wedges make up each of the two barrels of the SVX.

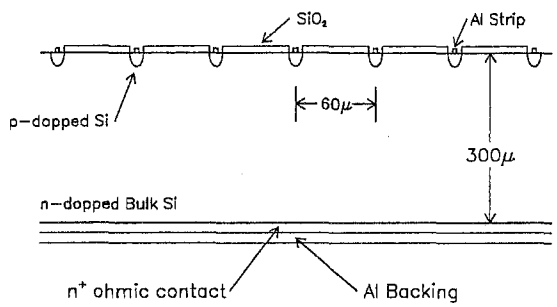

The ladder has a strip pitch of 60 μm for the inner three layers, and a 55 μm strip pitch for the outer layer. The strips are kept at electrical ground and the backing plate is biased to reverse bias the n-p junction between the p-doped channel and the n-doped bulk Si.

There is a small inactive area (no silicon) at each end of the ladder called the ear. A hybrid which holds two to six SVXD amplifier chips is mounted on the far ear, at $z = \pm 25.5$ cm. Each readout strip is wire bonded to the hybrid. The SVXD chips perform charge integration, pedestal subtraction, and amplification of the charge deposited on each strip. Each chip handles 128 strips (channels). The four ladders in each wedge are connected to a kapton cable that connects to a port card mounted on the bulkhead at the outer radius of the wedge. The port card contains the interface to the external digitizers as well as the ladder control logic (clocking signals, etc.).

The SVX has 46080 channels, which is about one third of the readout channels in the entire CDF detector. Physics events typically have an occupancy of 7% in the SVX, so zero channel suppression is implemented in the SVXD chip to reduce the readout time. Digitizers in crates mounted on the CDF detector, but far from the SVX itself, read out the barrel. The digitizers are controlled by the SVX sequencers, which feed the sparse data to rest of the CDF data acquisition system. Typical readout times are 1-2 ms, depending upon event complexity. A water cooling system pulls the heat away from the

detector. Unsafe operation is prevented through the use of a interlock system. Details of both the cooling and interlock systems for the SVX can be found in Appendix A.

2.2.5 The Trigger System

The proton and antiproton beams cross almost 300,000 times a second at the B0 interaction point. CDF's data recording system, 8 mm tape based, is only capable of writing 5 to 10 events per second. This means the CDF trigger system must eliminate about 9,990 events every second.

The CDF trigger is a three level system. Each level is a logical 'OR' of several triggers constructed to select events containing electrons and muons, or other physics particles. The central muon and central calorimeter detectors have two sets of data outputs. The main outputs feed the readout electronics and are only digitized if the CDF trigger system decides the event is worth further investigation. The second set of outputs, called the fast-outs, are used by the lowest level of the trigger system. Unlike the real readout, the fast-outs make their data available immediately (2.5 μs after beam crossing), at the expense of accuracy and full charge collection. The calorimeter information is summed into towers $((\delta\eta = 0.2) \times (\delta\phi = 15°))$ for the electromagnetic and hadronic calorimeters. The Level 1 trigger uses this information to look for large E, or muons, or jet formation in the detector. Typical level 1 trigger rate when the luminosity is 5×10^{30} pb^{-1} is 1 KHz, and it makes it decision in the 3.5μ s between beam crossings: it is dead-timeless.

The level 2 trigger makes more sophisticated use of the calorimeter information. A hardware nearest-neighbor cluster-finder creates a list of calorimeter clusters along with the cluster's E_T, average η, and average ϕ. The central fast

tracker (CFT) supplies a list of r-ϕ tracks. The CFT uses CTC hits as input and its momentum resolution is $\frac{\delta P_T}{P_T} \approx 0.035 \times P_T$. For tracks with a P_T greater than 10 GeV/c the CFT is 93.5 $\pm$ 0.3% efficient. Track segment information (also called track stub information) is also available from the CMU, CMP, and CMX detectors. Electron candidates are formed by matching highly electromagnetic calorimeter clusters to CFT tracks and muon candidates are formed by matching CFT tracks to muon track stubs. A typical output rate of the Level 2 trigger is 100 Hz when the luminosity is 5×10^{30} pb^{-1}, incurring only 5-10% deadtime.

The Level 3 trigger is a software reconstruction trigger. Silicon Graphics multi-cpu Power Servers (with the ability to perform one billion instruction per second, or 1000 MIPS) run a version of the CDF offline reconstruction with two dimensional tracking (instead of three dimensional). A typical output rate is 5-10 Hz. All events passing level 3 are stored on tape.

2.3 Data Reconstruction

The reconstruction of the raw data and identification of charged particles (e, μ, jets, etc.) is quite complex and requires a large amount of time (CPU) and care (people) to keep it running smoothly. During Run IA the system performed quite well, often making an initial version of the reconstructed data for certain triggers (i.e. high-P_T lepton trigger) available 24 hours after it had been collected. The final production run uses a large farm of IBM R/6000 computers. The rest of this section is a brief discussion of some of the reconstruction algorithms key to this analysis.

Jets are formed by finding clusters of energy in the calorimeter. The E_T of a jet is all the energy within a cone of $\eta = 0.4$ around the found cluster[17].

This applies both in the electromagnetic and hadronic calorimeters.

Track reconstruction is quite complex. The hardest task is to find three dimensional tracks in the CTC. Track stubs are found in each of the 9 superlayers (5 axial, 4 stereo). They are linked together into a three dimensional track, the stereo layers providing z information and the axial layers providing r-ϕ information. The CTC's excellent position resolution allows very precise measurement of the P_T of a track, $\frac{\delta P_T}{P_T} = 0.0010 \times P_T$ for tracks at 90°.

The SVX reconstruction algorithm first clusters SVX hits, a process not unlike jet clustering. A charged particle moving through the SVX may leave as many as two or three hits on a layer. The hits are clustered together, and their charge-weighted position is used in the subsequent track reconstruction algorithm. SVX tracks are constructed one cluster per layer at a time. CTC tracks are extended into the fourth layer of the SVX. The track finder adds a nearby cluster to the track fit, and updates the tracking parameters. This process is repeated for each layer of the SVX, working inwards. Because the direction of the track is measured better at each consecutive each step, the number of candidate clusters near the track decreases at each layer. All combinations of candidates are tried, and the combination with the smallest SVX-CTC track χ^2 is chosen (see Figure 2.8). This process may create a track with some layers having no clusters attached to the track.

The SVX track reconstruction, further, does not prevent two different CTC tracks from using the same SVX clusters. When this happens, a cluster is said to be *shared.* From the point of view of a secondary-vertex finder, the tracks are suspect, as it is unlikely that the two tracks did actually intersect in the SVX. Clusters may also contain strips that no longer function, called *dead strips.* The dead strips degrade the cluster and therefore the track resolution. In general good tracks are required to have at least two unshared clusters

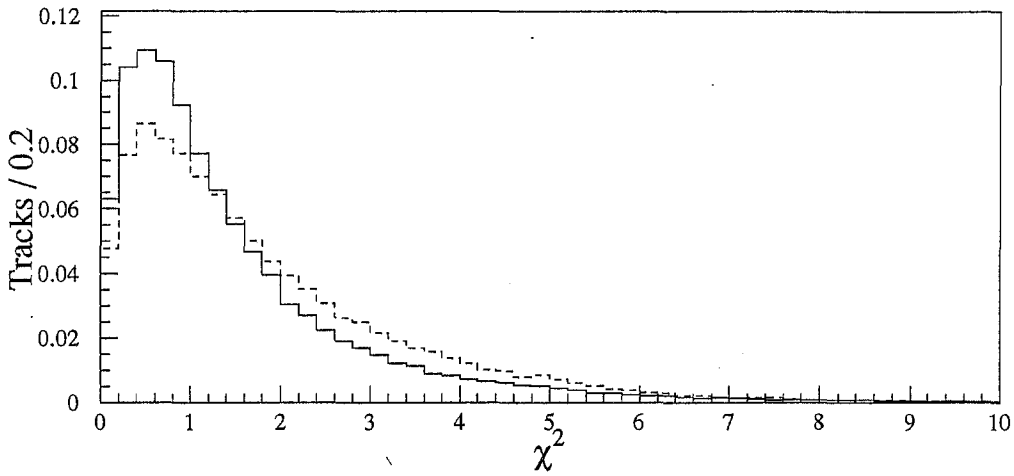

Figure 2.8: The SVX-CTC track χ^2 for found tracks in data (solid histogram) and in a Monte Carlo simulation (dashed histogram).

containing no dead strips.

To achieve the resolution needed to make the secondary-vertex search viable, the device must be carefully aligned. A large collection of high-P_T tracks from $p\bar{p}$ collisions are used for the alignment. Wedge alignment is performed by fixing the wedge's third layer and allowing the others to float. High-P_T tracks, which bend little in the magnetic field, are used to determine if each layer is offset. This is done by comparing the residual (the distance from the cluster to the track) for that layer, both when the layer is in the track fit and when it is not in the fit. Figure 2.9 shows the SVX's impact parameter resolution as a function of track P_T.

Finally, a primary vertex is found in the event. This is also done using an iterative process. The average beam position is used as a seed. All tracks which have $|d|/\sigma_d < 3.0$ relative to the beam spot are constrained to a common point. A residual is calculated for each track by removing the track from the vertex fit, and measuring the impact parameter relative to the fit vertex. If

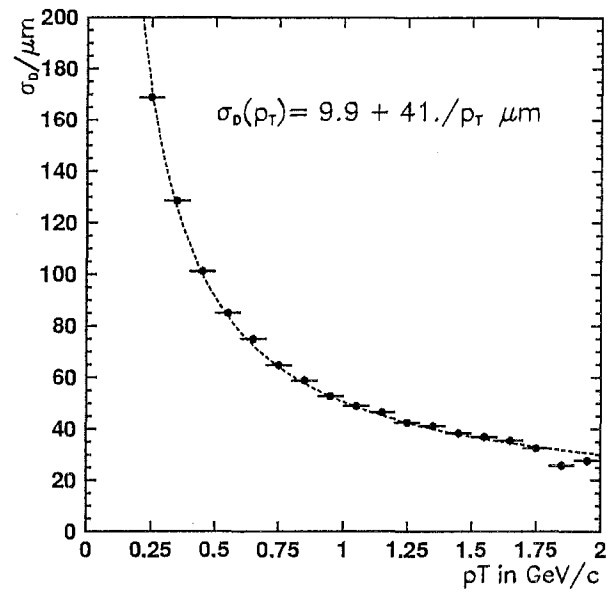

Figure 2.9: The impact parameter (d) resolution for SVX tracks as a function of track's P_T.

$|d|/\sigma_d > 3.0$, the track is removed from the fit. This process is repeated until all tracks satisfy the $|d|/\sigma_d$ requirement. No track with a $z > 5$ cm from the primary vertex is used in this analysis. The x and y resolution of the primary vertex fit is on the order of 15 μm (see Figure 2.10). The vertex is discarded if the resolution is greater than the size of the beam spot (36 μm). Events without a found primary vertex are not used in this analysis.

This analysis looks for secondary vertices displaced a small distance in the x-y plane (millimeters) from the primary interaction point. It is important that tracks due to a second interaction in events with multiple interactions be excluded from secondary-vertex reconstruction. The second interaction may not have the same x-y coordinate because the beam slopes about 4.5 μm/cm over the length of the SVX in both x and y directions, and will displace a second interaction enough for it to be tagged as a secondary vertex if it is a

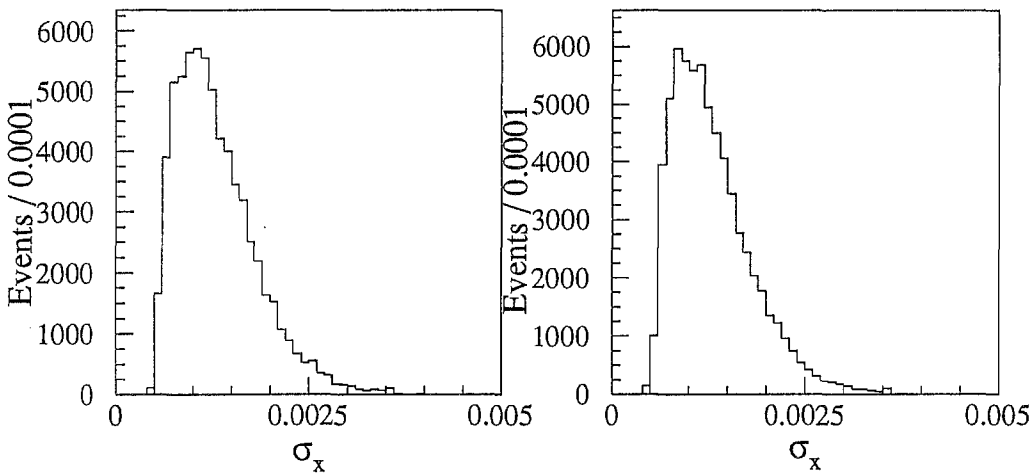

Figure 2.10: The x and y resolutions of a fit primary vertex.

significant distance away in z from the primary interaction point.

Chapter 3

The Event Samples

The top analysis uses several different data samples. Their descriptions are gathered here so that the subject matter of later chapters is not confused by discussions of data sample selection and purity. The primary data samples are:

1. the JET50 data sample, a large collection of typical (*generic*) jets,
2. the ICE sample, a large collection of inclusive central electrons,
3. and the $W+\geq 3$ jet sample.

All data are processed with the standard CDF offline software. All Monte Carlo samples, unless otherwise noted, are simulated with the full CDF detector simulation package (CDFSIM), and then processed with the same CDF offline software as the data. B hadron branching ratios in the Monte Carlo simulations are made to match the results of the CELO collaboration's B hadron branching ratio measurements by running generated events though a software module called CLEOMC[18]. SVX cluster data is smeared in post processing to make it more closely match the cluster resolutions and cluster lengths found

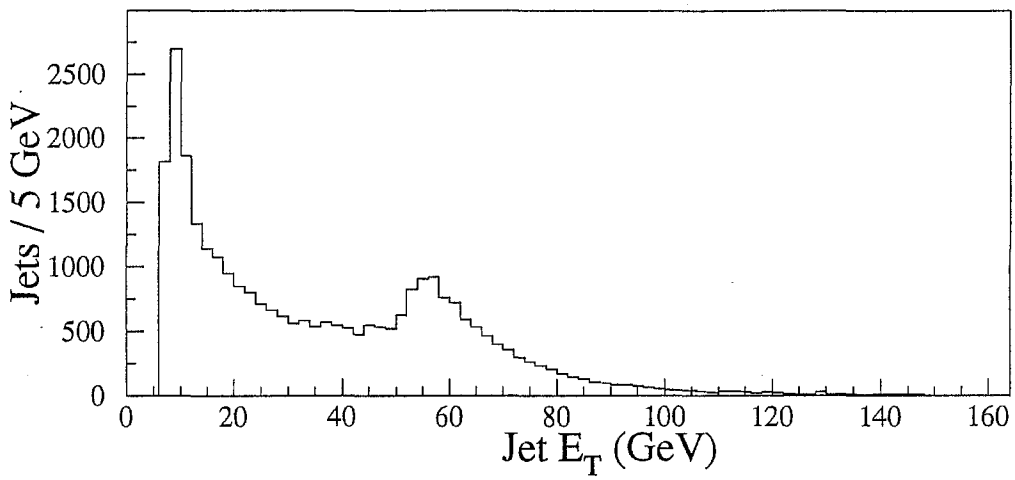

Figure 3.1: The E_T spectra of the JET50 sample. One jet with E_T>50 GeV or more is required by the trigger in each event. This trigger causes the second peak in the sample. Jets with E_T less than 50 GeV are volunteers in multijet events.

in the data. Specifics of Monte Carlo generation are described as needed in later chapters.

3.1 The Generic Jet Sample

All events in the generic jet sample are required to pass the 50 GeV jet trigger (the JET50 sample). Offline, the events are also required have a z vertex within 30 cm of the center of the CDF detector, and at least one jet with jet $E_T > 15$ GeV and $|\eta| < 2.0$. This sample is about 67,000 events containing 137,000 jets with jet $E_T > 15$ GeV. Most of the jets are light quark (u or d quarks) and gluon jets. The sample is used to study background rates in b-tagging because of the small heavy flavor content. In Section 5.1 a determination of the JET50 sample's heavy flavor content is made. Figure 3.1 is the jet E_T spectra of the JET50 sample.

The JET20 (JET100) sample is the same except events are required to satisfy the 20 GeV (100 GeV) jet trigger.

3.2 The Inclusive Central Electron Sample

The Inclusive Central Electron sample (the ICE sample) is made up of low P_T electrons passing the selection criteria listed in Table 3.1. The E/P requirement forces the energy measured in the calorimeter be close to the momentum of the track pointing at the calorimeter. Most of the calorimeter energy is required to be electromagnetic, instead of hadronic, by the $\frac{\text{Had}}{|\text{EM}|}$ requirement. The E profile of adjacent calorimeter towers is required to be similar to the profile made by test beam electrons (the LSHR requirement).

The electron track is required to match hits in the Central Electromagnetic Shower chamber (CES). The shower shape is required to match test beam shower shapes in both the cathodes and wires (χ^2_s and χ^2_w requirements). The Z_v requirement requires the event vertex to be close to the center of the detector and the $|Z_v - Z_0^e|$ requirement makes sure that the electron track came from the event's primary vertex. Finally, fiducial requirements remove electrons that are near calorimeter module boundaries.

The ICE sample contains a substantial number of B hadrons that decay semileptonically. The sample is used to determine the efficiency of the b-tagging algorithm (see Section 4.2).

The fraction of ICE sample events containing a B hadron, F_b, must be determined to calculate the efficiency of the b-tagging algorithm. F_b is determined by looking for oppositely signed e-μ pairs, one the primary lepton from the B hadron decay, and the second lepton from the B quark's charm decay

$E_T > 9$ GeV
E/P < 1.5
$\frac{\text{Had}}{\lvert\text{EM}\rvert} < 0.05$
LSHR < 0.2
Track Strip Matching:
$\lvert\delta x\rvert < 1.5$ cm
$\lvert\delta z\rvert < 3.0$ cm
$\chi^2_s < 10$
$\chi^2_w < 10$
$\lvert Z_v\rvert < 60$ cm
$\lvert Z_v - Z_0^e\rvert < 5$ cm
Fiducial Requirements

Table 3.1: The selection requirements for a good ICE electron.

(a soft lepton). For example,

$$B_x \rightarrow e^- \bar{\nu}_e D X$$

followed by the charm decay

$$D \rightarrow \mu^+ \bar{\nu}_\mu X.$$

The electron from the B hadron decay will be the trigger electron in an ICE event. The soft muon from the charmed hadron will have the opposite charge of the trigger electron. Also, the combined mass of the unlike-sign e-μ system is constrained to be less than the B hadron mass. F_b can then be calculated as follows:

$$N_{el} = N_e^B \times Br(D \rightarrow \ell X) \times \epsilon_\ell,$$

$$F_b = \frac{N_e^B}{N_e},$$

where N_{el} is the number of unlike-sign leptons from B hadron decay, ϵ_ℓ is

$P_T <$ GeV/c
$E_{HAD} < 5$ GeV
$E_{EM} < 2$ GeV
$\frac{\lvert\delta x\rvert}{\sigma_x} < 3.0$
$\frac{\lvert\delta z\rvert}{\sigma_z} < 3.0$

Table 3.2: The selection requirements for a good soft muon. E_{HAD}, the hadronic calorimeter energy and E_{EM}, the electromagnetic calorimeter energy, both refer to only the tower the muon goes through. δx and δz refer to the difference is distance between a matched CTC track and the muon stub.

the lepton reconstruction efficiency, and $Br(D \rightarrow \ell X)$ is the average charmed hadron to lepton branching ratio. N_e is the total number of good electrons in the ICE sample.

The CDF detector is slightly more efficient at finding soft muons because the isolation requirement on a good electron is not efficient in the busy jet environment typical of a B hadron decay. F_b is measured by looking for the decay $B \rightarrow e\nu DX$ followed by $D \rightarrow \mu X$; the decay $B \rightarrow \mu\nu DX$ is not used. A candidate soft muon is required to satisfy the requirements listed in Table 3.2

The like-sign e-μ pairs are used to measure the background rate for this process. A comparison of like-sign and unlike-sign e-μ mass combinations shows a significant excess in the unlike sign combination below 5 GeV/c^2 (see Figure 3.2). Table 3.3 shows the numbers of e-μ combinations for the ICE sample when mass region is restricted to below 4 GeV/c^2.

Considering only the $D \rightarrow \mu X$ decay, F_b is written as

$$F_b = \frac{N_{e\mu}}{Br(D \rightarrow \mu X)\epsilon_\mu} \frac{1}{N_e}.$$

Monte Carlo simulation studies show ϵ_μ to be 0.81 ± 0.12, and $Br(D \rightarrow \mu X)$ has been measured to be 10.3 ± 0.3[19]. The total number of electrons used for

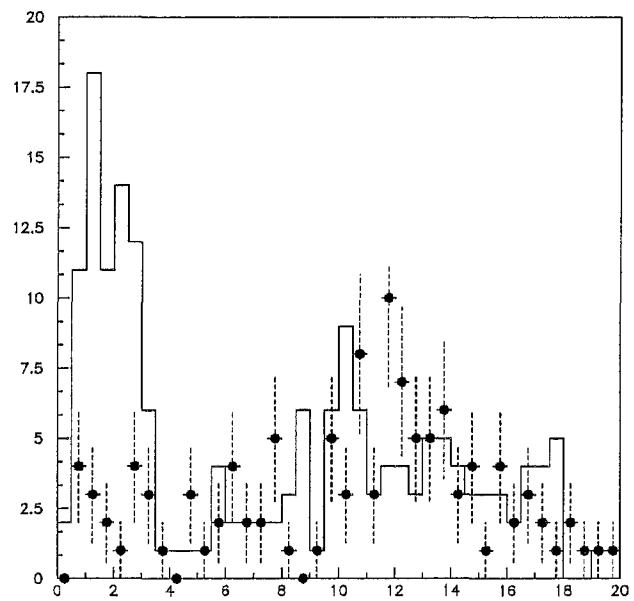

Figure 3.2: Mass of unlike-sign (solid histogram) and like-sign (points) e-μ pair. Bins below 4 GeV/c^2 are used to determine the number of e-μ pairs due to B hadrons by subtracting the like-sign from the unlike-sign distribution.

Unlike Sign e-μ pairs	75 ± 8.7
Like Sign e-μ pairs	18 ± 4.2
Excess unlike sign	57 ± 9.7

Table 3.3: The numbers of like-sign and unlike-sign e-μ combinations with a mass less than 4 Gev/c^2 in the ICE sample. Uncertainties are statistical only.

this study is 18975. F_b is calculated to be $(37.2 \pm 8.1)\%$, where the uncertainty is statistical only.

Major sources of systematic uncertainty are, first, the branching ratio of $D \rightarrow \mu X$, where D is any charmed hadron. While the individual branching ratios are known for the most charmed hadrons, the branching ratio of a mix of charmed hadrons is unknown. A second source of systematic uncertainty is the background subtraction. The assumption is made that the excess of e-μ pairs with masses below 4 GeV/c^2 is due to B hadron decays, however it may be due to some local charge correlation (kaon and pion decay in flight, for example). The effects are expected to be smaller than the already large uncertainty in F_b:

$$F_b = (37 \pm 8)\%$$

It is important to note that F_b only enters into the calculation of the top acceptance and the cross section, and not into the calculation of the significance of the evidence for top.

3.3 High P_T Lepton Identification

The high-P_T electron selection criteria are listed in Table 3.4. The criteria are similar to the electron selection criteria in the ICE sample. Table 3.5 lists the selection criteria a candidate high-P_T muon is required to satisfy. The D_0 requirement refers to the muon track's impact parameter. The track stub matching requirements assure that the muon's CTC track propagated out to the muon chambers matches with a reconstructed muon stub.

Trigger acceptance and identification efficency for high-P_T leptons is measured using data. A study of $Z \rightarrow ee$ events shows the electron requirement

$E_T >$ 20 GeV
E/P < 1.5
$\frac{\text{Had}}{\lvert\text{EM}\rvert} < 0.05$
LSHR < 0.2
Track Strip Matching:
$\lvert\delta x\rvert < 1.5$cm
$\lvert\delta z\rvert < 3.0$cm
$\chi^2_s < 10$
$\lvert Z_v\rvert < 60$ cm
$\lvert Z_v - Z_0^e\rvert < 5$ cm
Fiducial Requirements

Table 3.4: The high-P_T electron selection criteria.

$P_T >$ 20 GeV/c
EM Energy < 2.0 GeV
HAD Energy < 6.0 GeV
$D_0 < 0.3$ cm
$\lvert Z_v\rvert < 60$ cm
$\lvert Z_v - Z_0^e\rvert < 5$ cm
Track Stub Matching:
CMU: $\lvert\delta x\rvert < 2.0$ cm
CMP: $\lvert\delta x\rvert < 5.0$ cm
CMX: $\lvert\delta x\rvert < 5.0$ cm

Table 3.5: The high-P_T muon selection criteria.

to be $(84 \pm 2)\%$ efficient. The same requirement is slightly more efficient when applied to a Monte Carlo simulation, the scale factor is 0.89 ± 0.04. The scale factor is applied when the Monte Carlo is used to calculate a selection requirement efficiency for high-P_T leptons.

Muon trigger and identification efficiency is found in much the same way. A sample of $Z \rightarrow \mu\mu$ is used to find a muon selection efficiency of $(90.6 \pm 1.4)\%$. Cut efficiencies found in Monte Carlo events must be scaled by 0.84 ± 0.03 to match the selection efficiency observed in data for high-P_T muons.

3.4 The W Sample

W candidate events are selected by looking for the $W \rightarrow \ell\bar{\nu}$ decay. The signature is a high-P_T lepton and large missing energy in the event ($\not{E}_T$). Only the $W \rightarrow e\bar{\nu}$ and $W \rightarrow \mu\bar{\nu}$ final states are used because of difficulties associated with τ detection.

Additional requirements are made on events with a high-P_T lepton to assure W purity. They are:

- The lepton is required to be well isolated from other particles. Isolation is defined as

$$I = \frac{E_T^C - E_T}{E_T}$$

  where E_T^C is the calorimeter energy in a cone of radius $R = \sqrt{\delta\eta^2 + \delta\phi^2} = 0.4$, centered on the electron cluster. In the case of muons, the calorimeter energy requirement is similar, except the energy removed from the muon cluster is the minimum ionizing energy for the muon. Good W candidates events are required to have $I < 0.1$. This requirement removes backgrounds from sources like $b\bar{b}$, where the electron will be part

of a B hadron jet, and thus nonisolated. The isolation requirement is 77% efficient for top events in the electron sample, and 81% efficient for top in the muon sample. The efficiencies are determined with Monte Carlo simulations.

- Z bosons are removed (see Section 3.5).

- Photon conversions are removed. Conversions are identified by the following selection criteria:

  - The angle relative to the z axis, the dip angle, for the two photon tracks are required to be the same, because they come from a massless object and the magnetic field will not separate the tracks in dip angle. The requirement used is $|cot(\Delta\theta)| < 0.03$.

  - The separation of the two tracks at the point of their closest approach is required to be less than 0.3 cm.

  - The invariant mass of the two tracks is required to be less than 500 MeV/c^2.

  - The distance from the beamline to the conversion happens is required to be less than 50 cm. This makes sure the conversion doesn't occur in the gas volume of the CTC where there is very little material and thus the ratio of true conversions to false conversions is small.

  The conversion requirement removes (5±2)% of the events in the high-P_T electron sample.

- $\not\!\!E_T >$ 20 GeV (the $\not\!\!E_T$ is corrected for high-P_T muons in the event before this requirement is applied).

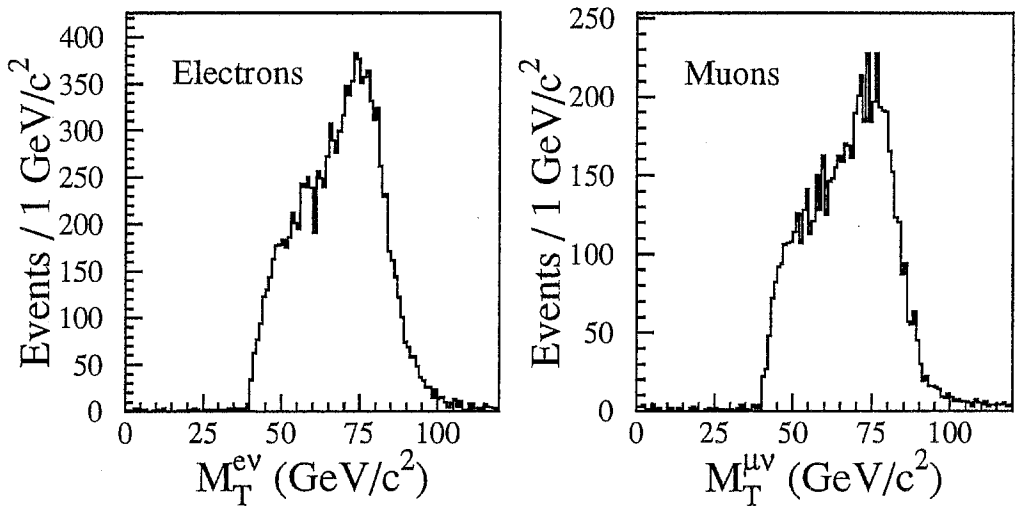

Figure 3.3: The transverse mass distribution for $W \rightarrow e\bar{\nu}$ and $W \rightarrow \mu\bar{\nu}$.

Figure 3.3 shows the transverse mass for the high-P_T electron and muon W's. A clear Jacobian peak can be observed at the W mass, 80 GeV/c^2.

Table 3.6 lists the numbers of high-P_T leptons passing the W selection criteria. A good jet in the W sample is defined as a jet with $E_T > 15$ GeV and $|\eta| < 2.0$. Table 3.7 describes how the W candidates are distributed in jet multiplicity, and Figure 4.10 shows this table graphically.

Selection Criteria	Electrons	Muons
Good Lepton	28,522	17,994
Lepton Isolation	20,420	11,901
Z Removal	18,700	11,310
$\not{E}_T >$ 20 GeV	13,657	8,724
Good Quality Run	12,797	8,272
Good Trigger	11,949	7,024

Table 3.6: The number of events passing the W sample selection criteria. The Good Lepton requirement includes all quality selection, fiducial requirements, E_T requirements, and conversion removal.

Jet Multiplicity	Electron Events	Muon Events
0 Jet	10,663	6,264
1 Jet	1058	655
2 Jets	191	90
3 Jets	30	13
$\geq$ 4 Jets	7	2

Table 3.7: The final W sample as a function of jet multiplicity. Each jet is required to have $E_T \geq$ 15 GeV and $|\eta| < 2.0$. The signal region consists of all events with 3 or more jets.

The W+jet sample is not 100% pure W bosons. The non-W contamination consists of QCD jet events and semileptonic $b\bar{b}$ events. To estimate the non-W background in the signal sample a $\not{E}_T$ *vs.* I scatter plot is divided into four regions:

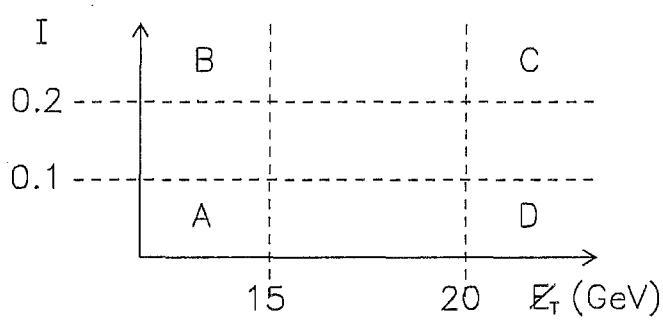

The signal region is D, where the lepton is isolated and the event has large $\not{E}_T$[20]. Since the low $\not{E}_T$ region, B, is mostly non-W events, like $b\bar{b}$, the non-W contamination of the signal sample can be written as

$$D = \frac{A}{B} \times C,$$

assuming that $\not{E}_T$ and I are uncorrelated. This predicts 10$\pm$5% non-W events in the W+jet data sample.

Other production mechanisms that may pass the W+jet selection requirements are calculated using Monte Carlo methods. $W \rightarrow \tau\nu$ represents about

Background Source	Background Estimate
QCD and $b\bar{b}$	5.2 ± 2.6
WW, WZ, and ZZ	2.6 ± 1.2
$Z \rightarrow \tau\tau$	1.7 ± 0.5
$Z \rightarrow \mu\mu$	1.5 ± 0.4
$Z \rightarrow$ ee	1.2 ± 0.6
Total	12.2 ± 3.1

Table 3.8: The expected background contributions in the $W+ \geq 3$ jet sample due to non-W, Z, and divector boson sources. The uncertainty in the total background takes into account the correlations in uncertainties in the various background sources.

4% of the events in the W sample, and $Z \rightarrow \tau\tau$, $Z \rightarrow \mu\mu$, and $Z \rightarrow ee$ about 8% of the total. The $Z \rightarrow ee$ and $Z \rightarrow \mu\mu$ contributions are calculated by first estimating the ratios $\frac{Z \rightarrow ee}{W \rightarrow e\bar{\nu}}$ and $\frac{Z \rightarrow \mu\mu}{W \rightarrow \mu\bar{\nu}}$. The ratios are then applied to the observed number of W+jet data to determine the number of $Z \rightarrow ee$ and $Z \rightarrow \mu\mu$ events. Table 3.8 lists the expected contributions in the $W+ \geq 3$ jet sample.

3.5 The Z Sample

Z boson events make an excellent control sample for this analysis. Most of the heavy flavor production mechanisms that appear in the W sample will also appear in the Z sample, except for $t\bar{t}$ production. The other important reason to find events containing Z bosons is to remove them from the signal sample, as they are known not to contain any top.

Events containing $Z \rightarrow ee$ and $Z \rightarrow \mu\mu$ are looked for in the high-P_T lepton sample (isolation, trigger, and good quality run requirements applied). A second electron or muon is required in the event (Table 3.9 and Table 3.10

$E_T > 10$ GeV
$E/P < 2.0$
$\frac{\text{Had}}{\lvert\text{EM}\rvert} < 0.12$
$I < 0.1$

Table 3.9: Selection criteria for the second electron in a $Z \rightarrow ee$ event.

describe the slightly looser cuts on the second electron and muon, respectively). Additionally, a requirement is made on the invariant mass of the two leptons,

$$70 \text{ GeV/c}^2 < M_{ll} < 110 \text{ GeV/c}^2.$$

There are 2311 Z bosons in the high-P_T lepton sample. The loss in top acceptance due to Z boson removal is small, on the order of a few percent.

Studies on the b-tag rates in the Z sample require a high statistics Z sample that is very pure. For purity reasons, the mass requirement is tightened to

$$75 \text{ GeV/c}^2 < M_{ll} < 105 \text{ GeV/c}^2.$$

To improve the statistics in the Z+jets sample, the E_T requirement is loosened to E_T>10 GeV for the second lepton. The isolation requirement on the second lepton is $I_{cal}/E_T < 0.1$, where I_{cal} is the calorimeter isolation which is defined as the transverse energy in the towers within a cone radius R=0.4, centered on the electron, but excluding the electron cluster's energy. This cut is more than 90% efficient for Z boson events. The Z boson sample used to study the tagging rate consists of 202 $Z+ \geq 1$ jet events.

$P_T >$ 15 GeV/c
$\|\eta\| < 1.1$
Track Strip Matching:
CMUO $\|\delta x\| < 5$ cm

Table 3.10: Selection criteria for the second muon in a $Z \rightarrow \mu\mu$ event.

Chapter 4

The b-Tagging Algorithm

We begin the search for top by defining a signal sample requiring at least three or more jets, as previously defined, in the W+jet sample. This selection is motivated by Figure 4.1, which shows the jet multiplicity of $t\bar{t}$ events in a Monte Carlo simulation. The expected jet multiplicity peaks near three jets. QCD W events have a steeply falling jet multiplicity distribution (see Table 3.7). The resulting W+jet sample contains 52 events. 75% of $t\bar{t}$ events in a Monte Carlo simulation pass this requirement, but less than 0.5% of the W background pass the same requirement. Other kinematic variables were examined to further reduce the W+jet background; however none had both the ability to separate signal from background and the simplicity of the 3 jet requirement[21]. Further kinematic restrictions in addition to the 3 jet requirement were also tried, but found to be too inefficient in the $t\bar{t}$ signal.

The requirement of three or more jets in a W candidate event does not sufficiently reduce the background such that a top quark signal can be detected in the lepton+jets channel. The presence of a b-quark in the $t \rightarrow Wb$ decay is a powerful discriminator since every $t\bar{t}$ pair is accompanied by 2 b-quarks and very few $W+$ jet events are accompanied by heavy flavor (about 4%)[13].

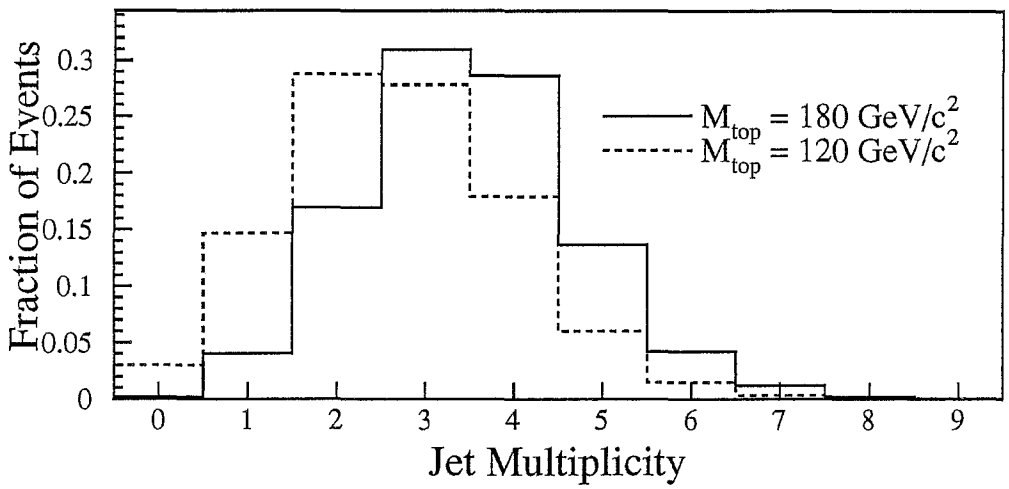

Figure 4.1: The Fraction of events passing the W selection criteria in a $t\bar{t}$ Monte Carlo simulation with M_{top}=120 GeV/c^2 (dashed histogram), and a $t\bar{t}$ Monte Carlo simulation with M_{top}=180 GeV/c^2 (solid histogram), as a function of the number of jets in the event, N_{JET}.

Tagging the b-jet provides the needed extra background rejection without a large sacrifice in the efficiency for the $t\bar{t}$ signal.

Two methods for tagging b-jets are used in CDF's recently completed top search analysis: a soft-lepton finder and a secondary-vertex finder[2]. The soft-lepton analysis tags a b jet by searching for the soft lepton from a semileptonic $B \rightarrow \ell X$ decay. Reference [2] contains further details of this analysis. The secondary-vertex method of b-tagging is the subject of this thesis.

The secondary-vertex algorithm is designed to find decay vertices displaced from the $p\bar{p}$ collision point (called the primary vertex). Both the t-quark and the W boson decay quickly (lifetime, $\tau \sim 10^{-23}$s), and if the t-quark mass (M_{top}) is greater than 130 GeV/c^2 it may decay so quickly that it does not form a T hadron[10]. The b quark, however, is long lived and does hadronize, forming a B hadron along with a number of other hadrons (pions, kaons, etc.). Figure 4.2 is a cartoon of a typical B hadron decay as it might look in the CDF

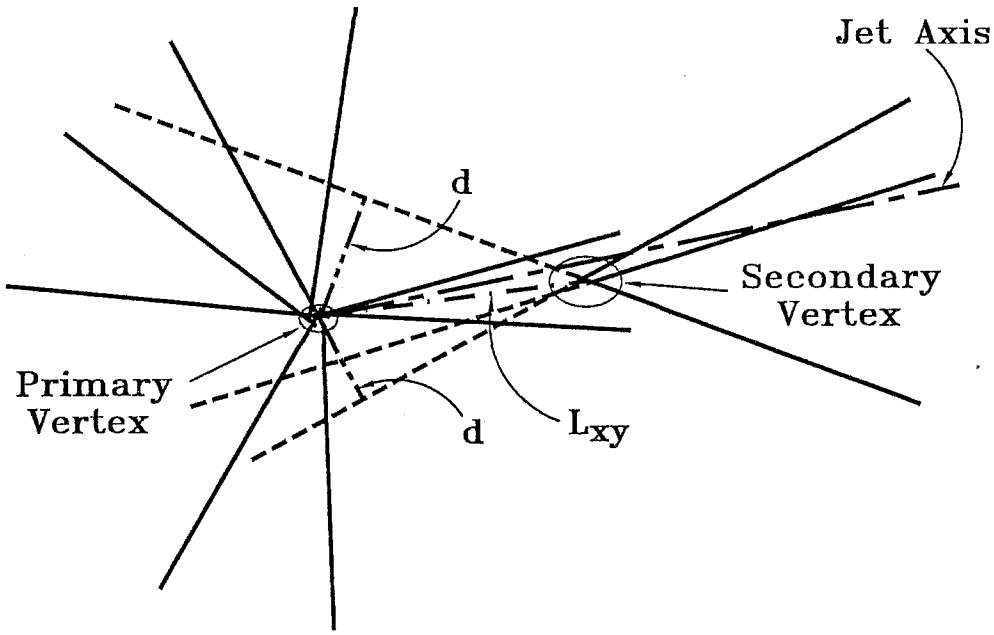

Figure 4.2: Cartoon depicting a t-quark decay. The b-quark fragments, creating a number of tracks, and a B hadron. The B hadron travels a short distance, L_{xy}, before it decays as well. The decay products are used to reconstruct the position of the secondary vertex.

detector. The distance between the primary vertex and the B hadron decay (secondary vertex) is called the 2d decay length (L_{xy}), as shown in Figure 4.2. The world average lifetime of the B hadron is $c\tau = 453\ \mu m$[11]. Figure 4.3 is a distribution of L_{xy} for B hadrons created by a t-quark decay simulated with the ISAJET Monte Carlo program. The B hadron's long lifetime and large boost mean it can travel a measurable distance from the primary vertex before it decays.

The position of the secondary vertex is reconstructed from the decay products of the B decay. The success of the reconstruction depends on the ability to resolve the secondary vertex from the primary vertex. It was impossible to

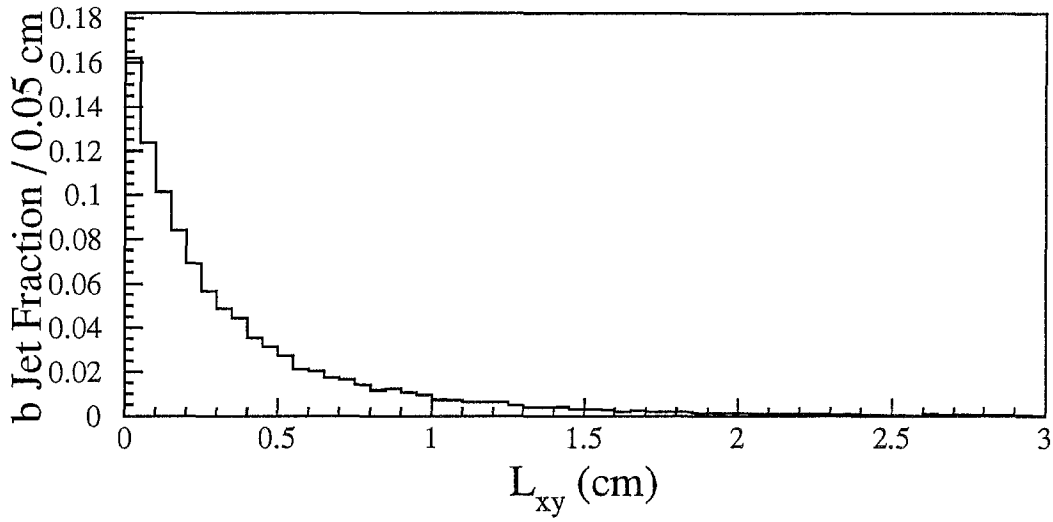

Figure 4.3: The L_{xy} distribution for B hadrons created by t-decays in ISAJET Monte Carlo generated events. Detector effects are removed.

distinguish the secondary vertex from the primary vertex with a high efficiency before Run IA because the CTC has insufficient spatial resolution. The SVX, installed for Run IA, is designed to have the spatial resolution required to do a secondary-vertex search.

4.1 The JETVTX Algorithm

The secondary-vertex finding algorithm used by CDF is called JETVTX, short for Jet Vertex. The secondary vertex algorithm is most efficient for highly boosted B hadrons because L_{xy} is likely to be large. Highly boosted B hadrons are also more likely to deposit energy in the calorimeters. It therefore makes sense to use a jet based algorithm to search for secondary B hadron decay vertices.

The JETVTX algorithm is seeded with jets having jet $E_T >$ 15 GeV/c and $|\eta| < 2.0$ A list of tracks satisfying the requirement $\cos(\theta) < 0.8$ is associated

with each jet, where θ is the opening angle between the jet axis and the track in the x-y plane. Only tracks which satisfy the following requirements are considered:

- The track is required to have hits on at least two stereo superlayers and two axial superlayers of the CTC. A good CTC track is necessary because it is the starting point for SVX track reconstruction (see Section 2.3).

- The transverse momentum of the track (P_T) is required to satisfy $P_T >$ 2.0 GeV/c. Daughter tracks of the highly-boosted B hadron from t decay are very likely to have P_T>2 GeV/c. Tracks from other sources are more likely to fail this requirement. Also, the CDF detector does not measure low momentum tracks as precisely as high momentum tracks, particularly in the impact parameter (d).

- At least two clusters on the SVX track must not be associated with any other track (these are called *shared* clusters) and must not contain any dead strips. The two good cluster requirement was determined by an extensive study of the tails of track-fit parameter distributions in a large sample of jets.

- The track's χ^2 per degree of freedom (χ^2_{dof}) is required to satisfy $\chi^2_{dof} < 6$. χ^2_{dof} is the track χ^2 divided by the number of SVX clusters associated with the track (see Section 2.3).

- The track's z coordinate is required to be consistent with the primary vertex, $|Z_0 - Z_v| < 5.0$ cm. This avoids tagging a second $p\bar{p}$ interaction due to the beam slope in x-y as a function of z.

- To remove very badly fit tracks, $K^0 \rightarrow \pi^+\pi^-$ decays, $\Lambda \rightarrow p\pi^-$ decays,

and other very long lived objects, large impact parameter tracks are ignored. Only tracks satisfying a $|d| < 0.15$ cm requirement are kept.

A jet is called a *taggable jet* if it has associated with it two or more tracks that pass this list of requirements. N_{SVX}, a per-jet variable, is the number of tracks that pass the listed requirements.

Tracks originating from a displaced secondary vertex tend to have a large impact parameter with respect to the primary vertex (see Figure 4.2). Tracks are called *displaced tracks* when they satisfy the requirement $|d|/\sigma_d > 3.0$. Figure 4.4 shows typical d/σ_d spectra for tracks in the generic jet sample (JET50) and for daughter tracks of B hadrons in ISAJET Monte Carlo generated events. The long tails in the d/σ_d distribution are due to long-lived B and charmed hadrons. Each tagged jet is required to have at least two displaced tracks. The two or more displaced tracks are fit using a 3-dimensional vertex constrained fitter, and individual track χ^2 contributions to the vertex χ^2 are calculated. Any track that contributes more than 50 to the vertex-fit χ^2 is removed from the vertex and the fit is repeated. Figure 4.5 shows the vertex-fit χ^2 before the χ^2 requirement has been applied. The χ^2 requirement is loose and designed to remove only true background.

Once the displaced tracks have been constrained to a common vertex, the displacement (L_{xy}) and the displacement uncertainty ($\sigma_{L_{xy}}$) are calculated. $L_{xy}>0$ fits are due mostly to true heavy flavor, and $L_{xy}<0$ fits are due mostly to tracking mistakes, resolution smearing, and a small component is due to true heavy flavor ($\sim$ 20%). The $L_{xy}<0$ fits due to tracking mistakes and resolution smearing typically have a large $\sigma_{L_{xy}}$ so they can be eliminated by a requirement on the quantity $|L_{xy}|/\sigma_{L_{xy}}$. Studies of top Monte Carlo and data samples (with small heavy flavor content) show the best requirement is

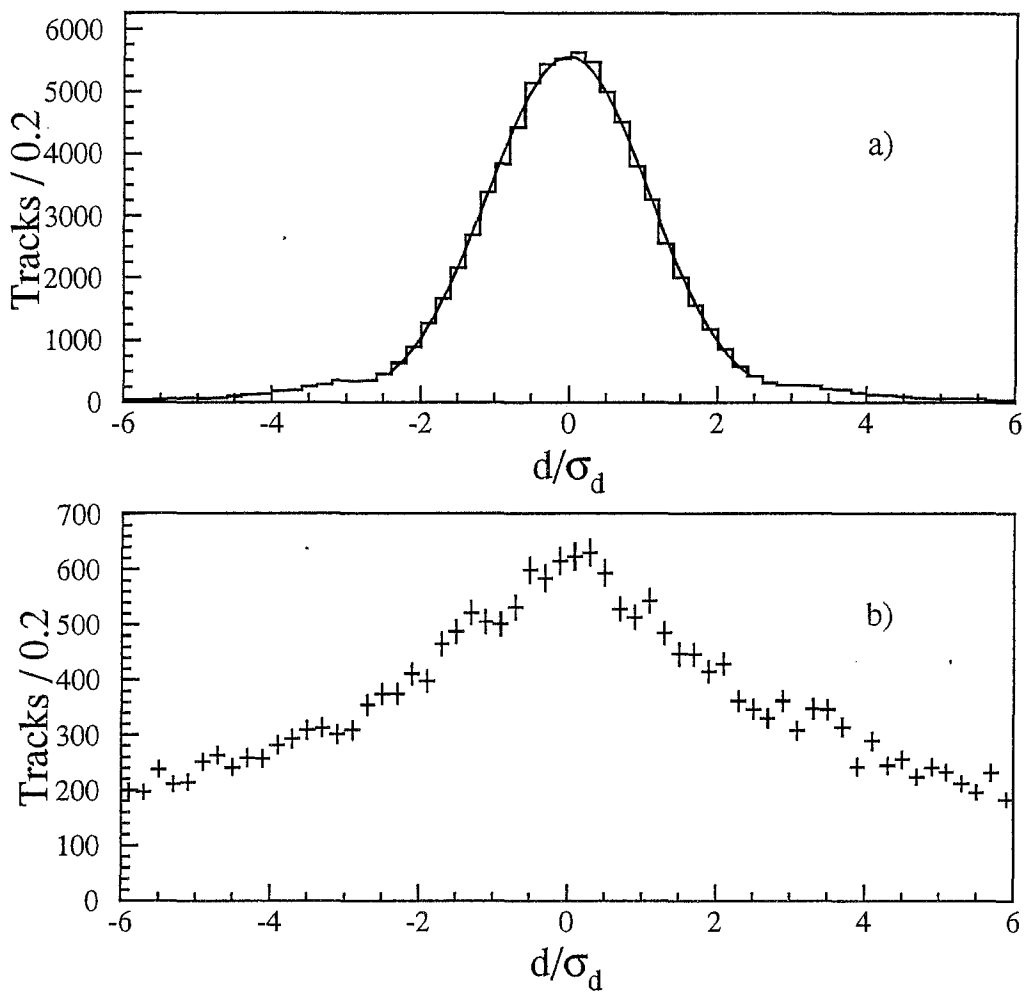

Figure 4.4: The impact parameter, d, distribution for tracks in (a) the JET50 sample, which is not expected to have a large heavy flavor content, and (b) in $t\bar{t}$ Monte Carlo generated events with M_{top}= 160 GeV/c^2. Only tracks from a B hadron decay are shown in the Monte Carlo simulation distribution.

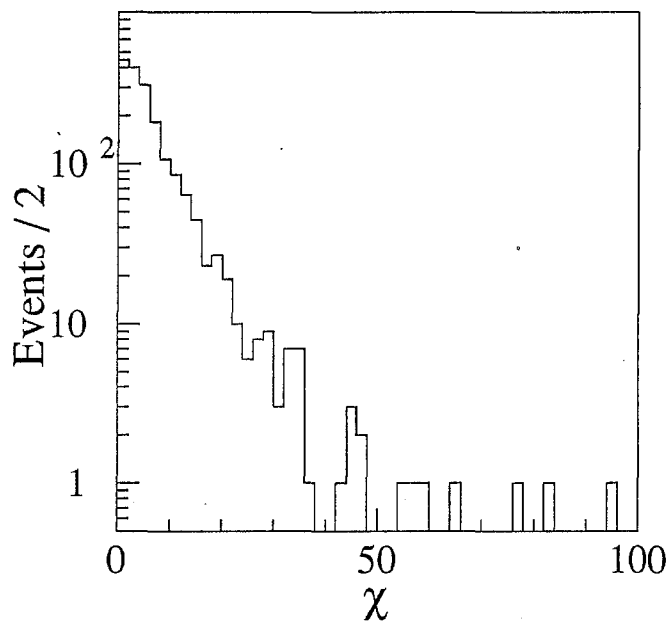

Figure 4.5: The vertex fit χ^2. All tracks that contribute more than 50 to the vertex χ^2 are removed from the fit. This histogram is made before the χ^2 requirement has been applied.

$|L_{xy}|/\sigma_{L_{xy}}$>3.0.

Found vertices passing the $|L_{xy}|/\sigma_{L_{xy}}$>3.0 requirement may be due to K_s mesons or Λ baryons, or other long lived hadrons. K_s and Λ hadrons are removed explicitly. Both K_s and Λ hadrons have two prong decays, and therefore fit vertices containing these hadrons will have two tracks in the vertex fit. Two track vertex fits are rejected if the invariant mass of the two tracks is in a window about the Λ or K_s hadron masses. A two track vertex fit is considered due to a $K_s \rightarrow \pi^+\pi^-$ decay if the invariant mass of the two tracks is in a ± 0.020 GeV/c^2 window about the K_s mass (0.49767 GeV/c^2). The invariant mass is calculated by assigning both tracks the π mass. $\Lambda \rightarrow p\pi^-$ decays are found the same way, except one track is assigned the π mass and the other the proton mass (both combinations are tried). Vertex fits with an invariant mass in a ± 0.015 GeV/c^2 mass window about the Λ mass (1.115 GeV/c^2) are rejected. Residual K_s, Λ, and conversion tags are estimated to be $(10 \pm 10)\%$ of the final tags by relaxing the mass window requirements and the γ conversion removal requirements and measuring the number of tags consistent with a K_s, Λ, or γ conversion decay.

Finally, it is possible to associate the same tracks with two different jets. Track sharing occurs because the jet cone size, $R = \sqrt{\delta\eta^2 + \delta\phi^2} = 0.4$, is larger than the track-jet association requirement, $cos(\theta) < 0.8$. The fit vertex is assigned to the jet whose x-y axis is closest to the x-y direction of the fit vertex. A jet with a fit vertex with $|L_{xy}|/\sigma_{L_{xy}} > 3$, that also passes the K_s and Λ mass requirements is called a *tagged* jet.

Tagged jets satisfying the condition $L_{xy}/\sigma_{L_{xy}} > 3.0$ are called positive decay length tags ($+L_{xy}$ tags). Similarly, tags with $L_{xy}/\sigma_{L_{xy}} < 3.0$ are called negative decay length tags ($-L_{xy}$ tags).

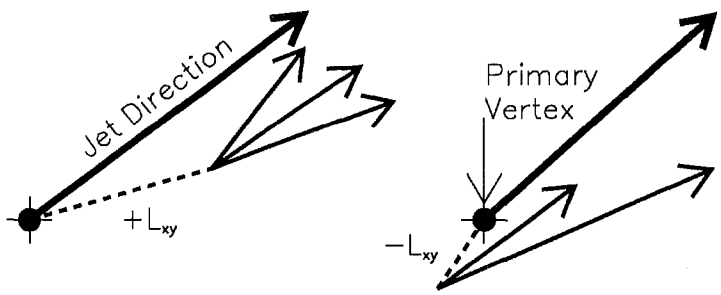

A negative tag is (to the first order) physically impossible; it means some particle has decayed behind the primary vertex. A small portion of negative tags are due to heavy flavor ($\sim 20\%$). A heavy flavor $-L_{xy}$ tag occurs when a track from the B hadron decay and a track from the cascade charmed hadron decay intersect behind the primary vertex. The dominant source of negative tags are due to tracking confusion and resolution smearing.

The b-tagging algorithm's efficiency is primarily a function of the distance the B hadron travels in the lab frame and the impact parameters of the B hadron's daughter tracks. The two effects compete against each other. The further the B travels, the larger a daughter track's impact parameter will be. However, jets from higher-P_T B hadrons are more collimated because the particles in the jet experience more of a boost, and thus the impact parameters of tracks are smaller. Figure 4.2, the $t\bar{t}$ decay cartoon, shows this effectively. The two effects balance when the B hadron is relativistic. Figure 4.6 shows the b-tagging efficiency for B quarks from a $t\bar{t}$ decay as a function of jet E_T. The low efficiency at low E_T is caused by the small boost of the B hadron. The B hadron decays before it is sufficiently far away from the primary vertex to be resolved by the SVX detector.

One of the B hadron's daughters is almost always a charmed hadron, which is also long lived ($c\tau \simeq 120$ μm for the D^0, ~ 300 μm for the $D^{\pm}$, about 1/3 the B hadron's lifetime)[19]. It will travel from the B hadron's decay vertex to

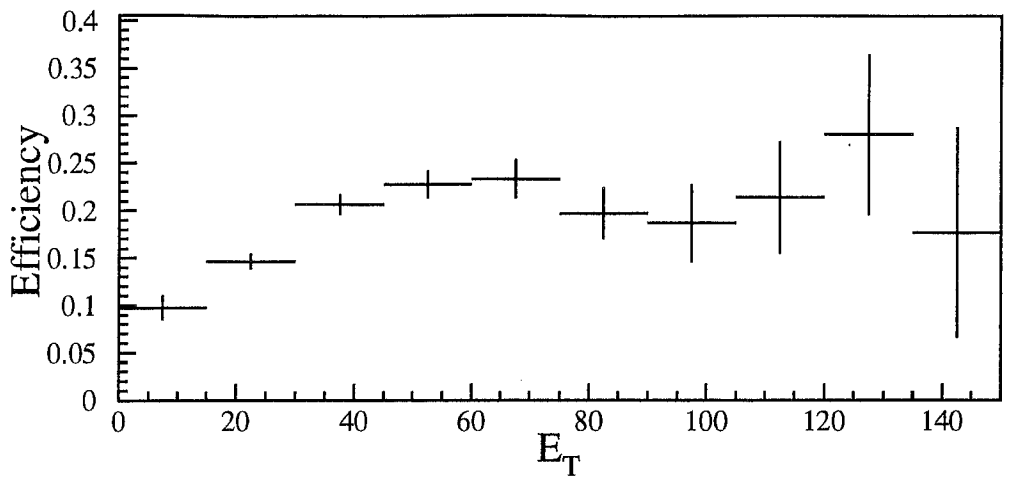

Figure 4.6: The JETVTX b-tagging efficiency in $t\bar{t}$ M_{top}=160 GeV/c^2 Monte Carlo simulated events as a function of the b-quark jet E_T.

	% of Total Tags
B hadron tracks only	20%
Charmed hadron tracks only	30%
Combination	50%

Table 4.1: The composition of the tags in $t\bar{t}$ Monte Carlo generated events. All numbers have an error of 10% associated with them due to statistics.

form a tertiary vertex. JETVTX will also tag tracks from this vertex because of the loose vertex χ^2 requirement. Table 4.1 shows the composition of tags in a $t\bar{t}$ ISAJET Monte Carlo simulation. About 50% of the time the displaced tracks in a tagged b jet consist of a mixture of tracks directly from the B and from the charmed hadron.

The b-tag algorithm is optimized by choosing the best values for the d/σ_d and P_T requirements. A large data sample, the JET50 sample, is used to measure the background tagging rate, and the $t\bar{t}$ Monte Carlo simulation is used to measure the signal rate. The P_T and d/σ_d requirements are varied

until the best value of signal squared (events tagged in $t\bar{t}$ Monte Carlo event sample) over background (number of tagged JET50 events) is found. The requirements P_T>2 GeV/c and $|L_{xy}|/\sigma_{L_{xy}}>$ 3.0 maximize the signal-squared to background ratio.

4.1.1 The $c\tau$ of the JETVTX Tags

The lifetime of a B hadron can be calculated from the 2-dimensional decay length, L_{xy}. The conversion from L_{xy} to $c\tau$ isn't straightforward for several reasons: distance the B hadron travels in z is not known accurately, the CDF detector isn't 100% efficient at finding all tracks, and tracks with P_T below $\sim$ 400 MeV are not reconstructed. Instead of calculating $c\tau$ directly, it is estimated. The effective decay length, $c\tau_{eff}$, is defined as:

$$c\tau_{eff} = L_{xy}\frac{M}{P_T F},$$

where M is the invariant mass of the tracks in the secondary vertex, P_T is the track's total vector transverse momentum, and F is a scale factor determined in a B hadron Monte Carlo simulation generated by the HERWIG program. The B hadron lifetime is set to the world average, $c\tau = 453$ μm. The scale factor, F, accounts for the tracks not associated with the secondary vertex as well as the fact that L_{xy} is a missing the z information. Above a B hadron P_T of 15 GeV/c, F is constant, and has a value of 0.7, below 15 GeV/c it rises slowly, changing by 10% of itself.

Figure 4.7 shows the $c\tau_{eff}$ of tags in the ICE sample (points). This sample has a high b-quark content (F_b=(37$\pm$8)%). The histogram is the $c\tau_{eff}$ of tags found in $b\bar{b}$ Monte Carlo generated events. This gives evidence that JETVTX is indeed tagging B hadrons. There are tags due to charm hadrons in the ICE

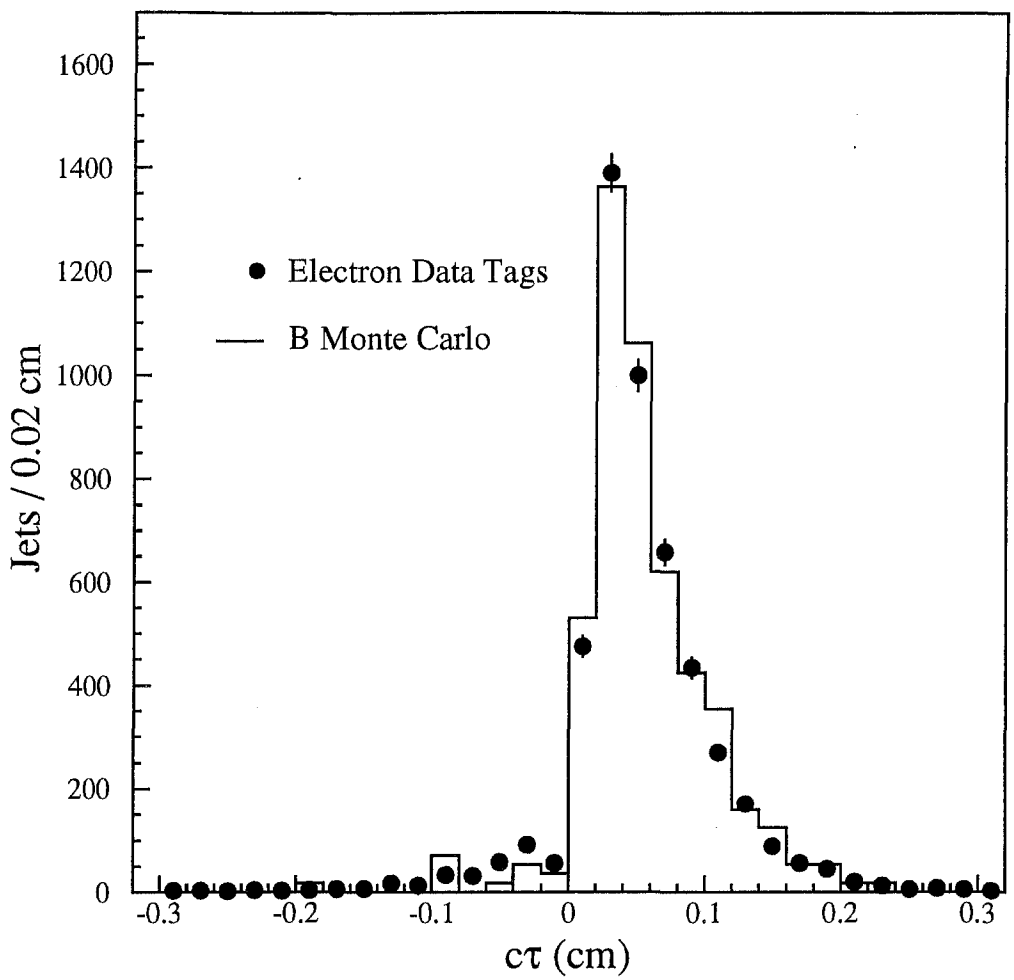

Figure 4.7: $c\tau_{eff}$ of tags in the Inclusive Central Electron (ICE) sample.

sample, but the contribution to the total number of tags is small because the charmed-hadron tagging efficiency is small compared to a B hadron's tagging efficiency, mostly due to the charmed hadron's short lifetime ($\sim$ 5% tagging efficiency, as compared to $\sim$ 30% for B hadrons). The tagging efficiency is examined in detail in the next section.

4.2 The b-tagging Efficiency

The b-jet tagging efficiency is an important part of the top acceptance calculation. The efficiency of the b-tagging algorithm is determined using the ICE data sample. Two methods are used for determining the tagging efficiency, and the results are averaged. The first method, called the singles efficiency, is based on tags of the electron jet that triggered the event. It is defined as:

$$\epsilon_{singles} = \frac{N^{with}}{N \times F_b},$$

where N^{with} is the number of tagged primary electron jets, N is the total number of good taggable electron jets in the sample, and F_b is the sample's b-fraction as determined in Section 3.2. Only taggable jets (as defined in Section 4.1) are counted so that $\epsilon_{singles}$ is insensitive to the taggable jet production rate.

The second efficiency, called the doubles efficiency, is based on double-tagged events, with one tag in the primary-electron jet and a second tag in another jet. It is the efficiency at which the primary-electron jets are tagged in a sample of events with a non-electron jet tag. The efficiency is defined as

$$\epsilon_{doubles} = \frac{N^{double}}{N^{away}},$$

where N^{away} is the number of events with a tag in a jet other than the primary-electron jet, and N^{double} is the number of events with both the primary electron jet and one additional jet tagged.

The quantities N^{away} and N^{with} must be background subtracted to account for mistags in the ICE data sample. Section 5.1 describes the procedure in detail, and it is outlined briefly here. A sample known to have small heavy

flavor content, the generic jet sample (the JET50 sample), is used to calculate a tag rate per jet. The tags in the JET50 sample include tags from $g \rightarrow b\bar{b}$, direct $b\bar{b}$ production, and $b\bar{b}$ from flavor excitation. These are all sources that will be present in other data samples, like the ICE sample, at approximately the same rate as in the JET50 sample. The background subtraction accounts for this base rate that underlies any excess heavy flavor, or signal. The JET50 tag rate is called the *mistag rate* when it is applied to other samples. The mistag rate, averaged over the whole JET50 sample, is $\sim 1\%$. The mistag rate is parameterized by the jet E_T and the number of good quality SVX tracks associated with the jet. Each bin of the resulting *tag matrix* contains the expected contribution for jets in a 10 GeV E_T range and a particular number of good SVX tracks. The number of background tags in the ICE sample is determined by a tag-matrix weighted sum over each jet in the ICE sample. N^{with} and N^{away} are both corrected as follows:

$$N^{with} = N^{with}_{raw} - (1 - F_b) * N^{with}_{mistag}$$

and

$$N^{away} = N^{away}_{raw} - (1 - F_b) * N^{away}_{mistag},$$

where the "$_{raw}$" subscript refers to the actual number of tags observed in the sample, and the "$_{mistag}$" subscript refers to the number of tags predicted using the tag matrix. This method assumes that each jet in the sample has the same heavy flavor content as the JET50 sample. This is an over-correction in the ICE data sample, which has a non-negligible B hadron content (F_b). Multiplying the tag prediction by the factor $(1 - F_b)$ scales the estimate by the number of expected non-b-quark jets. N^{double} is not corrected for mistags

	Inclusive Electrons	ISAJET $b\bar{b}$
Good Taggable Electrons	43114	1717
Tagged Electron Jets	4911	650
Tagged Away Jets	451	117
Double Tagged Events	106	49
Predicted Mistag Electron Jet Tags	358.1	N/A
Predicted Mistag Away Jet Tags	106.1	N/A
Corrected Electron Jet Tags	4552.9	650
Corrected Away Jet Tags	344.9	117
Single Tagging Rate ($\epsilon_{singles}$)	28.85 ± 5.8	37.86 ± 1.2
Double Tagging Rate ($\epsilon_{doublets}$)	30.73 ± 2.5	41.88 ± 4.6

Table 4.2: Tagging results in the ICE sample and ISAJET $b\bar{b}$ Monte Carlo generated events. The predictions are used for background subtraction.

because the double tag rate is very small: the chance of two fake tags happening in the same event is on the order of $1\% \times 1\% = 0.01\%$, much smaller than the systematic uncertainties in the calculation.

Table 4.2 tabulates the results in the ICE sample. The efficiencies are

$$\epsilon^{data}_{singles} = 28.8 \pm 5.8\%$$

and

$$\epsilon^{data}_{doubles} = 30.7 \pm 2.5\%.$$

$\epsilon^{data}_{singles}$ has very high statistics, but is limited by the large uncertainty in F_b. $\epsilon^{data}_{doubles}$ is not limited by the uncertainties in F_b, as F_b only enters as a second-order effect, but the $R_{doubles}$ method does suffer from poor statistics.

Table 4.2 also shows the tags and the tag rates in the ISAJET $b\bar{b}$ Monte Carlo simulation. In the Monte Carlo simulation there is no need for background corrections as there are no non-$b\bar{b}$ events (F_b is 1.0 by definition). The single and double tagging rates in Monte Carlo generated events are calculated

accordingly, and found to be

$$\epsilon^{MC}_{singles} = 37.86 \pm 1.2\%$$

and

$$\epsilon^{MC}_{doubles} = 41.88 \pm 4.6\%.$$

4.2.1 The Data/Monte Carlo Scale Factor

The tagging rates measured in the Monte Carlo simulation are 30% higher than those measured in the data. This difference must be taken into account when the tagging algorithm is used on the Monte Carlo simulation (i.e. when calculating the number of expected tags from $t\bar{t}$ events). The data/Monte Carlo scale factor is defined as

$$F^{tag}_{scale} = \frac{\epsilon^{Data}_{av}}{\epsilon^{Monte\ Carlo}_{av}},$$

where ϵ^{Data}_{av} and $\epsilon^{Monte\ Carlo}_{av}$ are the error weighted averages of $\epsilon_{singles}$ and $\epsilon_{doubles}$. Then, $F^{tag}_{scale} = 0.75 \pm 0.12$.

F^{tag}_{scale} is the data/Monte Carlo scale factor for taggable jets only, because the tag efficiencies, ϵ, use taggable jets as their denominators. The other half of the scale factor, $F^{taggable}_{scale}$, scales the taggable jet production rate in the Monte Carlo simulation to the rate observed in data. Because the primary use of this scale factor is in the $t\bar{t}$ acceptance calculation, where the scale factor will be applied to a $t\bar{t}$ Monte Carlo simulation, we use the W+jet data sample and the $t\bar{t}$ ISAJET Monte Carlo simulation to calculate $F^{taggable}_{scale}$. Table 4.3 details the results of $F^{taggable}_{scale}$, found in the W+ jets data sample and ISAJET $t\bar{t}$ Monte Carlo simulation. The taggable jet scale factor is $F^{taggable}_{scale} = 0.96 \pm 0.02$, and

	$W+$ jets	M_{top}= 160 GeV/c^2
Number of Jets	1849	8132
Number of Taggable Jets	930	4270
Taggable Rate	$.503 \pm 0.016$	$.525 \pm 0.0055$

Table 4.3: The raw numbers used to calculate $F_{scale}^{taggable}$.

the scale factor (F_{scale}) is the two multiplied together:

$$F_{scale} = F_{scale}^{tag} \times F_{scale}^{taggable} = 0.72 \pm 0.21.$$

The systematic uncertainty assigned to the scale factor is due to the different E_T spectra of the b-jets from $t\bar{t}$ decay and b-jets in the ICE sample, the limited statistics in the calculation of $\epsilon_{doubles}$, and the uncertainty in F_b. Figure 4.8 shows the E_T spectra of both the W+jets and the ICE sample normalized to equal area. The scale factor as a function of E_T is shown in Figure 4.9. F_{scale}^{tag} is based on the high statistics ICE sample, which is made up mostly of low E_T electron jets, as compared to the W+jet sample, which has a much flatter distribution in jet E_T. A large part of the scale factor's systematic uncertainty, ± 0.17 (23%), is due to the reduced ICE data sample statistics at high electron jet energies. The uncertainty ± 0.17 is the result of fitting the scale factor to a straight line as a function of E_T, taking a $\pm 1\sigma$ variation in the fitted slope, weighting it by the E_T spectrum of b-quark jets from $t\bar{t}$ Monte Carlo generated events, and comparing the resulting E_T averaged scale factor to the calculated F_{scale} above.

The SVX tracking efficiency and impact parameter resolution are better in Monte Carlo than in data. However, these differences can account for only 1/3

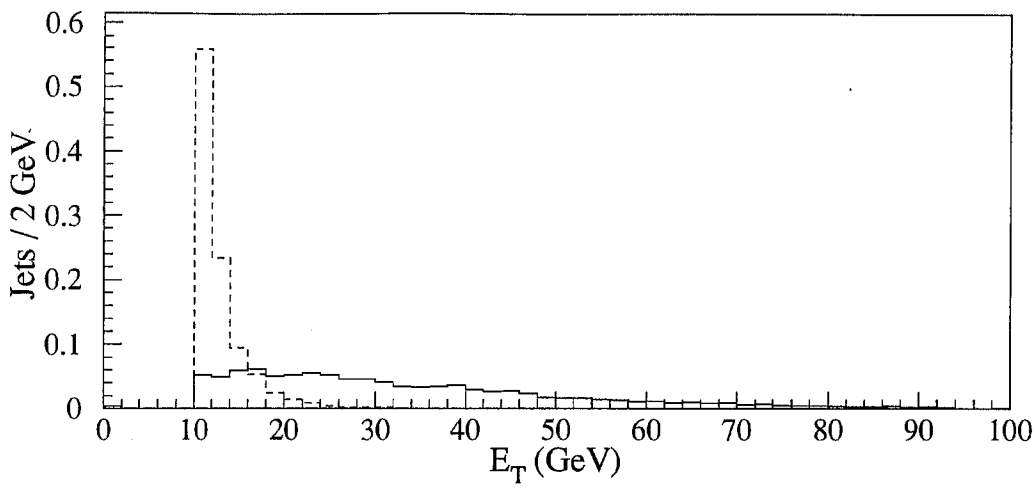

Figure 4.8: The E_T of jets in the $t\bar{t}$ ISAJET Monte Carlo simulation (solid histogram) and in ICE data sample (dashed histogram).

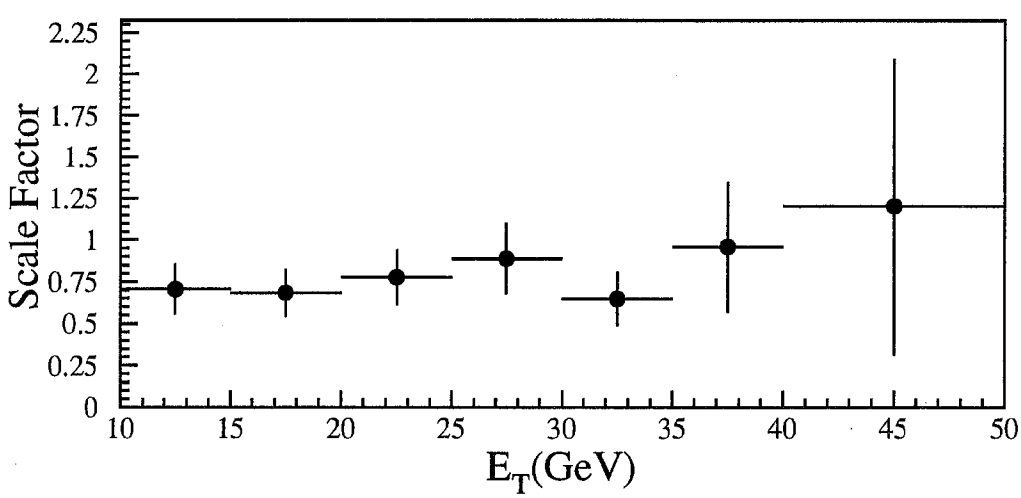

Figure 4.9: The scale factor F_{scale}^{tag} as a function of jet E_T. The systematic uncertainty on F_{scale}^{tag} is calculated by doing a straight-line fit to the data in this plot, and evaluating it at the average jet E_T for jets in $t\bar{t}$ Monte Carlo generated events.

of the difference in tagging rates between data and Monte Carlo simulation. The lower than expected b-tagging efficiency does not affect the significance of the tagging result, though it does affect the calculated cross section.

4.3 The $t\bar{t}$ Acceptance

The acceptance for the $t\bar{t}$ signal can be written as

$$\epsilon_{top} = Br(t\bar{t} \rightarrow \ell X) \cdot \epsilon_{P_T>20} \cdot \epsilon_{lep} \cdot \epsilon_{\not{E}_T} \cdot \epsilon_{Jet} \cdot \epsilon_{tag},$$

where $\epsilon_{P_T>20}$ is the fraction of $t\bar{t}$ events with a high-P_T lepton, $Br(t\bar{t} \rightarrow \ell X)$ is the branching ratio for $t\bar{t}$ events to give at least one lepton with $P_T >$ 20GeV/c, ϵ_{lep} is the lepton identification efficiency, $\epsilon_{\not{E}_T}$ is the fraction of $t\bar{t}$ events with 20 GeV or more of missing energy, ϵ_{Jet} is the fraction of $t\bar{t}$ events with 3 or more central jets with $E_T >$ 15 GeV, and ϵ_{tag} is the b-tagging efficency.

A Monte Carlo simulation is used to determine each of the efficiencies:

- $\epsilon_{P_T>20}$ is the number of found high-P_T leptons divided by the number of $t\bar{t}$ events generated by the Monte Carlo simulation.
- ϵ_{lep} is the number of events with at least one good high-P_T lepton divided by the number of produced leptons.
- $\epsilon_{\not{E}_T}$ is the fraction of events with a good high-P_T lepton passing the $\not{E}_T$ $>$ 20 GeV requirement.
- ϵ_{Jet} is the fraction of events with a good lepton and $\not{E}_T > 20$ GeV that also contain three or more centrally located $E_T >$ 15 GeV jets.

Figure 4.10 shows the expected top yield for two top masses, 120 GeV/c^2 and 180 GeV/c^2 as well as the observed number of events in the data, binned

M_{top} (GeV/c2)	120	160	180
$\sigma(t\bar{t})$ (pb) (theory)	$38.9 \pm^{10.8}_{5.2}$	$8.2 \pm^{1.4}_{0.8}$	$4.2 \pm^{0.6}_{0.4}$
$\epsilon_{top}/\epsilon_{tag}$	0.051 ± 0.007	0.077 ± 0.008	0.081 ± 0.008
Expected Events	39 ± 6	12 ± 2	6.6 ± 0.7

Table 4.4: The acceptance and expected event yield of $t\bar{t}$ events for M_{top} of 120, 160, and 180 GeV/c^2 in 19.3 pb^{-1} of data.

by event jet multiplicity. The secondary-vertex algorithm and efficiency has not been applied to the data in this distribution.

Table 4.4 lists the results of the quotient $\epsilon_{top}/\epsilon_{tag}$ calculation for three top masses, expected event yields when at least three jets are required, and the calculated $t\bar{t}$ production cross section from Reference [1].

The efficiency for tagging a b-jet, ϵ_{tag}, is written as

$$\epsilon_{tag} = \epsilon_{SVX} \times F_{scale} \times \frac{N_{tagged}}{N_{jets}},$$

where ϵ_{SVX} is the percentage of b-jets from $t\bar{t}$ decays that are within the SVX acceptance, N_{tagged} is the number of b-jets tagged, and N_{jets} is the total number of jets (within the SVX fiducial volume). ϵ_{tag} and the predicted number of events are shown in Table 4.5.

4.4 The Tags in the $W+\geq 3$ jet Sample

Six events are tagged by the JETXTX tagging algorithm in the $W+\geq 3$ jet data sample. Table 4.6 summarizes each of the six tagged events. Figure 4.11 is an event display of event 123158, run 45879, a 4 jet high-P_T muon event. Figure 4.12 shows the $c\tau_{eff}$ in the W+jet data sample (points) and the expected $c\tau_{eff}$ shape from a $t\bar{t}$ Monte Carlo simulation.

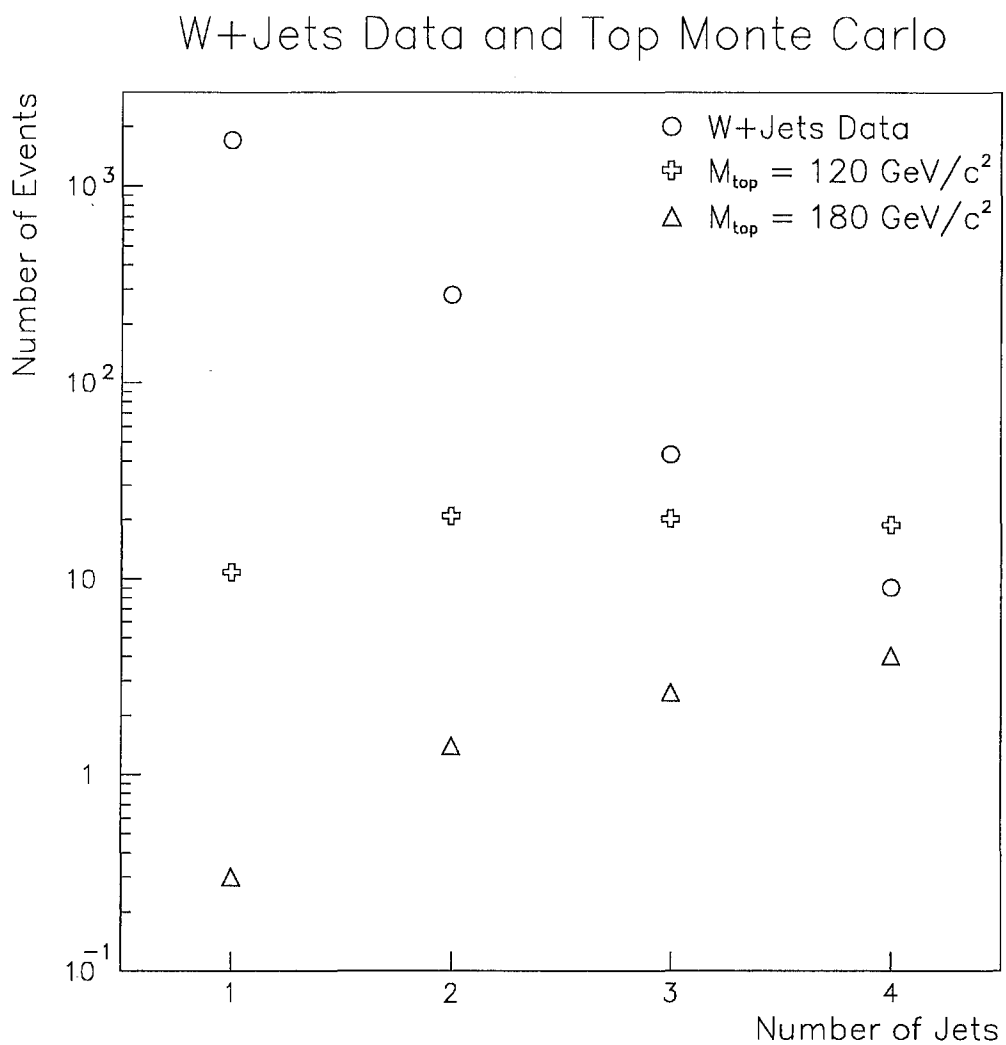

Figure 4.10: The number of expected $t\bar{t}$ events and number of observed W observed as a function of the jet multiplicity. Note that for ≥ 3 jets, the top signal is still overwhelmed by the W+jet rate. This is why a b-tag is required.

M_{top}GeV/c^2	ϵ_{tag}	Expected Events
120	0.20 ± 0.05	7.7 ± 2.5
140	0.22 ± 0.06	4.8 ± 1.7
160	0.22 ± 0.06	2.7 ± 0.9
180	0.22 ± 0.06	1.4 ± 0.4

Table 4.5: The expected number of tagged events and ϵ_{tag} for various top masses.

Run 40758, Event 44404

Object	Tag	η	ϕ (rad)	E_T (GeV)
e^+		0.44	3.63	109.0
$\not{E}_T$			4.69	56.2
Jet 1	$\surd$	-0.24	0.30	74.0
Jet 2		0.30	1.91	64.1
Jet 3		0.62	0.80	51.9
Jet 4		1.46	5.66	20.2

Run 42517, Event 44047

Object	Tag	η	ϕ (rad)	E_T (GeV)
μ^+		0.86	5.72	49.7
$\not{E}_T$			1.33	60.2
Jet 1		0.49	3.12	26.0
Jet 2		0.15	3.83	21.9
Jet 3	$\surd$	-0.67	4.34	18.2

Run 43096, Event 47223

Object	Tag	η	ϕ (rad)	E_T (GeV)
e^-		-0.81	0.77	33.1
$\not{E}_T$			4.55	72.0
Jet 1	$\surd$	0.02	0.91	101.4
Jet 2		1.35	2.74	57.2
Jet 3		1.02	4.87	47.4
Jet 4		2.02	3.53	26.5

Run 45047, Event 104393

Object	Tag	η	ϕ (rad)	E_T (GeV)
μ^-		-0.36	2.03	39.4
$\not{E}_T$			5.52	91.0
Jet 1	$\surd$	-1.20	2.06	43.9
Jet 2		0.41	4.45	30.2
Jet 3		0.91	2.05	22.5

Run 45610, Event 139064

Object	Tag	η	ϕ (rad)	E_T (GeV)
μ^-		-0.18	0.21	54.3
$\not{E}_T$			2.53	27.7
Jet 1	$\surd$	-0.70	1.42	58.9
Jet 2		-0.90	45.2	50.9
Jet 3		1.51	4.80	27.0
Jet 4		0.07	3.58	10.8

Run 45879, Event 123158

Object	Tag	η	ϕ (rad)	E_T (GeV)
μ^+		-0.21	0.09	53.7
$\not{E}_T$			3.34	28.0
Jet 1		-1.63	2.79	69.4
Jet 2	$\surd$	-0.11	5.21	61.2
Jet 3		0.13	0.66	28.8
Jet 4		-0.44	3.26	25.9

Table 4.6: Details of the six JETVTX tagged events in the $W+\geq 3$ jet signal sample. A $\surd$ indicates the jet tagged by JETVTX.

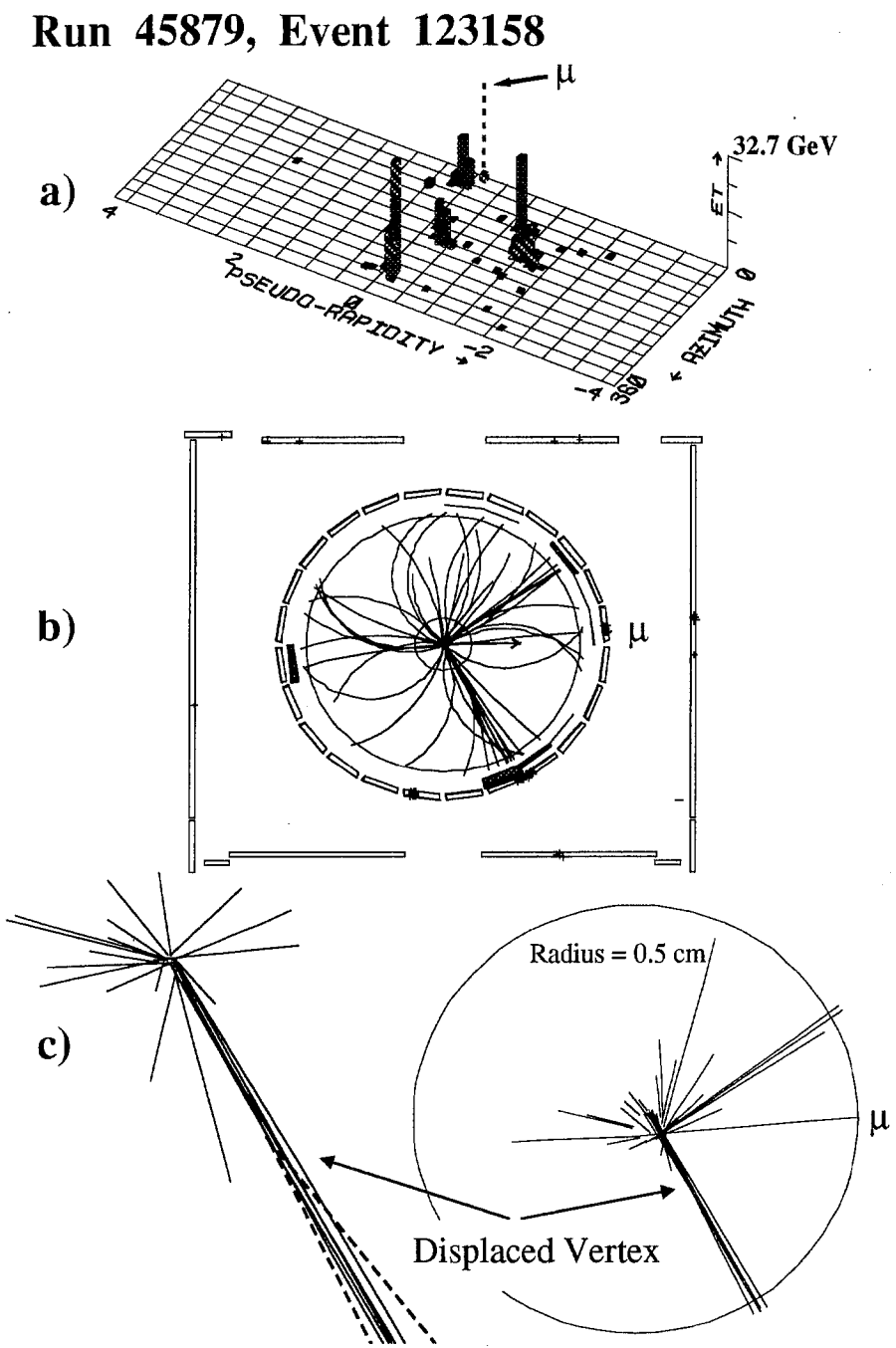

Figure 4.11: Event display for one of the SVX tagged W+jet events; (a) displays the observed calorimeter E_T in the $\eta - \phi$ plane, (b) shows muon hits in the CMP detector (circular detector just outside the tracking chamber) and CMU detector muon hits (the square detector outside the CMP) as well as the charged tracks found by the CTC. Details of tracks found by the SVX as well as the complete SVX event display are shown in (c). The dashed tracks form the displaced vertex (extraneous tracks have been removed from the enlargement). Track lengths of in the SVX display are proportional to the track's P_T.

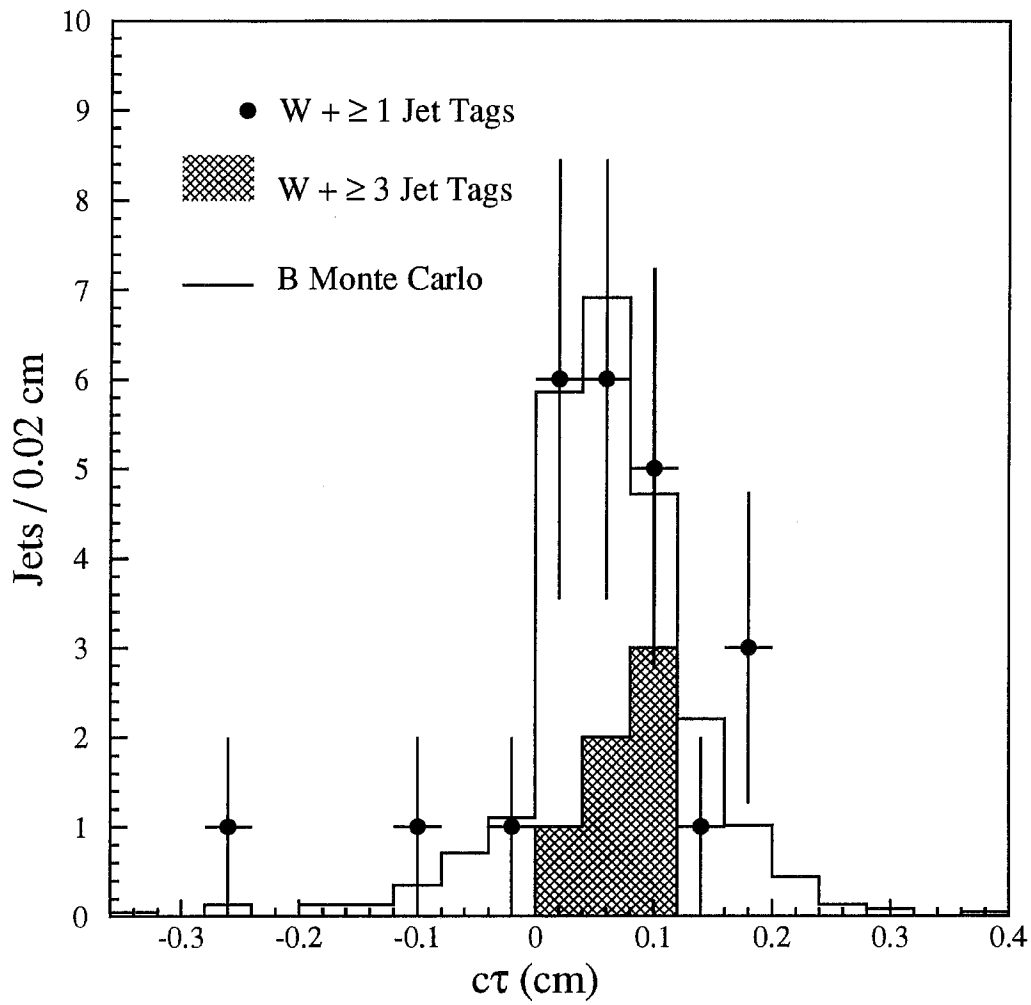

Figure 4.12: The $c\tau_{eff}$ distribution for jets with a secondary-vertex tag in the W+jets data sample (points) compared to b-quark tags from a Monte Carlo simulation (histogram, normalized to data). The shaded histogram represents the tags in the $W+\geq 3$ jet sample. Two tags, with $c\tau_{eff} = 1.2$ cm and -0.41 cm are not shown. They are a W+2 and a $W+1$ jet event, respectively.

Chapter 5

The Background Calculation

It is important to answer the question "How many b-tags do we expect in the $W+\geq 3$ jet sample if there are no $t\bar{t}$ events present?" The number of these tags, called *background tags*, must be accurately quantified to understand the significance of the six observed tags. The background tags can be understood as coming from four sources. First, tags can come from detector resolution and tracking reconstruction errors (called *mistags*). The second source of background tags are gluon jets splitting to a heavy flavor quark pair in a W+jet event (the so called $Wb\bar{b}$ or $Wc\bar{c}$ events)[13]. Third, there are other sources of long lived particles and heavy flavor in W events, like Wc production, $Z \rightarrow \tau\tau$ decays, and diboson production (WW and WZ) in which one of the bosons decays to a τ lepton or heavy flavor. Finally, the fourth source of background tags in the $W+\geq 3$ jet sample is non-W contamination, which includes direct $b\bar{b}$ production.

The rest of this chapter describes the background estimates for each of the four sources of tags. The basic method for predicting tags due to detector effects, $Wb\bar{b}$, and $Wc\bar{c}$ is described first, in Section 5.1. A large data sample is used to determine the rate of background tags, and a Monte Carlo calculation is

performed to check the results. Section 5.2 describes the tagging contribution due to the other sources of backgrounds, and finally, Section 5.3 summarizes the background tags expected from each source.

5.1 Mistags, $Wb\bar{b}$, and $Wc\bar{c}$ Backgrounds

Background tags caused by resolution smearing, detector effects, and gluon splitting to heavy flavor are estimated to be approximately 85% of the total expected background tags. We use a large, high statistics data sample to predict the tags due to detector effects and gluon splitting in the $W+ \geq 3$ jet sample, and a Monte Carlo calculation to check the prediction. The data method is the preferred method of background calculation as there is evidence the Monte Carlo simulations do not take into account all of the idiosyncrasies of the data (i.e., $F_{scale} \neq 1$). Also, the background estimate using the data method is larger than the Monte Carlo prediction and, thus, is a more conservative choice when calculating the statistical significance of the six observed events.

The motivation for using a large statistics data sample to predict the number of background tags in the W+jet sample is discussed first. Next, the procedure is described. We parameterize the tag rate of a large data sample and use that parameterized tag rate to predict the number of background tags in the $W+ \geq 3$ jet sample. Next, we describe the systematic error determination for the background tag prediction. Further studies are also performed to understand how robust the prediction is under changes in the way the tag rate is parameterized. Finally, a Monte Carlo calculation is used to predict the number of background tags due to $Wb\bar{b}$ and $Wc\bar{c}$. The results of the Monte Carlo calculation are compared to the results obtained using the parameterized

tag rate.

5.1.1 The Procedure

As mentioned above, we use a high statistics data sample whose heavy flavor content is similar to, or more than that of the $W+\geq 3$ jet sample to determine the tag rate. The tag rate in the large data sample is used to predict an upper bound on the number of tags in the $W+\geq 3$ jet sample due to gluon splitting and detector effects.

The generic jet data sample (JET50) provides ample statistics to determine a tag rate with small statistical uncertainties, and it is not enhanced in heavy flavor as the ICE sample is. Table 5.1 lists the results of running JETVTX on the JET50 data sample. The small (2%) $+L_{xy}$ tag rate is evidence of the small heavy flavor content. The $c\tau_{eff}$ of the JET50, shown in Figure 5.1, is further evidence (when compared with the $+L_{xy}$ to $-L_{xy}$ ratio in the ICE sample). As in the $c\tau_{eff}$ distribution for the ICE sample, the points are the observed tags in the JET50 sample, and the histogram is a fit of Monte Carlo generated events to the data. The histogram is a sum of three Monte Carlo simulations: a $b\bar{b}$ Monte Carlo simulation, a $c\bar{c}$ Monte Carlo simulation, and a Monte Carlo simulation with no long lived particles. The contribution of each is adjusted to give the best fit to the $c\tau_{eff}$ shape in the data. The shaded area, about 75% of the area of the distribution, is the combination of the $b\bar{b}$ and $c\bar{c}$ Monte Carlo simulations. Note the $-L_{xy}$ tags are a much larger proportion of the total number of tags than in the ICE sample. The negative tags depend mostly on the topology of the jets, not on their heavy flavor content, so the $-L_{xy}$ tag rate is similar from sample to sample. The positive tag rate, however, depends almost exclusively upon the heavy flavor content of the jets.

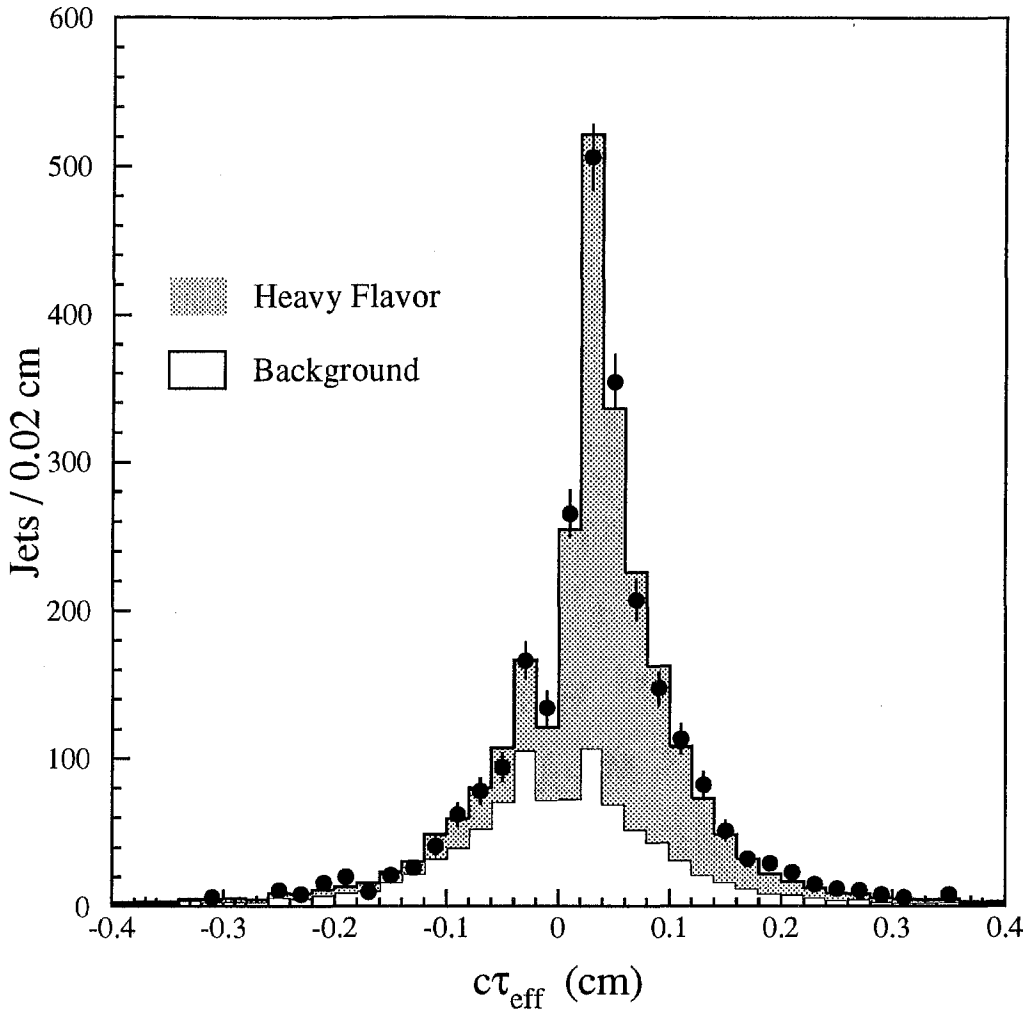

Figure 5.1: The $c\tau_{eff}$ of the JET50 sample. The JET50 sample does have an appreciable heavy flavor content, though small compared to the ICE sample. The points are the observed tags. The histogram is the sum of $c\bar{c}$, $b\bar{b}$, and background Monte Carlo simulations. The background Monte Carlo generated events contain no long lived particles. The shaded area, $b\bar{b}$ and $c\bar{c}$ contributions, is about 75% of the area under the histogram. Note the $c\tau_{eff}$ distribution of the background Monte Carlo generated tags is symmetric about zero.

	Events
Taggable Jets, $E_T >$ 10 GeV	123660
$+L_{xy}$ Tags	1744
$-L_{xy}$ Tags	661

Table 5.1: Tags in the JET50 sample. The 15 GeV jet requirement matches the 15 GeV jet requirement in the W signal sample by design.

Heavy flavor in a QCD $W \rightarrow \ell\bar{\nu}$ event arises when a gluon jet splits into a $b\bar{b}$ or a $c\bar{c}$ quark pair (one possible Feynman diagram is shown in Figure 1.6)[13]. The JET50 sample, however, has three sources of heavy flavor: direct production ($p\bar{p} \rightarrow b\bar{b}$), gluon splitting (same as in the W sample), and flavor excitation. The Feynman diagrams for the three production mechanisms are shown in Figure 5.2.

The HERWIG Monte Carlo program predicts that the gluon splitting process accounts for 65% of produced $b\bar{b}$ pairs, and 75% of produced $c\bar{c}$ pairs in the JET50 sample[22]. VECBOS and HERWIG Monte Carlo calculations predict that the fraction of gluon jets in the W+jet sample is 1.5 to 2 times smaller than in the JET50 sample for jet multiplicities between 1 and 4. A HERWIG Monte Carlo calculation predicts the b-quark content per jet to be almost three times smaller in the W+jet sample than in the JET50 sample when all heavy flavor contributions are included in the calculation.

It is, then, evident that a background prediction based on the JET50 tag rate, in the $W+\geq 3$ jet sample, should be an overestimate, thus conservative.

A naive scaling of the tag rate from the JET50 sample into the $W+\geq 3$ jet sample would have prohibitive systematic uncertainties because there are known correlations between the tag rate and two jet quantities: the jet E_T and N_{SVX}. Figure 5.3 shows the $+L_{xy}$ and $-L_{xy}$ tag rates as a function of

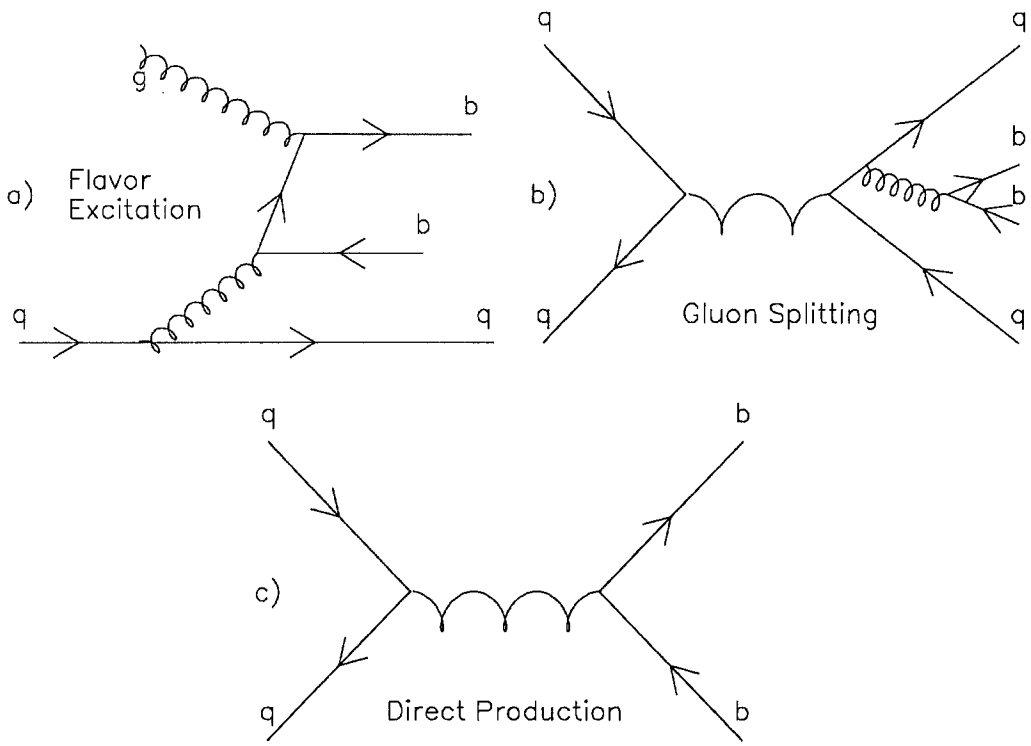

Figure 5.2: The three Feynman diagrams for heavy flavor production in the JET50 data sample, (a) flavor excitation, (b) gluon splitting, and (c) direct $b\bar{b}$ production.

jet E_T and the number of good quality SVX tracks (N_{SVX}). The tagging rate, as a function of jet E_T, is flat above 30 GeV, with a quick turn on below that threshold. The $W+ \geq 3$ jet sample has jets with transverse energies down to 15 GeV. Below 30 GeV, B hadrons do not travel far enough from the primary vertex to be easily resolvable by the SVX detector. The tagging rate also rises as N_{SVX} increases. N_{SVX} is a measure of the complexity of the tracking environment: the track reconstruction software is more likely to choose the wrong hit or cluster in a dense track environment. As such, almost any quantity that measures the density of tracks or hits in the tracking chambers could have been used in place of N_{SVX}.

The correlations between tag rate and jet E_T and N_{SVX} are important because the jet E_T and N_{SVX} distributions are different in the JET50 and W+jet data samples. To remove these two correlations when we apply the JET50 tag rate to the $W+ \geq 3$ jet sample, we parameterize the tag rate by jet E_T (range 10 to 200 GeV in 10 GeV steps) and by N_{SVX} (2 to 14 tracks in 1 track steps). The taggable and tagged jets in the JET50 data sample are counted in each jet E_T and N_{SVX} bin. Any bin with a tagging rate that has more than a 30% statistical uncertainty is combined with adjacent bins to prevent gross statistical uncertainties in the final background prediction. The tag rate lookup table is called the *standard tag matrix.*

Predicting expected tags in other samples is straightforward once the tag matrix has been constructed. The calculation of the background proceeds on a jet-by-jet basis. The tag matrix is used to assign a tag probability to each jet. The weights assigned to each jet by the tag matrix in an event are summed, and the background prediction for the sample is the sum over each event. The resulting total is the predicted number of tags due to detector effects, $Wb\bar{b}$, and $Wc\bar{c}$.

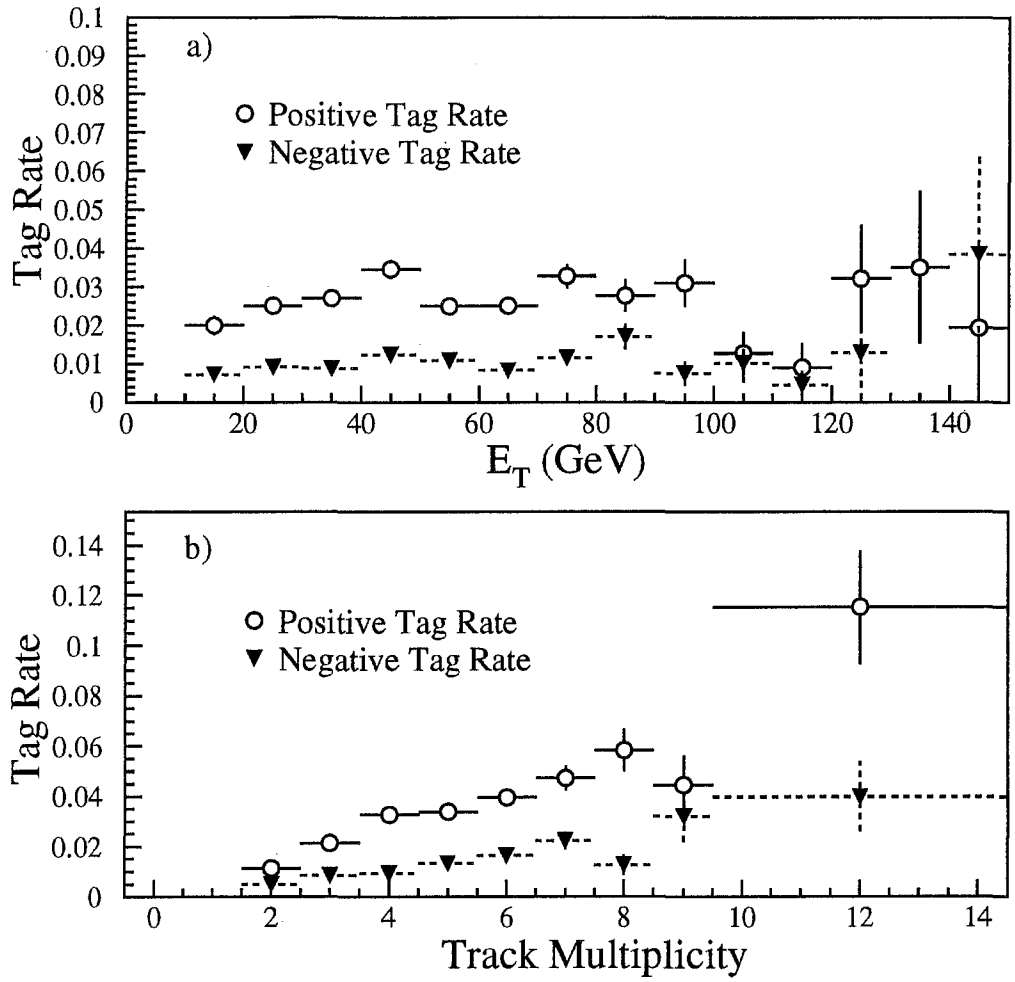

Figure 5.3: The $+L_{xy}$ tags in the JET50 sample as a function of (a) P_T and (b) the number of good tracks in a jet (N_{SVX}) showing correlations with the tag rate in each of the two variables. The open circles are the $+L_{xy}$ tag rate, and the closed triangles are the $-L_{xy}$ tag rate.

N_{JET}	$+L_{xy}$ Prediction
1	12.7 ± 1.7
2	4.86 ± 0.63
≥ 3	1.99 ± 0.26

Table 5.2: The predicted mistags from the $+L_{xy}$ tag matrix in the W+jet event sample. The uncertainties are due both statistical and systematic uncertainties.

The standard application of the scaling method predicts 2.1 tagged jets in the signal sample. The 2.1 tagged jets are reduced to 1.99 tagged events when the chance of more than one tag due to detector effects, $Wb\bar{b}$, or $Wc\bar{c}$ in an event is accounted for. Table 5.2 shows the predictions in all jet multiplicity bins (N_{JET}) in the W+jets data sample.

5.1.2 Checks in Control Samples

Control samples with a similar expected heavy flavor content are used to test the background calculation and determine the systematic error of the procedure. Table 5.3 lists the observed tags and the predictions for $+L_{xy}$ and $-L_{xy}$ tags in the JET100 sample, the photon sample (looking at jets opposite a photon), the $\sum E_T$ sample, which contains events with total energy greater than 300 GeV, and the Z+jets sample. Agreement between observed and predicted tags is good in almost all samples except in the number of $-L_{xy}$ tags in the $\sum E_T$ sample, which are high by 39%.

The $\sum E_T$ sample is different from the W+jets and JET50 data samples in the run range it covers and its jet E_T distribution. The $-L_{xy}$ discrepancy is reduced to a 10% effect when the $\sum E_T$ sample is limited to a run range similar to the JET50 sample and is limited to jets with a jet E_T less than 100 GeV[23].

	$+L_{xy}$		$-L_{xy}$	
Sample	Tags	Predicted	Tags	Predicted
JET100	229	248	92	109
Photon 16	67	63	17	20
$\sum E_T$	349	319	162	117
Z+jets	2	2.1	0	0.7

Table 5.3: JETVTX tags and predictions in the control samples.

Only two events in the $W+\geq 3$ jet sample are outside this run range (neither are tagged). The signal sample does not contain jets with a large E_T (the highest jet E_T in the sample is 110 GeV). The $\sum E_T$ sample's requirement of $\sum E_T >$ 300 GeV preferentially selects events with very high jet energies. The JET50 sample does not have many jets in that jet E_T range either, and, thus the prediction is statistically limited in the high jet E_T range. The $\sum E_T$ of the $W+\geq 3$ jet and JET50 data samples are well matched, however (see Figure 5.4).

The size of the systematic uncertainties for this prediction method are determined by the results of the control sample studies and the decrease in tagging rate that occurred during the course of Run IA. The SVX was damaged by radiation during Run IA, and this caused the track efficiency of the SVX to decrease, and thus its tagging rate to decrease as well. The decrease is an 8% effect in the tagging rate. In the control samples there is a $\pm$ 10% difference between the predicted $+L_{xy}$ tags and observed $+L_{xy}$ tags, and a $\pm$39% uncertainty in the $-L_{xy}$ tags.

The total systematic uncertainty for the $+L_{xy}$ predictions is $\pm$ 13%, and for the $-L_{xy}$ predictions, it is $\pm$ 39%. In the $W+\geq 3$ jet sample there are 1.99 $\pm$ 0.26 tags predicted due to $Wb\bar{b}$, $Wc\bar{c}$, and mistag sources. Table 5.2 shows the tags expected and their uncertainties in each jet bin.

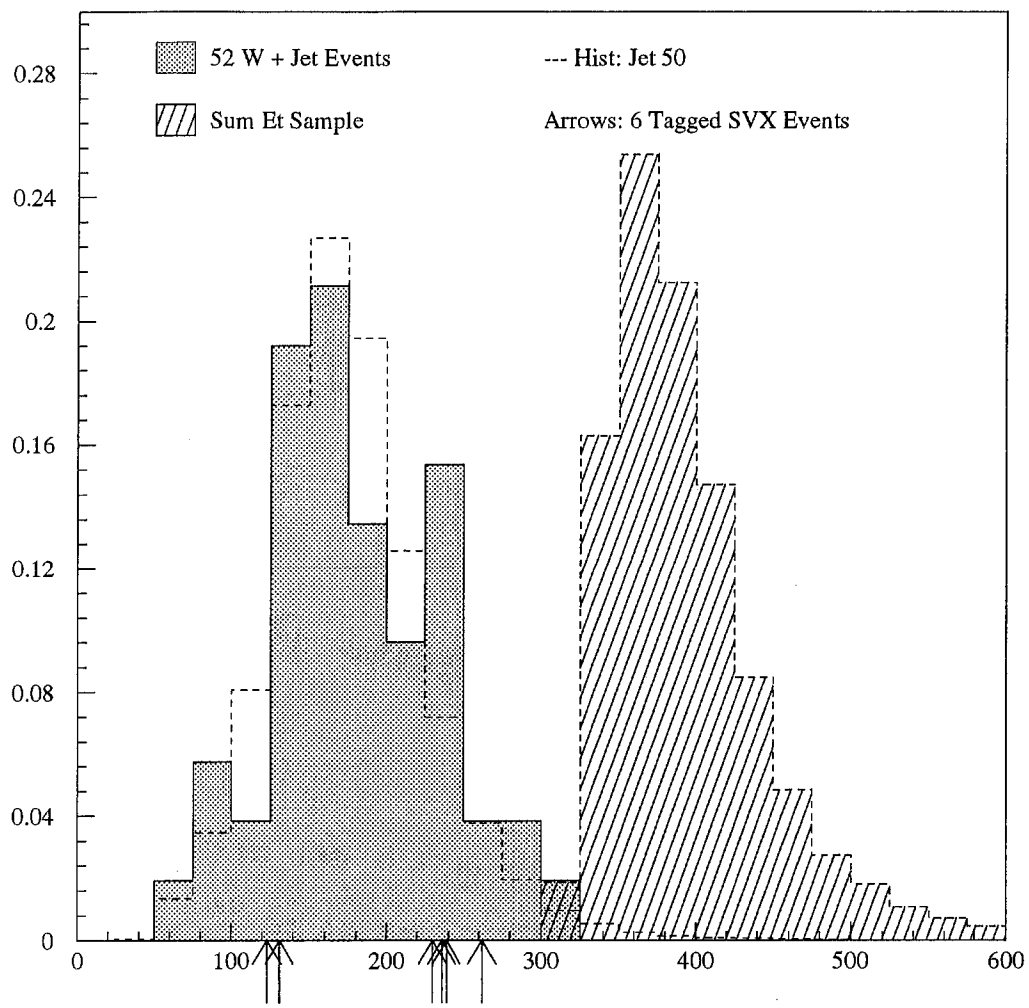

Figure 5.4: The $\sum E_T$ for the JET50 sample (dashed histogram), the W+jets signal sample (dot shading), and for the $\sum E_T$ sample (cross hatch). The arrows are $\sum E_T$ values for the tagged W+jet events, as described in Section 4.4

5.1.3 The Tag Rate Parameterization

The use of the tag matrix to predict background tags in the W+jet sample could be in error if the JET50 tag rate isn't parameterized correctly. There will be a bias in the prediction if there is a variable that the tag rate is correlated with, and the distribution of that variable is different in the W+jets and JET50 data samples. The standard tag matrix is parameterized by jet E_T and N_{SVX} because the tag rate is correlated with both. By parameterizing the tag matrix the correlations are accounted for. We search for correlations with other variables by plotting the observed $+L_{xy}$ tags and the predicted tags as a function of the suspected variable. Two variables one might worry about are the $\sum E_T$, because of the poor match in the $-L_{xy}$ tag prediction of the $\sum E_T$ sample, and N_{JET}, because that distribution is known to be different in the JET50 and $W+\geq 3$ jet samples. Figure 5.5 shows the observed tags (points) and predicted background tags (solid histogram) as a function of $\sum E_T$ and N_{JET} in the JET50 data sample. Note there is a systematic shift in the N_{JET} distribution, indicating there is a small correlation between N_{JET} and the background prediction. More tags are predicted than observed, a conservative error. There is no such correlation in the $\sum E_T$ variable. The correlations observed in other variables are smaller than the systematic uncertainty assigned the background calculation.

A second check of the background prediction is to re-parameterize the JET50 tag rate by other variables. Resulting tag matrices are used to predict the number of background tags in the $W+\geq 3$ jet sample. The predictions can then be compared to the 1.99 ± 0.26 background tags predicted by the standard tag matrix. The following 12 pairs of variables are used to construct 12 tag matrices:

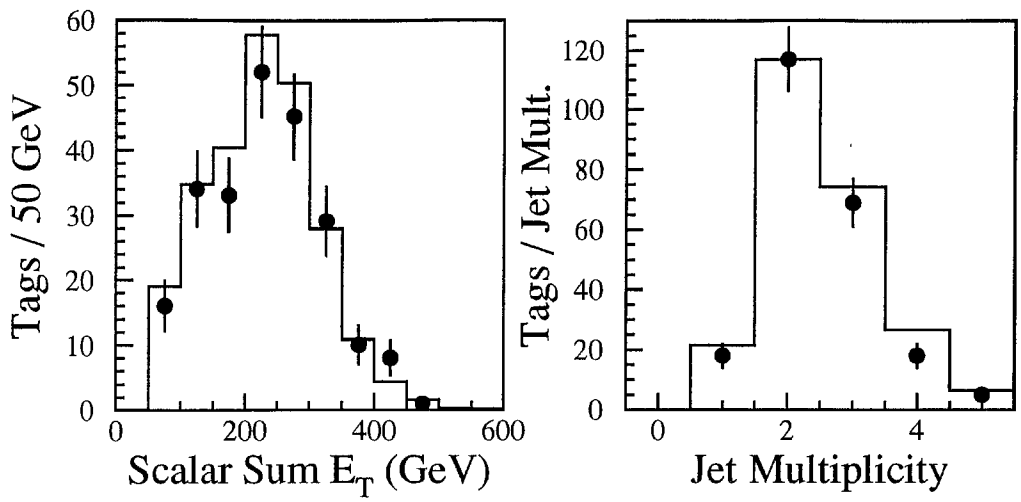

Figure 5.5: Correlations between $+L_{xy}$ tagging rates and (a) the $\sum E_T$ variable and (b) the N_{JET} variable. The points are the observed tags in the JET50 sample and the histogram is the predicted tags using the standard tag matrix. Note the systematic shift high of the predicted tags for large jet multiplicities. The differences are accounted for in the systematic uncertainty of the background measurement.

1. All SVX tracks, not just those passing the quality requirements, in a cone of $R = \sqrt{\delta\phi^2 + \delta\eta^2} = 0.4$ and the jet E_T are used to parameterize the matrix. The higher the density of hits in the SVX and CTC detectors, the more likely the tracking software is to assign a hit to the incorrect track, and therefore calculate incorrect tracking parameters.

2. All CTC tracks in a cone of 0.4 and the jet E_T are used to parameterize the matrix. Again, no track quality requirements are applied to the CTC tracks.

3. The $\sum P_T$ of all good SVX tracks (those that pass the list of track quality requirements in Section 4.1) and the N_{SVX} are used to parameterize the matrix.

4. The average $\delta\phi$ (2d opening angle) between good SVX tracks and the

cental axis of the jet and the jet E_T are used to parameterize the matrix.

5. The average χ^2 per degree of freedom (χ^2_{dof}) for the good SVX tracks and N_{SVX} are used to parameterize the matrix.

6. The average CTC track quality for good SVX tracks and the jet E_T are used to parameterize the matrix. The CTC track quality is a variable between zero and one that takes into account the number of stereo and axial layer hits and the calculated χ^2 of the CTC track fit.

7. The minimum CTC track quality for good SVX tracks and the jet E_T are used to parameterize the matrix.

8. The average number of clusters near a good SVX track, for good tracks, and the jet E_T are used to parameterize the matrix. The number of clusters near a track is found by adding up the total number of clusters on all four SVX layers that are within a 4σ radius of the track vector. Here, σ is the uncertainty in the CTC impact parameter.

9. The maximum number of clusters near a good SVX track and the jet E_T are used to parameterize the matrix.

10. The minimum number of CTC hits attached to a track for good SVX tracks and the jet E_T are used to parameterize the matrix.

11. The total number of good tracks in the event (as opposed to associated with a single jet) and the jet E_T are used to parameterize the matrix.

12. The jet multiplicity for the event and the jet E_T are used to parameterize the matrix.

Each of the 12 sets of variables is used to create a parameterization of the JET50 tag rate. Figure 5.6 shows the results of using each tag matrix to predict the number of tags in the signal sample (points). The solid central line is the standard tag matrix prediction of 2.1 events (before double tags subtraction is done). The upper and lower solid lines represent the errors on the standard background tag prediction. The standard matrix gives the largest background tag prediction, though all of the predictions are consistent with it. Tag matrices that are a function of three variables were also explored, with similar results.

5.1.4 The Monte Carlo Check

As previously discussed, the background prediction of 1.99 ± 0.26 tags in the $W+ \geq 3$ jet sample due to $Wb\bar{b}$, $Wc\bar{c}$, and detector effects is thought to be an overestimate because the heavy flavor rate in the JET50 sample is greater than the heavy flavor rate in the signal sample. The size of the overestimate can be quantified by calculating the gluon splitting contribution directly from a Monte Carlo simulation.

The number of tags due to detector effects in the $W+ \geq 3$ jet sample, however, can not be determined by Monte Carlo calculations, as the simulation does not accurately simulate the rate of mistags. Rather, the $-L_{xy}$ tags in the JET50 sample are used. Figure 5.1 shows the $c\tau_{eff}$ distribution for the tags in the JET50 sample. The fit to a $b\bar{b}$, a $c\bar{c}$, and a background Monte Carlo generated sample shows that the negative tags are due mostly to non-heavy-flavor jets (see Figure 5.1). All small portion are due to positive tags ($\sim 35\%$). The $-L_{xy}$ tag rate does not scale with the b-fraction, as can be seen by comparing Figure 5.1 to Figure 4.7, the ICE sample's $c\tau_{eff}$ distribution.

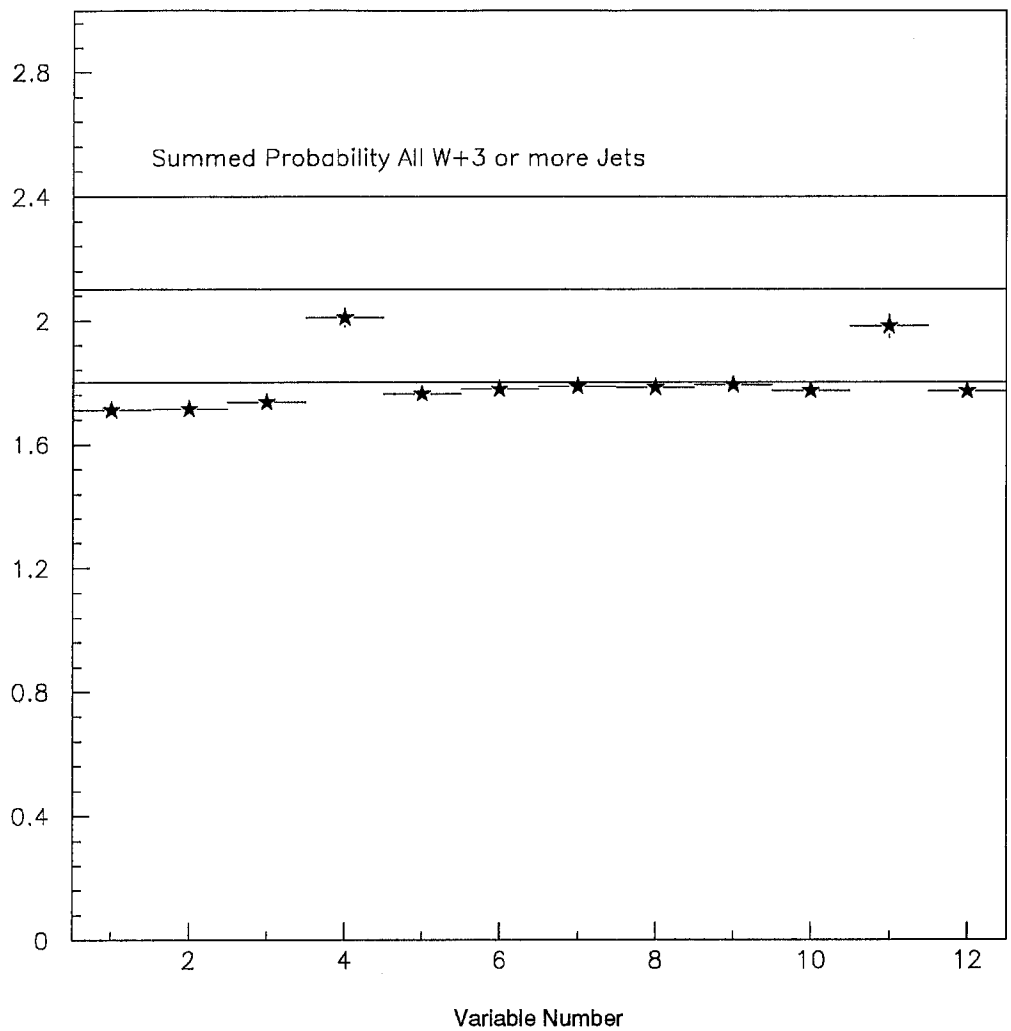

Figure 5.6: Results using the 12 tag matrices to predict background tags in the $W+ \geq 3$ jet sample (points). See text for description of each of the 12 variables. The central solid line is the predicted background tags from the standard tag matrix, and the surrounding solid lines are the error bars on that prediction, both statistical and systematic uncertainties are included.

N_{JET}	$-L_{xy}$ Prediction
1	4.8 ± 2.5
2	1.85 ± 0.98
≥ 3	0.76 ± 0.43

Table 5.4: The predicted mistags calculated by the $-L_{xy}$ tag matrix in the W+jet event sample. The largest uncertainty is due to the mismatch in $-L_{xy}$ tag rates in the $\sum E_T$ sample.

The negative tag rate in the b-quark enriched ICE sample is a much smaller proportion of the total tags in the ICE sample.

The JET50 tags due to the background Monte Carlo are symmetric about L_{xy}=0, which means the $-L_{xy}$ tags can be used to predict the $+L_{xy}$ tags due to detector effects. The symmetry of $-L_{xy}$ tags has been verified in data by taking tracks from one jet and inserting them in a different jet. The tagging algorithm is then applied to this sample. It is unlikely that any heavy flavor will be tagged in this case, and the L_{xy} distribution is symmetric about L_{xy}=0 in this sample of modified jets.

The fact that the $-L_{xy}$ tag rate is mostly independent of the b-quark fraction and is symmetric about L_{xy}=0 makes a tag matrix generated by the $-L_{xy}$ tags an excellent predictor of the number $+L_{xy}$ tags due to detector effects in the $W+\geq 3$ jet sample. The $-L_{xy}$ tag rate in the JET50 sample is parameterized the same way as the $+L_{xy}$ tag rate, and applied to the $W+\geq 3$ jet sample in the same way. The predicted mistags in the W+jet sample are shown in Table 5.4.

The $Wb\bar{b}$ and $Wc\bar{c}$ Monte Carlo program used to estimate the heavy flavor content of the $W+\geq 3$ jet sample is based on calculations performed by Mangano[13]. The calculation includes only the lowest-order W+jet diagram (see Figure 5.7a), however, unlike other Monte Carlo calculations that include

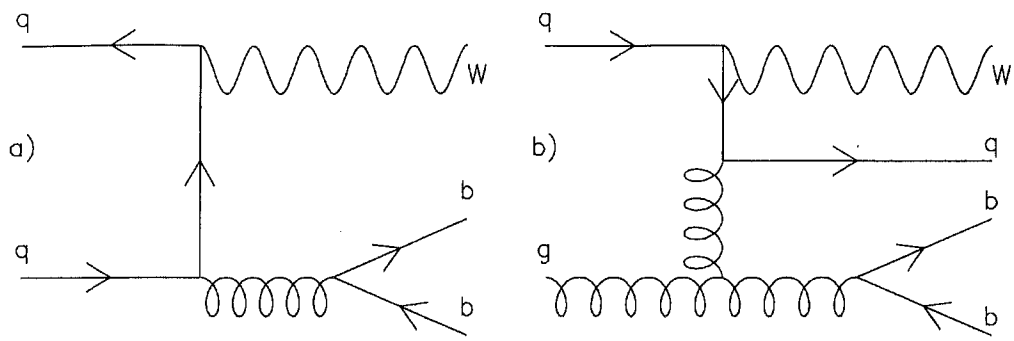

Figure 5.7: The lowest order (a) $Wb\bar{b}$ and $Wc\bar{c}$ production diagram that is calculated by the modified HERWIG Monte Carlo calculation. A second, higher order, diagram is also shown in (b).

higher-order diagrams, it does include quark mass effects. This means there is no requirement on the minimum P_T or angular separation of the b-quarks. The calculation has been incorporated into the HERWIG Monte Carlo generator, which includes parton evolution. The expected number of $Wb\bar{b}$ and $Wc\bar{c}$ events in the W+jet data is determined by multiplying the predicted fraction of $Wb\bar{b}$ and $Wc\bar{c}$ events by the number of observed events in the data, after subtracting non-W backgrounds. The expected number of $Wb\bar{b}$ and $Wc\bar{c}$ is scaled by the tagging efficiency to determine the expected number of tags.

The procedure and the ability of the HERWIG program to predict the heavy flavor content of multi-jet events are tested in the JET50 and $\sum E_T$ data samples. Figure 5.8 shows the excess $+L_{xy}$ tagging rate (i.e., $(+L_{xy})$ $-$ $(-L_{xy})$) as a function of jet multiplicity in the JET50 sample, and as a function of jet E_T in the $\sum E_T$ sample. HERWIG's prediction matches well with the observed tags.

Determining the number of background tags in the W+jet sample due to $Wb\bar{b}$ and $Wc\bar{c}$ events is not as straightforward because the Monte Carlo tools aren't sufficiently powerful. The modified HERWIG calculation includes only

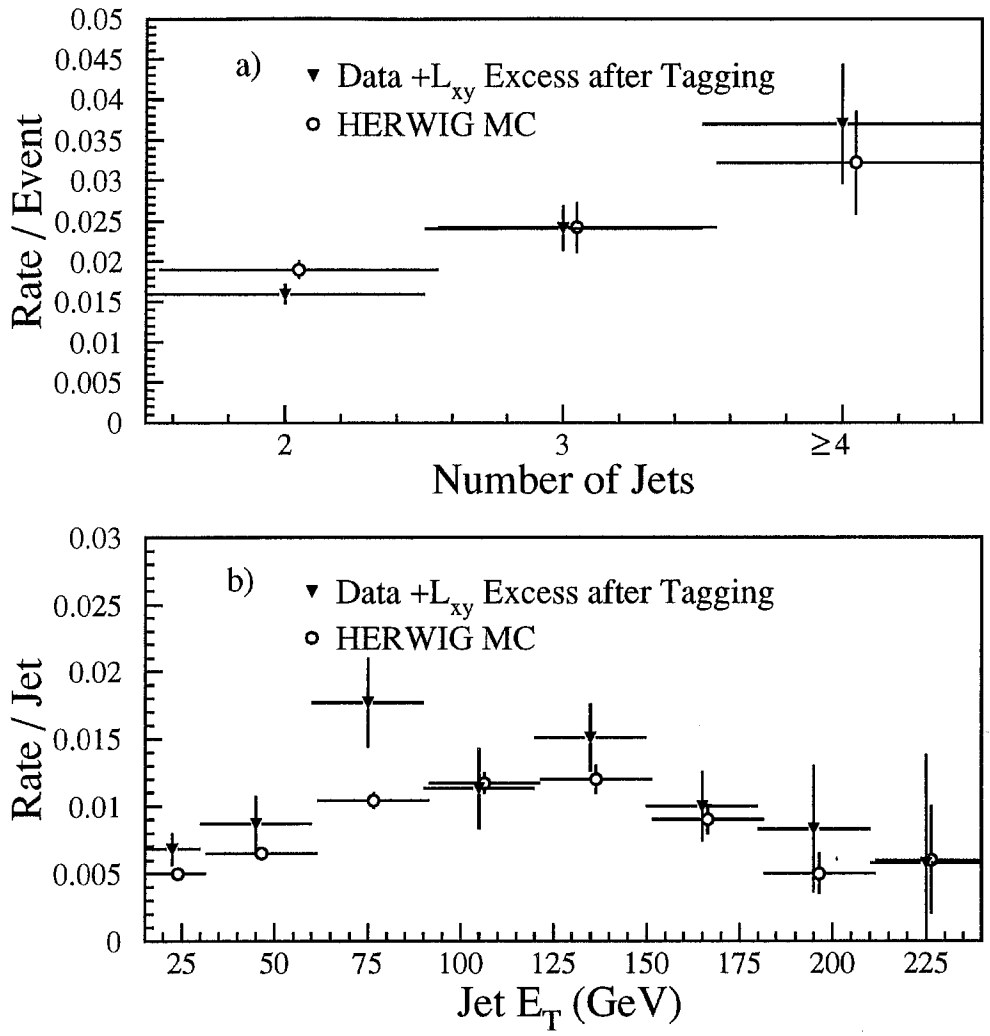

Figure 5.8: The observed excess tags (solid triangles) and the Monte Carlo predicted tags (open circles) in the JET50 sample, shown as a function of jet E_T and N_{JET}. The prediction uses the HERWIG Monte Carlo calculation for the heavy flavor prediction.

	$W+$ 1 jet	$W+2$ jet
HERWIG Prediction	5.8	1.0
Standard HERWIG Prediction	3.7	0.9
Standard HERWIG Normalized	5.1	1.7

Table 5.5: The number of $Wb\bar{b}$ events predicted by HERWIG's calculation as well as standard HERWIG in the $W+1$ and 2 jet data samples. The complete detector simulation and the analysis (excluding the b-tag requirement) are used. Only the $W \rightarrow e\bar{\nu}$ channel is shown. The default HERWIG prediction, both raw and normalized to the number of $W+1$ jets observed in the data, is also listed for comparison.

the lowest order production diagram, and does not model $W+\geq 3$ jet events well. The standard HERWIG calculation does model $W+\geq 3$ jet well, but does not include mass effects of the $g \rightarrow q\bar{q}$ decay. As a result, a combination of the two is used. We use the fraction of events containing a b-quark or a c-quark predicted by the modified HERWIG calculation instead of the absolute cross section to avoid any uncertainty in the absolute HERWIG normalization of the $W+$jets rate. Finally, the modified HERWIG calculation forces the W boson to decay to $e\bar{\nu}$; results are multiplied by two to include the $W \rightarrow \mu\bar{\nu}$ decay. First, the modified HERWIG calculation is used to predict the number of b-quark or c-quark jets in the $W \rightarrow e\bar{\nu}$ channel. Though we do not have to worry about the overall $W+$jet rate normalization, there is an uncertainty in the relative normalization of the heavy flavor production rate. This uncertainty is estimated to be $\pm 40\%$ in Reference [13]. To be conservative, we use the upper value, and scale all of the modified HERWIG predictions by 1.4. Table 5.5 compares the standard and modified HERWIG predictions in the $W+1$ and $W+2$ jet bins of the $W+$jet data sample.

The modified HERWIG calculation includes only the leading order term

N_{JET}	$Wb\bar{b}(\%)$	$Wc\bar{c}(\%)$
1	0.53 ± 0.20	1.19 ± 0.04
2	1.04 ± 0.08	2.45 ± 0.13
3	2.11 ± 0.30	3.45 ± 0.48
4	2.50 ± 1.2	2.70 ± 1.50

Table 5.6: Fraction of W+jet events with at least one b-quark jet. The numbers are from the standard HERWIG calculation. A scale factor of 1.4 ± 0.8 is applied to make the $W + 1$ jet bin match the modified HERWIG calculation.

and thus is not expected to accurately predict the W+3 and W+4 jet rates. The standard HERWIG calculation includes the higher order Feynman diagrams, but not the mass effects. It is used to extend the modified HERWIG calculation to higher jet multiplicities. Table 5.6 lists the prediction by the standard HERWIG calculation of the fraction of events that contain at least one b-quark (or c-quark) as a function of jet multiplicity. A scale factor of 1.4 ± 0.8 is applied to the rates so that the expected $Wb\bar{b}$ rates match in the W+1 jet bin of standard and modified HERWIG simulations. The systematic error of ± 0.8 is determined by increasing the gluon splitting rate in the modified HERWIG until the tag rate in the simulation is 1σ above the tag rate in a JET20 sample. The gluon splitting rate is increased a factor of 2.2 to attain the elevated rate of tagging (no scale factor of 1.4 due to the uncertainty in the heavy quark production rate is applied). This translates to a systematic error of ± 0.8 on the factor of 1.4 (2.2-1.4). The number of W+jet events containing a $Wb\bar{b}$ or a $Wc\bar{c}$ before tagging is determined by scaling the number of W+jets events, after non-W background subtraction, by the fractions.

The $Wb\bar{b}$ tagging rate is determined using the $W + 1$ and $W + 2$ jet events generated by the modified HERWIG simulation. The tag rate is found to be 20% in W+1 jet events, and 28% in W+2 jet events after applying the

N_{JET}	$Wb\bar{b}+ Wc\bar{c}$
1	2.7 ± 2.2
2	1.05 ± 0.85
≥ 3	0.37 ± 0.31

Table 5.7: Predicted $Wb\bar{b}$ and $Wc\bar{c}$ tags in W+1, 2, and 3 or more jet events by the modified HERWIG calculation.

data/Monte Carlo scale factor, F_{scale}. Three, four, five, etc. jet events are assigned the same tagging rate as the W+2 jet events because it is very unlikely that there is a second $b\bar{b}$ pair in the event. For $Wc\bar{c}$ events, the tag rate is 5% for all jet multiplicities. Table 5.7 lists the number of predicted tags due to $Wb\bar{b}$ and $Wc\bar{c}$ events in the W+jets data sample. The systematic errors in the tag efficiency ($\pm$30%), the heavy flavor content ($\pm$35%), the 1.4 ± 0.8 scale factor, and the dependance on jet multiplicity (based on Figure 5.8) of $\pm$40% are added in quadrature, and rounded to a $\pm$80% uncertainty in the expected number of tags.

Table 5.2 and Table 5.7 are added together to get the predicted background tags due to $Wb\bar{b}$, $Wc\bar{c}$, and detector effects. The Monte Carlo check predicts a total of 1.13 ± 0.53 tags in the $W+\geq 3$ jet sample, as compared to the 1.99 ± 0.26 events predicted by the standard tag matrix. The tag matrix prediction is inherently conservative, as it attempts to estimate the background with minimal reliance on Monte Carlo simulations. Specifically, the tag matrix calculation

1. does not implicitly assume the mistag rate for negative and positive tags is the same (though this is thought to be case),

2. includes residual tags from K_s mesons, Λ baryons, and conversions, and,

3. includes the real rate of $b\bar{b}$ and $c\bar{c}$ along with the actual tagging efficiency of those jets.

5.2 The Remaining Backgrounds

Most of the remaining background (Wc, $Z \rightarrow \tau\tau$, and dibosons) are calculated using Monte Carlo simulations. The Monte Carlo simulation is used to find the cross section and pre-tagging acceptance, and a tagging rate is applied to find the expected contribution to the background tags in the $W+\geq 3$ jet sample. The non-W background is calculated directly from the data. The following sections describe each background calculation in more detail.

5.2.1 Wc Contributions

The Wc production proceeds, to lowest order, by gluon fusion with a strange quark from the proton sea, the Feynman diagram for which is shown in Figure 5.9a. Figure 5.9b is a second production mechanism, however, it is Cabibbo suppressed, and contributes only 10% to 15% to the Wc production rate.

The Wc background is estimated in two steps. The fraction of Wc events passing $W+1$ jet requirements is estimated to be $(5.3 \pm 1.3)\%$ using the HERWIG Monte Carlo program. The systematic uncertainty is estimated by repeating the Monte Carlo calculation using several different structure functions. Only jets with $E_T >$ 15 GeV/c and $|\eta| < 2.0$ are examined. VECBOS is used to examine the higher order jet multiplicities. In the three jet bin, $(8.0 \pm 2.0)\%$ of events are predicted to contain a single c quark.

The second step is to check the SVX acceptance of the charm jets in the Wc events. Monte Carlo simulation shows that the acceptance for Wc events is 1.11 ± 0.03 times larger than generic W+jet events. This factor is applied

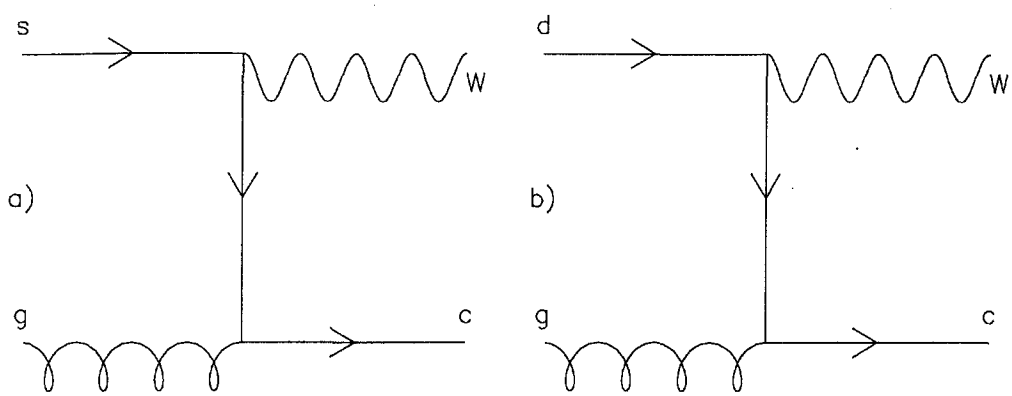

Figure 5.9: The Feynman diagrams for Wc production. Gluon fusion with a strange quark (a) and the other first order, but Cabibbo suppressed diagram (b).

to the estimate for Wc.

The tagging efficiency for a charm jet is measured in a large sample of $c\bar{c}$ HERWIG Monte Carlo generated events. After applying F_{scale} (see Section 4.2.1) to the Monte Carlo generated events, the tagging rate is found to be 4%. In the $W+\geq 3$ jet sample we expect 0.14 ± 0.07 tags due to events containing Wc production. Table 5.16 lists the results in all the jet bins.

5.2.2 Non-W Contributions

Estimating the background due to non-W events can be conveniently divided into two steps. First, the rate of non-W events in the signal sample is calculated, and then the rate at which the events are tagged is estimated.

An I *vs.* $\not{E}_T$ method, described in Section 3.4, is used estimate the amount of non-W events in the $W+\geq 3$ jet sample. Table 5.8 summarizes the expected number of non-W events in the muon and electron samples.

There is a potential for double counting that must be avoided when calculating the tagging rate and the number of tagged events. The tag matrix

N_{JET}	e	μ
1	7.4 ± 0.7 %	6.3 ± 0.9 %
≥2	6.8 ± 1.5 %	10.8 ± 2.8 %

Table 5.8: Estimated non-W events in the electron and muon W event samples. Estimates are made using the I *vs.* $\not\!\!E_T$ scaling.

calculation assumes that, on average, events in the $W+\geq 3$ jet sample have the same (or smaller) heavy flavor content as the JET50 sample. In the case of non-W events, especially $b\bar{b}$, the premise that the tag rate is the same as the JET50 sample will not be true. The excess of the expected tags over the expected number of tags predicted by the standard tag matrix is determined to avoid double counting.

The tagging rate is dependant on the lepton isolation (I). The tagging rate in the $I < 0.1$ and $\not\!\!E_T < 15$ GeV region is used to estimate the tagging rate of the non-W events in the signal region, I < 0.1 and $\not\!\!E_T > 20$ GeV.

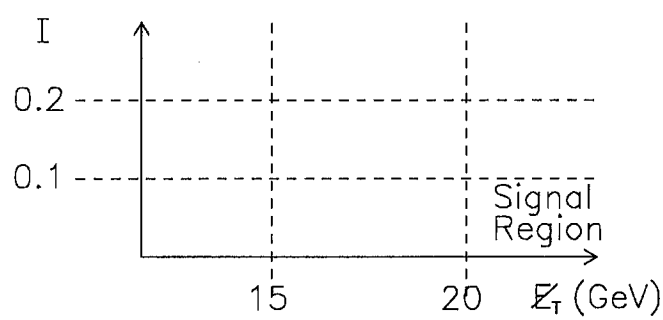

This assumes that the tagging rate is constant in $b\bar{b}$ and other non-W events with respect to $\not\!\!E_T$. $b\bar{b}$ Monte Carlo simulations verify this assumption for the $b\bar{b}$ component of the non-W background. A second assumption made is that the $\not\!\!E_T$ distribution for $b\bar{b}$ and other non-W events is identical. The raw tagging rates are shown in Table 5.9, along with the excess rate in the low $\not\!\!E_T$ region. Table 5.10 shows the expected tags in the signal region due to non-W events.

	$+L_{xy}$ Rate	Excess $+L_{xy}$ Rate
W+1 Jet, e	$0.7 \pm 0.2\%$	$0.2 \pm 0.2\%$
W+2 Jet, e	$3.0 \pm 1.3\%$	$0.7 \pm 1.2\%$
W+1 Jet, μ	$1.6 \pm 0.5\%$	$0.9 \pm 0.6\%$
W+2 Jet, μ	$6.4 \pm 2.9\%$	$4.2 \pm 3.3\%$

Table 5.9: The tagging rates in the region I < 0.1 and $\not{E}_T < 15$ GeV, and the excess tagging rate (over the predicted background from the JET50 sample).

N_{JET}	Tags Expected
1	0.5 ± 0.3
2	0.59 ± 0.44
≥ 3	0.15 ± 0.11

Table 5.10: The calculated tags in excess of the predicted tags from the tag matrix in the signal region due to non-W events.

5.2.3 $Z \rightarrow \tau\tau$ Contributions

A typical three prong τ decay is $\tau^- \rightarrow \pi^+\pi^-\pi^-\nu_\tau$. The τ can be tagged as a secondary vertex because of its long lifetime ($c\tau = 88.9$ μm)[19]. A $Z \rightarrow \tau\tau$ event will be part of the signal sample if one of the two τ leptons decays $\tau \rightarrow \mu\bar{\nu}_\mu\nu_\tau$ or $\tau \rightarrow e\bar{\nu}_e\nu_\tau$ and the e or μ passes the high-P_T lepton requirements. The $Z \rightarrow \tau\tau$ event will almost always be classified as a W+1 jet event, however.

The number of $Z \rightarrow \tau\tau$ events before tagging is:

$$N_{1jet}(Z \rightarrow \tau\tau) = N_{1Jet} \times \frac{1}{R} \times \frac{Br(Z \rightarrow \tau\tau)}{Br(Z \rightarrow ee)} \times \frac{\epsilon_Z}{\epsilon_W}$$

where $N_{1jet}(Z \rightarrow \tau\tau)$ is the predicted number of $Z \rightarrow \tau\tau$ events passing the W+1 jet selection criteria before tagging, N_{1jet} is the number of observed

events passing the $W+1$ jet selection criteria, and

$$R = \frac{\sigma Br(\bar{p}p \rightarrow W \rightarrow e\bar{\nu})}{\sigma Br(\bar{p}p \rightarrow Z \rightarrow ee)},$$

$$\epsilon_Z = \frac{\#\text{of } Z \rightarrow \tau\tau \text{ events passing } W{+}1 \text{ jet selection criteria in MC}}{\#\text{ of } Z \rightarrow \tau\tau \text{ events generated in MC}},$$

and

$$\epsilon_W = \frac{\#\text{ of } W \rightarrow e\bar{\nu} \text{ events passing } W{+}1 \text{ jet selection criteria in MC}}{\#\text{ of } W \rightarrow e\bar{\nu} \text{ events generated in MC}}.$$

The ratio, R, of W and Z cross sections times branching ratios has been published by CDF, $R = 10.2 \pm 0.8 \pm 0.4$[24]. The ratio of the $Z \rightarrow \tau\tau$ and $Z \rightarrow ee$ branching ratios is taken to be 1. The last term, ϵ_Z/ϵ_W, must be determined by Monte Carlo simulation. Since it is a ratio of efficiencies, most Monte Carlo systematic uncertainties should cancel. Table 5.11 shows the Monte Carlo measured efficiencies. There are

$$N_{1jet}(Z \rightarrow \tau\tau) = N_{1jet} \times (0.033 \pm 0.006) \tag{5.1}$$

$Z \rightarrow \tau\tau$ events expected before tagging, in the $W{+}1$ jet sample. To extend to higher jet multiplicities the assumption is made that the chance of each extra jet in the event is similar to that in the W sample. If higher jet multiplicities of $Z \rightarrow \tau\tau$ events occur at the same rate as in the $W{+}$jet sample (replace N_{1jet} by N_{2jet} or N_{3jet} in Equation 5.1), then the expected number of $Z \rightarrow \tau\tau$ decays in the $W{+}2$ or $W{+}\geq 3$ jet bins is negligible. Table 5.12 lists the numbers of $Z \rightarrow \tau\tau$ background events expected to fall into the $W+1$ jet bin before tagging. The table also shows the expected number of tags in the $W+1$ jet bin. The tag rate is estimated from Monte Carlo simulations.

	Efficiency
ϵ_W	$(0.98 \pm 0.04)\%$
ϵ_Z	$(0.033 \pm 0.005)\%$

Table 5.11: ϵ_W and ϵ_Z, efficiency for $Z \rightarrow \tau\tau$ and $W \rightarrow e\bar{\nu}$ events to pass the W+1 jet event selection requirements.

	Events
Before Tagging	5.6 ± 10.28
After Tagging	$0.09 \pm .16$

Table 5.12: Expected $Z \rightarrow \tau\tau$ events in the W+1 jet bin before and after tagging has been applied. Only the $W + 1$ jet case is examined, as there is expected to be negligible contributions to the higher jet multiplicities. The tagging rate is $0.016 \pm 0.012\%$.

5.2.4 Diboson Contributions

There is a small contribution from diboson production, such as WW and WZ, where one of the W bosons decays leptonically and the second decays into a long lived particle(s) (i.e., $Z \rightarrow b\bar{b}$ or $W \rightarrow c\bar{s}$). Figure 5.10 shows the production diagrams for the two processes.

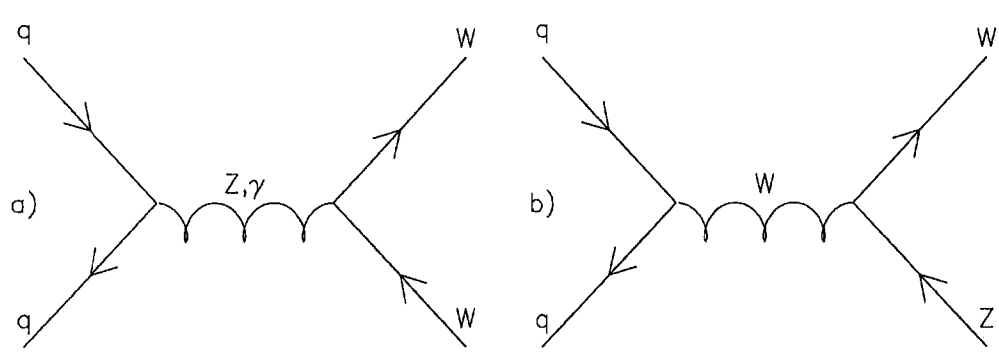

Figure 5.10: The lowest order WW and WZ production diagrams.

The cross section of diboson events before tagging is given by

$$\sigma_N = [\sigma \times Br] \times \epsilon_{kin} \times \epsilon_l,$$

where σ is the cross section for diboson production, Br is the branching ratio for the diboson state to decay to a long lived state, $Br(WW \rightarrow e\bar{\nu}c\bar{s})$ or $Br(WZ \rightarrow e\bar{\nu}b\bar{b})$, ϵ_l is the lepton identification efficiency detailed below, and ϵ_{kin} is the kinematic selection efficiency listed in Table 5.13.

The production cross sections for both processes are expected to be small, $\sigma(WW) = 9.5 \pm 0.5 \pm 0.5\ pb$ and $\sigma(WZ) = 2.6 \pm 0.3 \pm 0.3\ pb$, where the first uncertainty is due to the uncertainty in structure functions and the second is due the Q^2 scale[25]. The electron identification efficiency is

84 ± 3 %	electron ID efficiency
93 %	trigger efficiency
95 %	conversion removal
$\epsilon_e =$ 74%,	

and the muon identification efficiency is

95 %	muon ID efficiency
87 %	trigger efficiency
$\epsilon_\mu =$ 83%.	

The values of σ_N for the processes, decay channels, and jet multiplicity bins are listed in Table 5.14. The tagging rate is estimated using the ISAJET Monte Carlo generator and the data/Monte Carlo scale factor (F_{scale}) is applied. The results are shown in Table 5.15. Table 5.16 lists the expected tags in the W+jet sample.

Jet Multiplicity	ϵ	ϵ
	Electrons	
1 jet	12.3 ± 0.4	10.4 ± 0.4
2 jets	14.9 ± 0.8	13.8 ± 0.8
$\geq$3 jets	5.9 ± 0.5	4.8 ± 0.5
	Muons	
1 jet	6.4 ± 0.5	6.3 ± 0.5
2 jets	8.1 ± 0.6	6.7 ± 0.5
$\geq$3 jets	3.3 ± 0.4	2.4 ± 0.3

Table 5.13: The diboson kinematic selection efficiencies, in percent.

Jet Multiplicity	$\sigma_N(WW)$ (pb)	$\sigma_N(WZ)$ (pb)
	Electrons	
1 jet	0.064 ± 0.019	0.004 ± 0.001
2 jets	0.077 ± 0.024	0.005 ± 0.002
$\geq$3 jets	0.031 ± 0.012	0.002 ± 0.001
	Muons	
1 jet	0.037 ± 0.011	0.003 ± 0.001
2 jets	0.047 ± 0.014	0.003 ± 0.001
$\geq$3 jets	0.019 ± 0.008	0.001 ± 0.001

Table 5.14: The diboson cross section in pb before tagging for the various decay channels, listed by jet multiplicity.

Jet Multiplicity	WW	WZ
1 jet	0.02612 ± 0.00974	0.18077 ± 0.02387
2 jets	0.04023 ± 0.01490	0.32642 ± 0.03375
$\geq$ 3 jets	0.00000 ± 0.00000	0.38889 ± 0.11490

Table 5.15: The event tagging rates for the diboson backgrounds.

Source	$W+1$ Jet	$W+2$ Jets	$W+\geq 3$ Jets
Backgrounds From Data			
$Wb\bar{b}$, $Wc\bar{c}$+ Mistags	12.7 ± 1.7	4.86 ± 0.63	1.99 ± 0.26
Monte Carlo Check			
$Wb\bar{b}$, $Wc\bar{c}$ only	2.7 ± 2.2	1.05 ± 0.85	0.37 ± 0.31
Mistags only	4.8 ± 2.5	1.85 ± 0.98	0.76 ± 0.43
$Wb\bar{b}$, $Wc\bar{c}$+ Mistags	7.5 ± 3.3	2.90 ± 1.30	1.13 ± 0.53
Wc	2.4 ± 0.8	0.66 ± 0.27	0.14 ± 0.07
$Z \rightarrow \tau\bar{\tau}$, WW, WZ	0.20 ± 0.10	0.19 ± 0.09	0.08 ± 0.04
Non-W, including $b\bar{b}$	0.50 ± 0.30	0.59 ± 0.44	0.09 ± 0.09
Events Before Tagging	1713	281	52
Observed Tagged Events	8	8	6
Background	15.8 ± 2.1	6.3 ± 0.8	2.30 ± 0.29
Monte Carlo Check	10.6 ± 3.7	4.3 ± 1.4	1.44 ± 0.54

Table 5.16: The total background tags expected in each jet bin in the W+jet sample.

5.3 Summary of the Backgrounds

Table 5.16 lists all the separate background contributions as well as the Monte Carlo check, in each W+jet multiplicity bin. The total expected background in the signal sample, if there were no top present, is 2.3±0.29 events, as compared to the 6 tagged events observed. The Monte Carlo check predicts a total of 1.44 ± 0.54 events. There is good agreement the between data and the number of predicted background tags in the W+1 and $W+2$ jet bins. The $W+\geq 3$ jet bin has an excess, however. The significance of this excess is discussed in the next chapter. Figure 5.11 shows the same information as Table 5.16 in the form of a histogram.

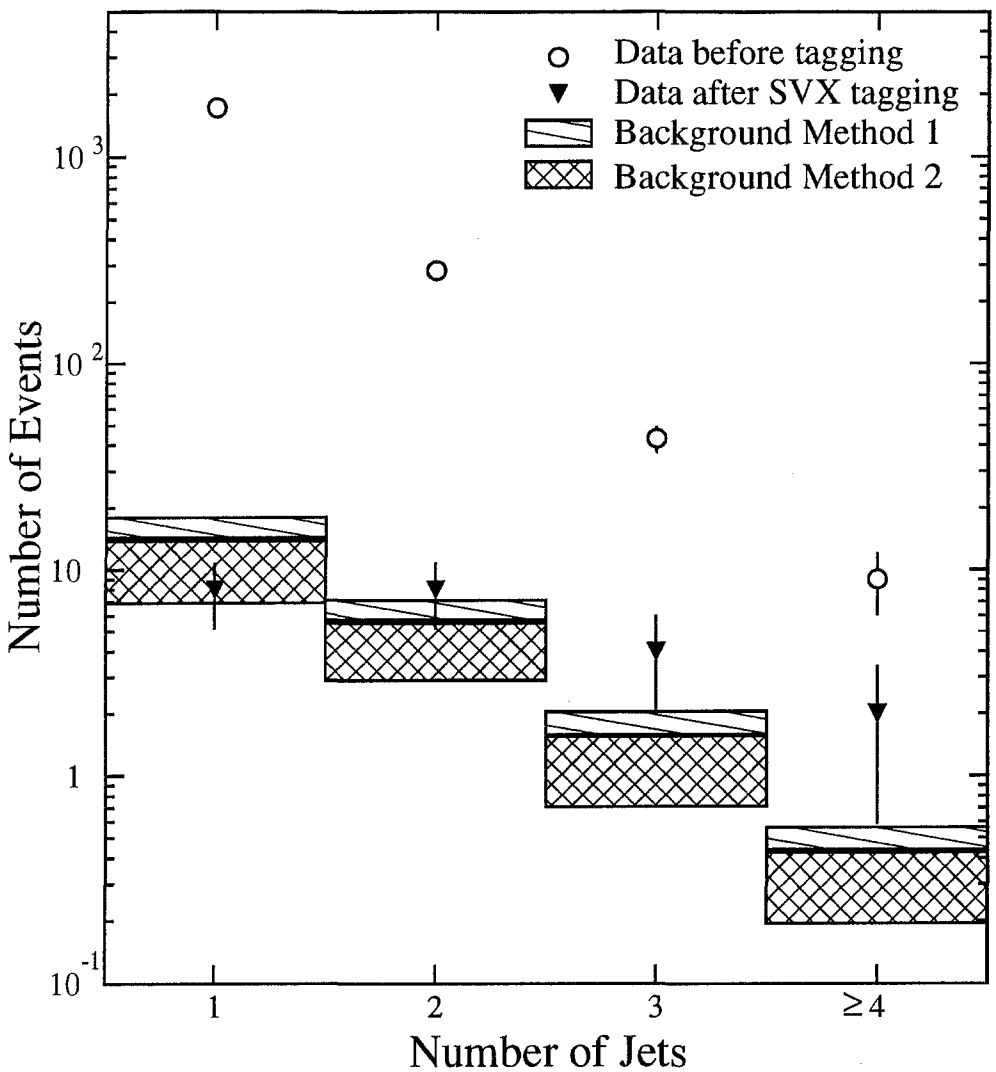

Figure 5.11: The results of the secondary vertex search in the W+jets data sample, binned by number of jets. The open circles are before secondary vertex tagging, and the solid triangles are after tagging. The cross-hatched boxes are the two after tagging background estimates.

Chapter 6

Results and Conclusions

6.1 The Counting Experiment

Chapter 5 described the calculation of the expected number of background tags due to sources other than $t\bar{t}$ production in the signal sample. The result, 2.3 ± 0.29, is less than the six tags observed in the signal sample. Poisson statistics are used to determine how statistically significant this excess is.

The 0.29 uncertainty on the predicted background is included in the significance calculation by assuming the uncertainty has a gaussian distribution. Instead of one Poisson distribution for the background, several with means of 1, 2, 3, etc. are added together, each weighted by the value of a gaussian with mean 2.3 and width 0.29 at x =1, 2, 3, etc. The fraction of the resulting distribution populating the region of six or more is 3.2%. Thus we conclude that the probability, or significance (P), is 3.2%. P is the probability that the background tags can generate the six or more observed tags.

The SVX search is only one of three top searches that have recently been published by CDF[2]. The other two are a second b-tagging search, the soft lepton search (SLT), and a search for top decaying to two leptons (a dilepton

		W+1 Jet	$W+2$ Jet	$W+3$ Jet
Events Before Tagging		1713	281	52
Events After Tagging	e	17	2	4
	μ	16	10	3
	$e+\mu$	33	12	7
Expected Backgrounds	e	11.9 ± 1.6	3.4 ± 0.4	1.1 ± 0.2
	μ	22.2 ± 2.1	6.5 ± 0.6	2.0 ± 0.2
	$e+\mu$	34.1 ± 3.3	9.9 ± 1.0	3.1 ± 0.3

Table 6.1: The results of the soft lepton top quark search. The W sample is the same as used in the secondary-vertex search.

search). While the details of both searches are beyond the scope of this thesis, the results of the SVX b-tag search should be discussed in the context of the other search results.

In the SLT top search, we attempt to tag the soft lepton from the B or charmed hadron decay $b \rightarrow \ell\bar{\nu}_\ell X$ ($\ell = e$ or μ) or $b \rightarrow c \rightarrow \ell\bar{\nu}_\ell X$ (cascade decay). The lepton P_T is required to be greater than 2 GeV/c. The signal sample is the same $W+\geq 3$ jet sample used by the secondary-vertex search. The b-tagging efficiency is measured to be $(15 \pm 2.4)\%$ for top masses between 140 GeV/c^2 and 180 GeV/c^2. Three soft electron tags and four soft muon tags are observed in the $W+\geq 3$ jet sample. The background calculation uses the same method as the secondary-vertex search, parameterizing the tag rate in the generic jet sample. In the $W+\geq 3$ jet sample, a total of 3.1 ± 0.3 background tags are expected. Table 6.1 summarizes the results. Three events are tagged by both the secondary-vertex search and the soft-lepton search, though only one of the three tags is the same jet. Figure 6.1 shows a graphical representation of the observed tags and expected backgrounds for the SVX and SLT searches, combined.

The dilepton search looks for $t\bar{t}$ production in the final states $ee\nu\bar{\nu}$, $e\mu\nu\bar{\nu}$,

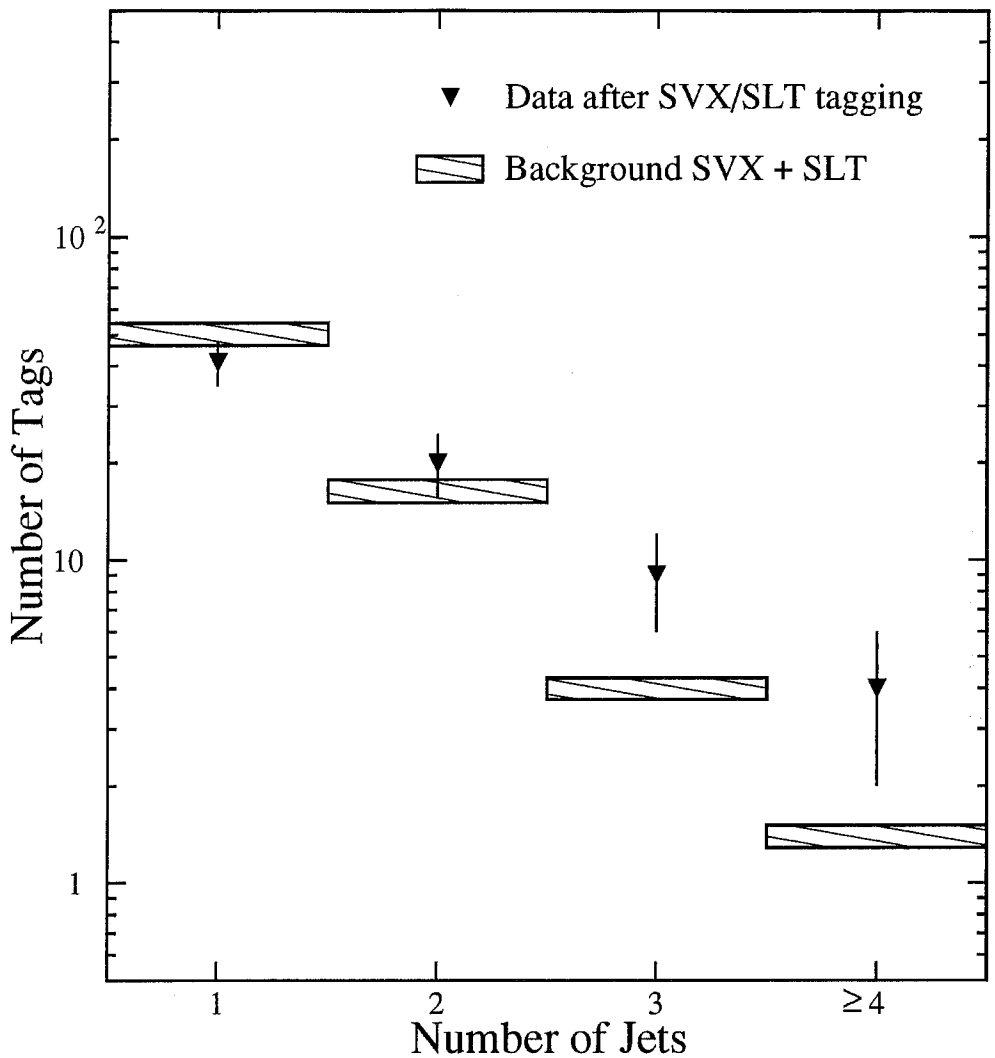

Figure 6.1: The sum of SVX and SLT tags observed in the W+jets sample (solid triangles). Events tagged by both algorithms are counted twice. The shaded area is the sum background predictions.

and $\mu\mu\nu\bar{\nu}$. The leptons are required to be oppositely charged, with a $P_T>$ 20 GeV/c. The event $\not{E}_T$ requirement is raised to 25 Gev. Each candidate event must have a central lepton satisfying requirements similar to the W+jets central lepton requirement (see Section 3.3). To increase efficiency the requirements for the second lepton are relaxed, and the lepton need not be central (it may be in the plug calorimeters). After making further kinematic requirements to reduce the backgrounds due to $Z \rightarrow \tau\tau$, $b\bar{b}$, and Drell-Yan (including a two jet (E_T>10 GeV) requirement) two $e\mu$ events survive. As in the other two searches, backgrounds are calculated by a combination of data and Monte Carlo techniques. A total of $0.56^{+0.25}_{-0.13}$ events are expected in the three final states. One of the two dilepton events also contains both a secondary-vertex and soft lepton tag, though this information is not used in determining the significance of the dilepton result.

All three searches observe an excess of events. The results of the three searches are combined to obtain an overall significance of the excess. Table 6.2 tabulates the significance for each of the three top searches. Combining the three counting experiments is done using a Monte Carlo program to simulate the various possible outcomes of the experiment. The Monte Carlo calculation accounts for fluctuations of the various sources of backgrounds as well as correlations in the tag rates (an increase in the $Wb\bar{b}$ production rate will cause an increase in the number of SVX and SLT tags for example). Details of this are beyond the scope of this thesis; see the Reference [2]. When correlations in the two lepton+jets b-tagging algorithms are taken into account and backgrounds are allowed to fluctuate appropriately, the combined significance is 2.6×10^{-3}. This corresponds to the same probability as a 2.8σ effect on a gaussian distribution. While not enough to claim a discovery of the top quark, we interpret this result as evidence for the existence of the top quark.

Search	Significance (P)
SVX b-tag	3.2%
SLT b-tag	3.8%
Dilepton	12%
Combined Significance	2.6×10^{-3}

Table 6.2: The probability of the expected background fluctuating up to the observed events in each of the three top searches detailed in CDF's recent top PRD[2].

6.2 Checks in the Z Sample

In principle, the Z+jet sample provides a good cross check of the heavy flavor content of the W+jet sample because the W and Z production mechanisms are very similar. The main difference between the two samples is that the t-quark does not decay to a Z boson and so will not be present in the Z sample. A background process producing unaccounted for heavy flavor in the W boson sample would, most likely, be present in the Z boson sample. An excess of tags in the Z boson sample might point to such a heavy flavor source. In this section we report on the results of a search for tags in a sample of Z boson events.

The procedure is similar to the tag search in the W+jet sample. The Z+jet data sample used for this study is described in Section 3.5. Table 6.3 lists the results of running both the SVX and the SLT algorithm on the sample. The background tags are calculated in the same way for the Z+jet sample as they are in the W+jet sample, except no non-Z backgrounds are included (such as $b\bar{b}$ direct production), and no contributions due to $t\bar{t}$ events are included as they are small. There are 5 events in the $Z+\geq 3$ jet region, the equivalent of the $t\bar{t}$ $W+\geq 3$ jet region. Of the 5 events, 2 are tagged by the secondary-

	$Z+1$ Jet	$Z+2$ Jet	$Z+\geq 3$ Jets
Observed Z Candidates	176	21	5
SVX Tags	0	0	2
SVX background tags	1.4±0.2	0.32±0.05	0.31±0.05
SLT Tags	6	0	0
SLT background tags	2.9±0.3	0.52 ±0.05	0.33 ±0.03
SVX + SLT Tags	6	0	2
SVX + SLT background tags	4.3 ± 0.4	0.84 ± 0.07	0.64± 0.06

Table 6.3: Summary of the rate of Z candidates both with and without b tags, and the expected backgrounds.

vertex algorithm, and 0.31±0.03 background tags are predicted. Using Poisson statistics, the likelihood of the background fluctuating up to the observed 2 events is 4%. When both the SVX and the soft lepton analysis are combined, the probability is 14% that the background will fluctuate up to the observed number tags.

The observed excess in the $Z+\geq 3$ jet sample could indicate a source of heavy flavor in the W+jet sample that we have not accounted for, even though in the $W+1$ and $W+2$ jet bins agree well (see Table 5.16). The discrepancy occurs only at high jet multiplicities, as Table 6.3 demonstrates; the $Z+1$ and $Z+2$ jet bins agree well. More statistics are required to determine if the excess Z tags are a fluctuation or due to a real source of heavy flavor.

6.3 The $t\bar{t}$ Production Cross Section

The cross sections can be simply calculated for each individual search using the relation

$$\sigma = \frac{N-b}{\mathcal{L} \times \epsilon_{top}}$$

	SVX	SLT
$N_{t\bar{t}}$	19.6 ± 9.5	29.0 ± 11.5
Corrected b	1.6 ± 0.7	1.5 ± 0.7

Table 6.4: The expected number of tags due to non-$t\bar{t}$ sources when the $W+\geq 3$ jet sample is assumed to have some $t\bar{t}$ content. $N_{t\bar{t}}$ is the estimated number of $t\bar{t}$ events in the $W+\geq 3$ jet sample.

where N is the number of observed tags, b is the predicted background and ϵ_{top} is the acceptance for the process. The background, b, is not the same background calculated in Chapter 5. That calculation assumed the no-top quark hypothesis. The presence of $t\bar{t}$ production in the $W+\geq 3$ jet sample lowers the estimate of W events in the sample (it can be considered a non-W contribution). The background (b) is estimated by an iterative process based on the relation:

$$N = N_{t\bar{t}} \times \epsilon_{tag} + b,$$

where $N_{t\bar{t}}$ is the number of $t\bar{t}$ events in the 52 event $W+\geq 3$ jet sample. Each iteration solves for a new $N_{t\bar{t}}$. A new b is calculated by scaling the predicted background tags (2.3 ± 0.3 events for the secondary-vertex search) for the $t\bar{t}$ presence in the $W+\geq 3$ jet sample. This process is done for both the secondary-vertex and soft-lepton search. Table 6.4 lists the results. Systematic errors are large for this procedure as the backgrounds vary greatly from event to event and we do not know which events are from $t\bar{t}$ production. The systematic uncertainty for the procedure is determined by summing the predicted mistags from the tag matrix in randomly selected event samples containing $52 - N_{t\bar{t}}$ events, and using the width of the resulting distribution as the uncertainty.

A second correction must be made to the tagging efficiencies of both the SLT and secondary-vertex search efficiencies. The efficiencies do not account

M_{top}(GeV/c^2)	ϵ_{tag}^{cor}
120	0.21 ± 0.05
140	0.23 ± 0.05
160	0.23 ± 0.05
180	0.23 ± 0.05

Table 6.5: The corrected tagging efficiency. ϵ_{tag} does not take into account the probability that a non-b quark jet will be tagged in a $t\bar{t}$ event.

M_{top}(GeV/c^2)	$\sigma_{t\bar{t}}^{SVX}$ (pb)	$\sigma_{t\bar{t}}^{ALL}$ (pb)
120	$21.5^{+17.2}_{-11.3}$	$22.7^{+10.0}_{-7.9}$
140	$14.9^{+12.2}_{-7.9}$	$16.8^{+7.4}_{-5.9}$
160	$13.0^{+10.6}_{-6.9}$	$14.7^{+6.5}_{-5.1}$
180	$12.4^{+10.0}_{-6.5}$	$13.7^{+6.0}_{-4.7}$

Table 6.6: SVX cross section for four different top masses. The σ^{ALL} is calculated as described in the text. σ^{SVX} is calculated by the simple relation $n_i = \epsilon_i \cdot \int \mathcal{L}dt \cdot \sigma^{SVX}$.

for possibility of mistagging a non-b jet in a top event. This correction can be written:

$$\epsilon_{tag}^{cor} = \epsilon_{tag} + (1 - \epsilon_{tag}) \times P_{mistag}$$

where ϵ_{tag} is the tagging efficiency (calculated for the secondary-vertex search in Section 4.2), and P_{mistag} is the probability of mistagging an event. We estimate P_{mistag} to be $(1.5 \pm 0.8)\%$ for the secondary vertex search from the $-L_{xy}$ tag rate prediction in the $W+ \geq 3$ jet sample. Table 6.5 shows the corrected tagging efficiencies as a function of top mass.

Table 6.6 tabulates the cross section for each of the top masses for the SVX. The cross section changes as a function of top quark mass because the search efficiency, ϵ_{top} is a function of top mass.

The combined $t\bar{t}$ production cross section is calculated using the following

likelihood function:

$$L = e^{-\frac{(\int \mathcal{L}dt - \overline{\int \mathcal{L}dt})^2}{2\sigma_{\mathcal{L}}^2}} L_{DIL} \cdot L_{SVX} \cdot L_{SLT}$$

$$L_i = G(\epsilon_i, \overline{\epsilon_i}, \sigma_{\epsilon_i}) G(b_i, \overline{b_i}, \sigma_{b_i}) P(\epsilon_i \cdot \sigma_{t\bar{t}} \cdot \int \mathcal{L}dt + b_i, n_i),$$

where σ_i is the corrected efficiency for each search, b_i is the search's expected background (corrected by the method described earlier in this section), and n_i is the number of tags found in that search. $G(x, a, w)$ is a gaussian function evaluated at x with an average value of a and a width of w. $P(a, n)$ is a Poisson function evaluated at n with an expectation value of a. Finally, the quantities with a overline are the measured quantities, the others (except n_i) are allowed to float in the minimization. The CERN MINUIT package is used to find a minimum of $-lnL$. Systematic uncertainties are determined for each parameter by varying it such that $\Delta lnL = \frac{1}{2}$.

Figure 6.2 is the cross section shown for various top masses, along with the theory calculation. Since the acceptance for $t\bar{t}$ events varies with top mass, the calculated cross section, $\sigma_{t\bar{t}}$, varies with top mass in Figure 6.2.

6.4 Mass Determination of Tagged Events

The top quark is one of the fundamental particles in the Standard Model. In the coming years particle physicists will attempt to determine its mass and its decay modes. The current data sample is too small to do most of these studies. However, there are enough statistics to study the mass. The mass of the top quark is known to be much heavier than any of the other quarks: the current lower limit is 131 GeV/c^2[4], and the next heaviest quark is the bottom quark with a mass of 4.1 to 4.5 GeV/c^2[19]. A large top mass may

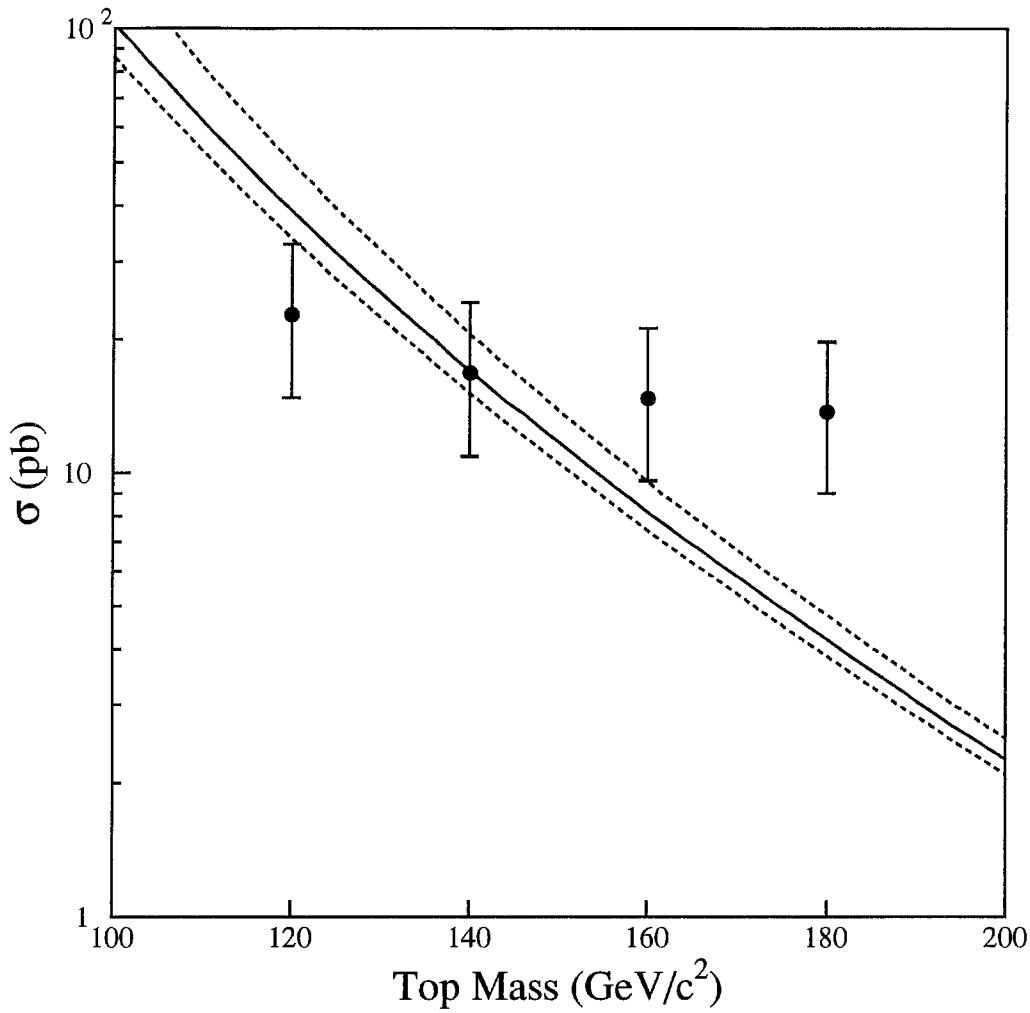

Figure 6.2: The CDF calculated $t\bar{t}$ production cross section shown as a function of top mass (points) and the theory curve (line) by Laenen et al[1]. The dashed lines represent the uncertainty in the theory calculation.

be an indication of physics outside the Standard Model. Due to radiative corrections to the W and Z masses, a measure of the W, Z, and top masses constrain the Higgs mass. This is especially important when the Higgs is discovered and its mass is measured, because the Standard Model will be over constrained. The top mass also is a parameter in many loop calculations, for example, those involving mixing in the B hadron system.

The masses of $t\bar{t}$ events are determined by a kinematic fit. The primary process

$$p\bar{p} \rightarrow t\bar{t} + X$$

can't be used directly to find the mass, as no measurements are made directly of the t-quark or the $\bar{t}$-quark. Instead, the following subprocesses are used:

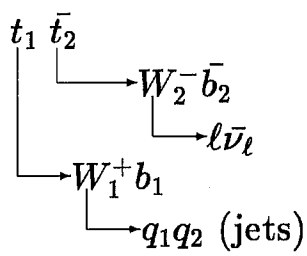

$$p\bar{p} \rightarrow t_1\bar{t}_2 + X$$

$$t_1 \rightarrow b_1 + W_1$$

$$t_2 \rightarrow b_2 + W_2$$

$$W_1 \rightarrow \ell + \nu$$

$$W_2 \rightarrow q_1 + q_2$$

where the b's represent b-quark jets, and the q's represent light quark jets. In the CDF detector b_1, b_2, q_1, q_2, ℓ, and the two component $\not{E}_T$ (which is equated with the $\bar{\nu}$) are measured. The masses of t_1 and t_2 are constrained to be the same. The W masses are also fixed at the standard 80 GeV/c^2 with a 1 GeV/c^2 uncertainty. There are 18 unknowns in this system of five constrained processes, and 20 equations. A program used to fit bubble chamber

data, SQUAW[26], is used to find the best solution to the system. Solutions are rated in terms of a fit calculated χ^2.

There are 12 ways the jets can be matched to the quarks, without b-tag information (the light quark jets can be match to either q_1 or q_2). Further, because the initial P_z of the $p\bar{p}$ collision is unknown, there is a 2-fold ambiguity in the P_z of the neutrino. This makes for a total of twenty-four possible ways to solve the system of equations in each event. The combination with the lowest χ^2 is kept. When b-tag information is used, the minimum χ^2 corresponds to the right choice of jets 31% of the time in a M_{top}=170 GeV/c^2 Monte Carlo simulation. The higher the top quark mass, the more often the correct choice of jets corresponds to a minimum in the χ^2.

Results from Monte Carlo calculations indicate that if the correct combination of jets is chosen, the mass distribution has a symmetric peak about the generated mass. The dashed histogram in Figure 6.3 shows the fit top mass in a Monte Carlo simulation at M_{top}=170 GeV/c^2 when all jets are assigned correctly. The solid histogram is the mass fit when at least one of the b-quark jets is required to be assigned correctly.

The data sample is which the top mass is fit is composed of the events tagged by the secondary-vertex and soft-lepton algorithms, a total of 10 events. As will be explained, a fourth jet is required in the fitting procedure. To increase the acceptance, the E_T requirement of the fourth jet is relaxed to 8 GeV, and the η requirement is opened $|\eta| < 2.4$. Seven tagged events have the required fourth jet. Jet corrections are applied to the data to correct for detector nonlinearities. A special set of jet corrections for b and $\bar{b}$ jets is also applied to tagged jets[2]. The individual masses for the seven tagged SVX and SLT events are listed in Table 6.7. The histogram in Figure 6.4 shows the fitted top quark masses.

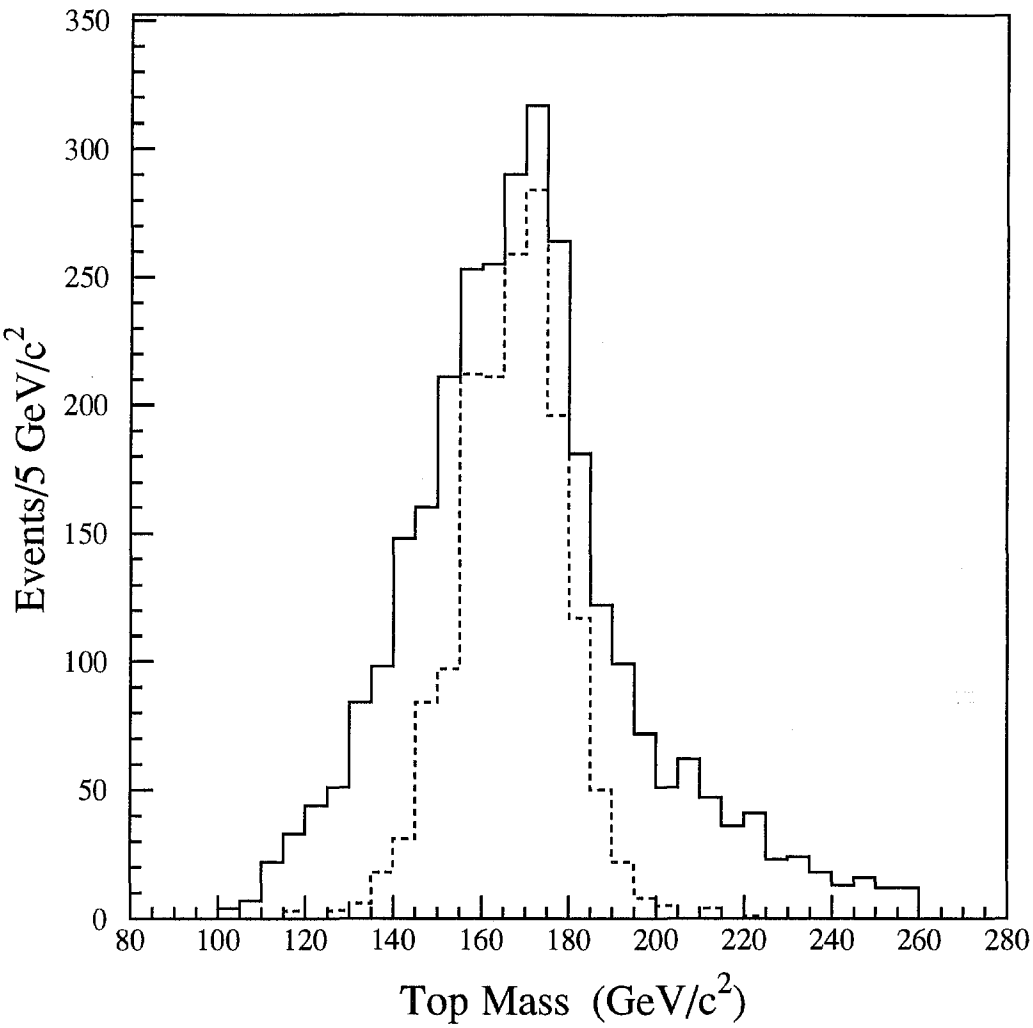

Figure 6.3: The distribution of reconstructed top mass for Monte Carlo events generated with $M_{top} = 170$ GeV/c^2. The full histogram corresponds to the best fit obtained by the fitting program when requiring that one of the b jets is a b in the fit. The dashed histogram is obtained if the correct assignment for each of the jets is made.

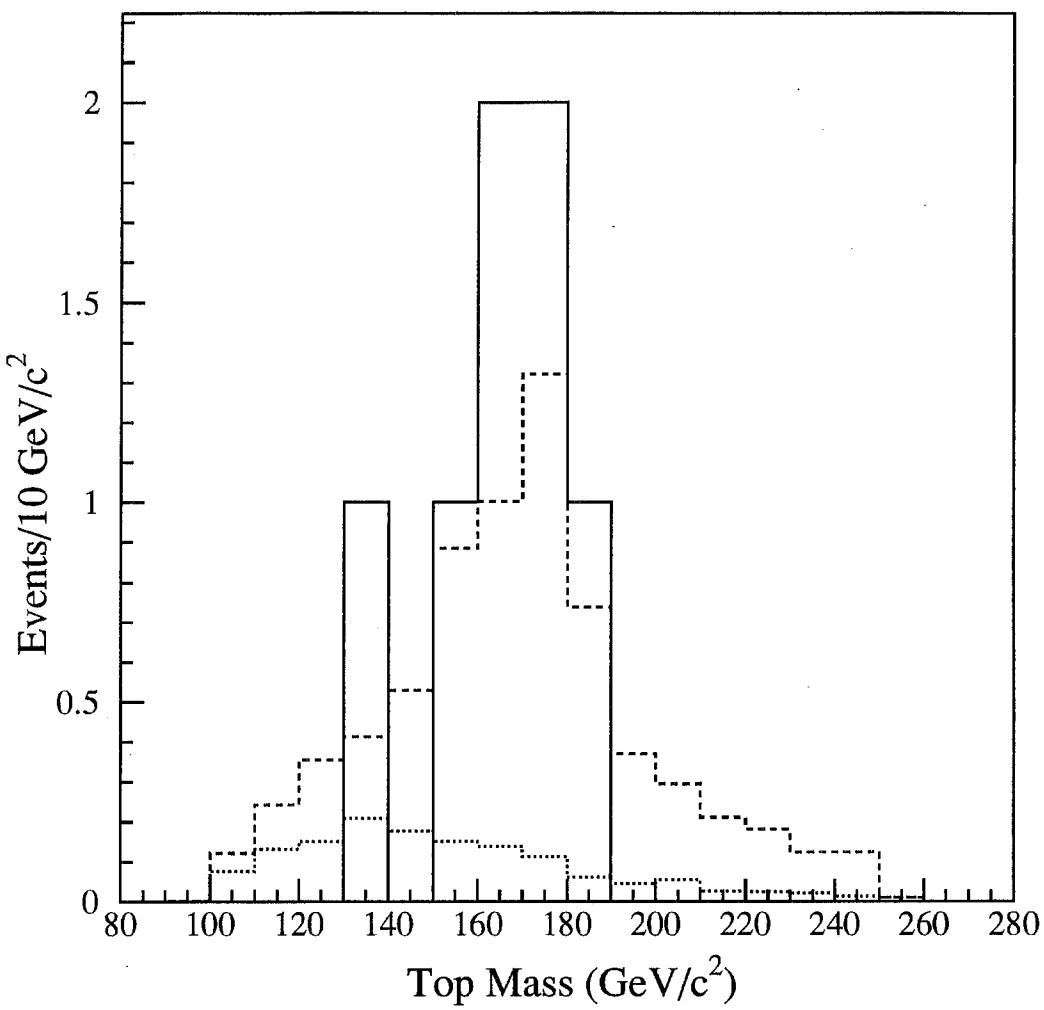

Figure 6.4: Fit top mass distribution for the data (solid histogram) and the background of 1.4 events (dots) obtained from the $W+$ multijets VECBOS events. The dashed histogram represents the sum of 5.6 $t\bar{t}$ Monte Carlo events (from the M_{top}=175 GeV/c^2 Monte Carlo simulation) plus the 1.4 background events.

Run-Event	ℓ	b-tag	Mass (GeV/c^2)	χ^2
40758-44414	e^+	SVX	172 ± 11	0.0
43096-47223	e^-	SVX	166 ± 11	2.0
43351-266423	μ^-	SLT(μ^-)	158 ± 18	6.1
45610-139604	μ^+	SVX	180 ± 9	5.0
45705-54765	e^-	SLT(e^+)	188 ± 19	0.4
45879-123158	μ^+	SLT(μ^-),SVX	169 ± 10	2.2
45880-31838	e^-	SLT(e^-)	132 ± 8	1.7

Table 6.7: The fit masses of the SVX and SLT tagged events. The run and event number are listed, along with the type of high-P_T lepton, the algorithm that tagged the jet, the mass fit and its uncertainty, and the χ^2 of the fit.

The W+jets background is fit to the $t\bar{t}$ hypothesis with SQUAW as well. The W+jets Monte Carlo sample is generated with the VECBOS program and the fragmentation is done by the HERWIG program. Many of the QCD W+4 jet events do pass the χ^2 requirement. 83% of the events have a $\chi^2 < 10$, while in $t\bar{t}$ Monte Carlo simulation, 94% of events have $\chi^2 < 10$. This means it is not possible to separate the signal and background by a requirement on χ^2 distribution alone. The fit top mass for events from W+jet Monte Carlo simulation has a broad peak at 140 GeV/c^2.

A maximum likelihood fit is used to determine the t-quark mass. For each of several simulated masses, a maximum likelihood fit determines the amount of VECBOS W+jet and $t\bar{t}$ simulated events that best fit the mass distribution of the data. The result of the maximum likelihood fit at each top mass is shown in Figure 6.5.

Sources of systematic errors are outlined in Table 6.8. The uncertainty in the jet energy scale is ±10% at 8 GeV, and ±3% at 100 GeV. Monte Carlo simulations shows the jet energy scale uncertainties translate to a ±1.8% un-

Systematic Uncertainties	(%)
Jet Energy Scale	1.8
Gluon Radiation	4.4
Different Backgrounds	$^{+5.3}_{-4.4}$
Tagging Algorithm Effects	1.4
Different Likelihood Fits	1.1

Table 6.8: The sources of systematic errors in the top quark mass determination.

certainty in the mass measurement. There is an additional contribution to the uncertainty caused by the misassignment of energies to partons in the presence of gluon radiation. This is treated as a $\pm 10\%$ effect in the jet energy, which translates to a $\pm 4.4\%$ uncertainty. The shape of the QCD W+jet background is not well known. We use four methods to model it, VECBOS with HERWIG or ISAJET fragmentation (W+3 jet generation in VECBOS), $W + 4$ jet VECBOS generation with HERWIG fragmentation, and a flat background. A 0.9% effect in the measured top mass is observed. A substantial fraction of the background originates from processes for which we have not modeled the background (see Table 5.16). A conservative approach is to assume the masses of the background are distributed evenly. We therefore eliminate two of the seven events and average the remaining five. This procedure leads to a systematic error of $+5.2\%$ and -4.4%. Possible shifts in the E_T spectra of the background and signal introduced by the SVX and SLT tagging algorithms by introducing a bias in the tagged jet energy. Monte Carlo simulation is used to show this effect introduces an uncertainty of 1.4%. Finally, changes to the likelihood procedure (alterations to the background fraction such as forcing the background fraction) as well as varying the mass range fit over introduce a 1.1% systematic error.

The minimum in the log likelyhood occurs at a top mass of $174 \pm 10^{+13}_{-10}$ GeV/c^2. At this minimum, the fraction of W+jet events in the seven is 0.16. The dashed histogram in Figure 6.4 shows the distribution of fitted top masses for a combination of 1.4 W+jet VECBOS generated events and 5.6 $t\bar{t}$ M_{top}=175 GeV/c^2 events. The dotted histogram is the distribution of fitted masses for a top mass fit of 1.4 VECBOS W+jet Monte Carlo simulation only. A final check is performed to see at what the level the data are consistent with the background-only hypothesis. The maximum log likelihood result when 100% VECBOS simulated W+jet events are fit to the data, indicates the fit is 50 times less likely than the best combination of W+jets data and best-fit top mass. Using the acceptance for the most likely top mass, the $t\bar{t}$ cross section is estimated to be $13.9^{+6.1}_{-4.8}$ pb.

6.5 Conclusion

The top quark is one of the twelve major building blocks of matter in the Standard Model, and the only one of six quarks still unobserved. Its discovery will be a major verification of the Standard Model. This thesis describes one of three CDF top quark searches that together find the first significant evidence for the top quark. This search for the top quark looks for the $t\bar{t}$ system to decay in the lepton+jets mode and, for further background rejection, looks for a b-quark using CDF's Silicon Vertex Detector. A top b-tagging efficiency of $22 \pm 6\%$ was determined using a large sample of inclusive electrons. Expected tags due to non-top sources in the signal sample are calculated by first assuming the heavy flavor rate in the W+jets sample is the same as in a generic jet sample. This is thought to be conservative. A Monte Carlo calculation verifies this, and predicts the heavy flavor content of the W+jets

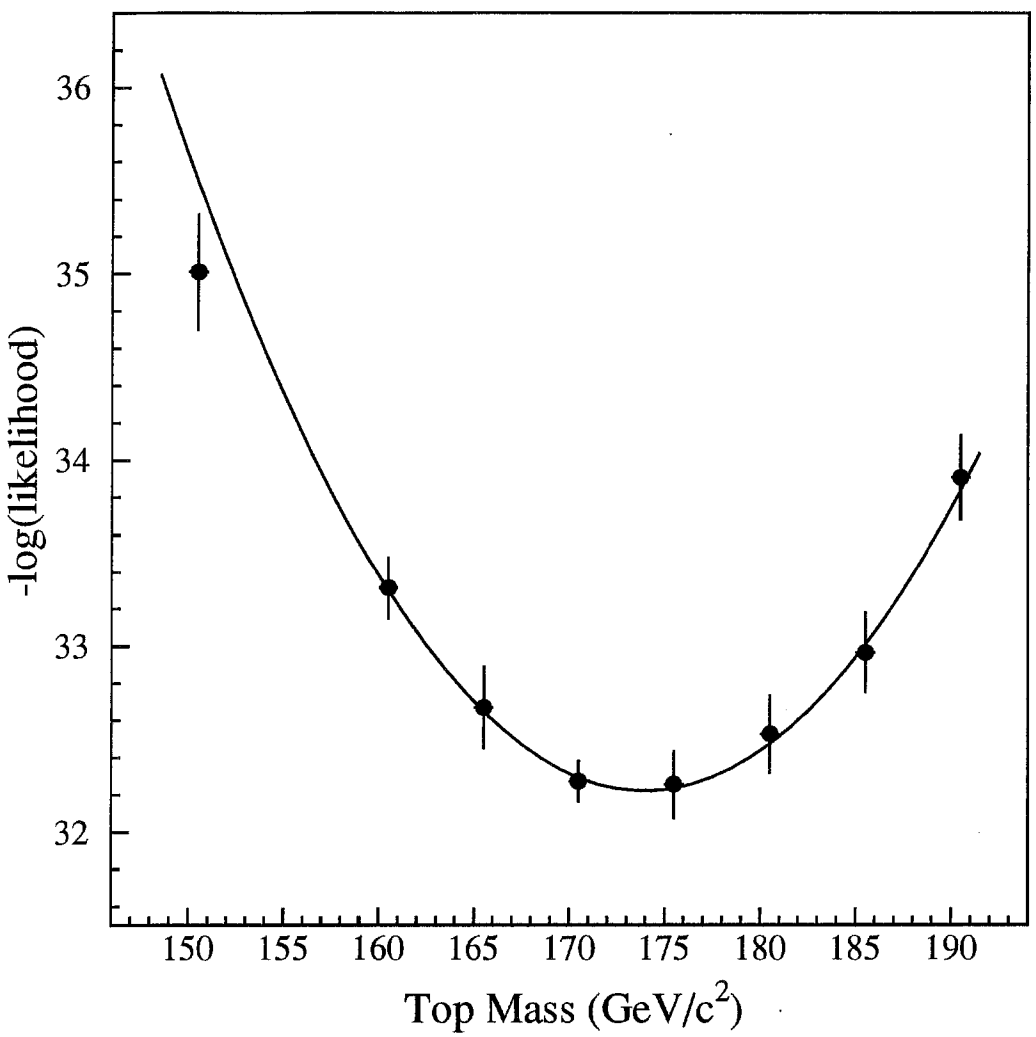

Figure 6.5: The results of the maximum likelihood fit to the top mass. The vertical error bars represent the uncertainties due to the statistics in the Monte Carlo event samples.

sample to be a factor of 3 times smaller than in generic jets. The generic jet rate is used to estimate the non-top tagging contributions due to gluon splitting ($g \rightarrow b\bar{b}$) and b-tagging mistags in the signal sample. Most other tags due to non-top sources (about 15% of the total) are carefully modeled using Monte Carlo simulations and the data-derived tagging efficiency. The total background tags expected are 2.3 ± 0.29. There is only a 3.2% chance that the background will fluctuate up to the observed 6 tags, according to Poisson statistics. When combined with other top quark search methods, there is only a .26% chance that the observed data is due to a upward fluctuation of the background. For a gaussian distribution, 0.26% probability is a 2.8σ effect. Though this isn't statistically significant enough to be interpreted as a top quark discovery, a natural interpretation is that it is evidence for the top quark's existence. The most likely mass for events tagged by the SVX and SLT algorithms is $174 \pm 10^{+13}_{-10}$ GeV/c^2, and at that mass, the CDF $t\bar{t}$ cross section is measured to be $13.9^{+6.1}_{-4.8}$ pb.

Bibliography

[1] E. Laenen, J Smith, and W.L. Van Neerven,
Phys. Lett. **321B**, 254 (1994)

[2] F. Abe *et al.*,
Phys. Rev. D **50** 2966, (1994)

[3] The discovery of the J/Ψ in 1974 (J. J. Aubert *et al.*, Phys. Rev. Lett. **33**, 1404 (1974) and J.-E. Augustin *et al.* Phys. Reb. Lett. **33**, 1406 (1974)) and the Υ (S. W. Herb *et al.*, Phys. Rev. Lett. **39** 252 (1977) and the study of the new hadron's paved the way for general acceptance of the Standard Model. The book *Introduction to Elementary Particles* by David Griffiths (John Wiley & Sons, Inc. 1987) contains a brief historical review of particle physics.

[4] The DØ Collaboration,
Phys. Rev. Lett. **72** 2138 (1994)

[5] The JADE Collaboration,
Phys. Lett. **146B**, 437 (1984).

[6] The ALEPH Collaboration,
Phys. Lett. **B263**, 325 (1991).

[7] The CLEO Collaboration,
Phys. Rev. D **35**, 3522 (1987).

[8] Rev Mod. Phys. **56**, 5296 (1984)

[9] D.O. Carlson and C.-P. Yuan, Phys. Lett.
306B, 386 (1993)

[10] Lynne H. Orr,
Phys. Rev. D **44** 88 (1991).

[11] W. Venus, Proceedings of the XVI International Symposium on Lepton-Photon Interactions, 10-15, August 1993, to be published.

[12] The CLEO Collaboration
Phys. Rev. Lett. **49** 357 (1982).

[13] M. L. Mangano,
Nucl. Phys. **B405**, 536 (1993).

[14] F. Abe *et al.*,
Fermilab Preprints Fermilab-PUB-93/232-E,
Fermilab Preprints Fermilab-PUB-93/233-E,
Fermilab Preprints Fermilab-PUB-93/234-E,
submitted to Phys. Rev. D.

[15] F. Abe *et al.*,
Nucl. Inst. Meth. Phys. Res. A **271**, 387 (1988).

[16] D. Amidei *et al.*,
Fermilab Preprints Fermilab-PUB-94/024-E,
submitted to Nucl. Inst. Meth. Phys. Res.

[17] F. Abe *et al.*, Phys. Rev. D **45**, 1448 (1992).

[18] P. Avery, K. Read, G. Trahern,
Cornell Internal Note CSN-212, March 25, 1985 (unpublished).

[19] The Particle Data Group,
Phys. Rev. D **45**, Part 2 (1992).

[20] F. Abe *et al.*,
Phys. Rev. D **44**, 29 (1991).

[21] B. Winer and P. Koehn
CDF Internal Publication 1876.

[22] The estimates are derived using the next-to-leading order calculation described in M.L. Mangano, P. Nason, and G. Ridolfi,
Nucl. Phys. **B373** 295 (1992).

[23] G. Watts *et al.*,
CDF Internal Publication 2471.

[24] F. Abe *et al.*,
Phys. Rev. Lett. **73** 220 (1994).

[25] J. Ohnemus *et al.*, Phys. Rev. D **44**, 1403 (1991);
Phys Rev D **44** 3477 (1991);
S. Frixione, Nucl. Phys. **B410**, 280 (1993);
S. Frixione, P. Nason, and G. Ridolfi, Nucl. Phys. *B383*, 3 (1992).

[26] O. Dahl, T. Day, F. Solmitz, and N. Gould *SQUAW, Kinematic Fitting Program*, Lawrence Berkeley Laboratory, Group A Programming Note P-126, July 1968

Appendix A

SVX Cooling and Interlock Subsystems

The Silicon Vertex Detector is located at the very center of the CDF detector. The large number of channels in each barrel, about 20,000, requires some data processing to take place on the detector. Unhit channels are not read out (zero suppression), pedestal subtraction is performed, and data readout is multiplexed. The analog signal is also amplified on the silicon, thus reducing a signal-to-noise ratio that might otherwise be large if the signal were to be read out of the detector unamplified. The onboard electronics generates 50 watts of heat on each barrel. Though there is some gas flow to carry away the heat, it is not enough. Instead, a water cooling system, with cooling tubes mounted on the bulkhead of the SVX detector, is used to carry away the heat. Figure A.1 is a schematic diagram of the water cooling system for the SVX. Water is cooled in a Neslab CFT 25 recirculating chiller, which is mounted on the face of the plug calorimeter. The water is filtered as it exits the chiller. Most of the water is returned directly to the chiller via a bypass loop. The returned water passes through a deionizer, which prevents a second path to ground through

the water. The water that does not return through the bypass valve flows through the SVX valve and into a gas heat exchanger (to cool the gas around the SVX) and finally through the SVX. The SVX valve, also mounted on the face of the plug calorimeter, is used to remotely control the water flow into the SVX. The water exiting the SVX returns to the chiller reservoir, joining the water from the deionizer. The flow rate through the SVX is $\sim$ 1 gallon per hour.

A key feature of the SVX cooling system is that at no point in the system is the pressure greater than atmospheric pressure. This means that any small leak will draw air into the system, instead of pushing water out. This is important as cooling pipes are located along the inside of the SVX as well as the outside of the VTX detector, near the VTX detector's high voltage wires. The main water reservoir is the low pressure point, and is maintained at 3.1 PSIA (pounds per square inch absolute) by an oilless roughing pump. Independence from pressure changes due to weather systems is maintained by referencing the vacuum system to a constant 5 PSIA nitrogen source. The highest pressure point in the system is the entrance to the SVX and is maintained close to 10.5 PSIA by the SVX valve (atmospheric pressure is 14.7 PSIA).

The SVX cost one million dollars in parts; much more when labour is factored in. It also runs water near the VTX which operates at 2000 volts. The investment in time and potential damage require an interlock system to monitor the SVX, prevent unsafe usage, and protect against accidents.

The interlock system is designed to require minimal human intervention; only during SVX power up and ramp down is operator attention required. Further, turning the power on of the SVX requires checking a key out from shift personal in the CDF main control room (with the shift capitan's knowledge). Figure A.2 is a functional schematic of the SVX interlock system.

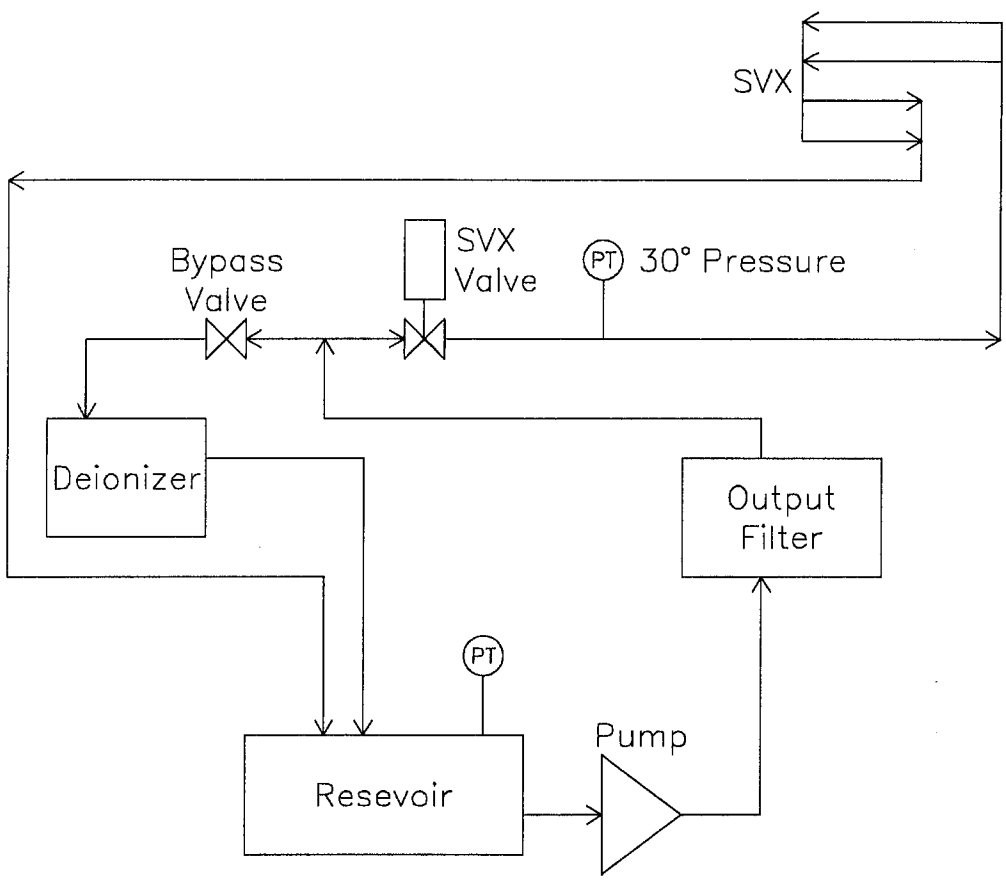

Figure A.1: A schematic diagram for one barrel of the SVX water cooling system. About 1.5 gallons of water are held and cooled to 9°C in the reservoir. The cold water is pumped through a filter, and to the bypass and SVX valves. Most of the water travels through the bypass valve, the deionizer, and returns to the reservoir. A small amount of water travels through the SVX valve and into the SVX carrying away heat generated by the electronics. Pressures are measured (transducers are marked by the PT symbol) in the reservoir and just before the entrance to the SVX.

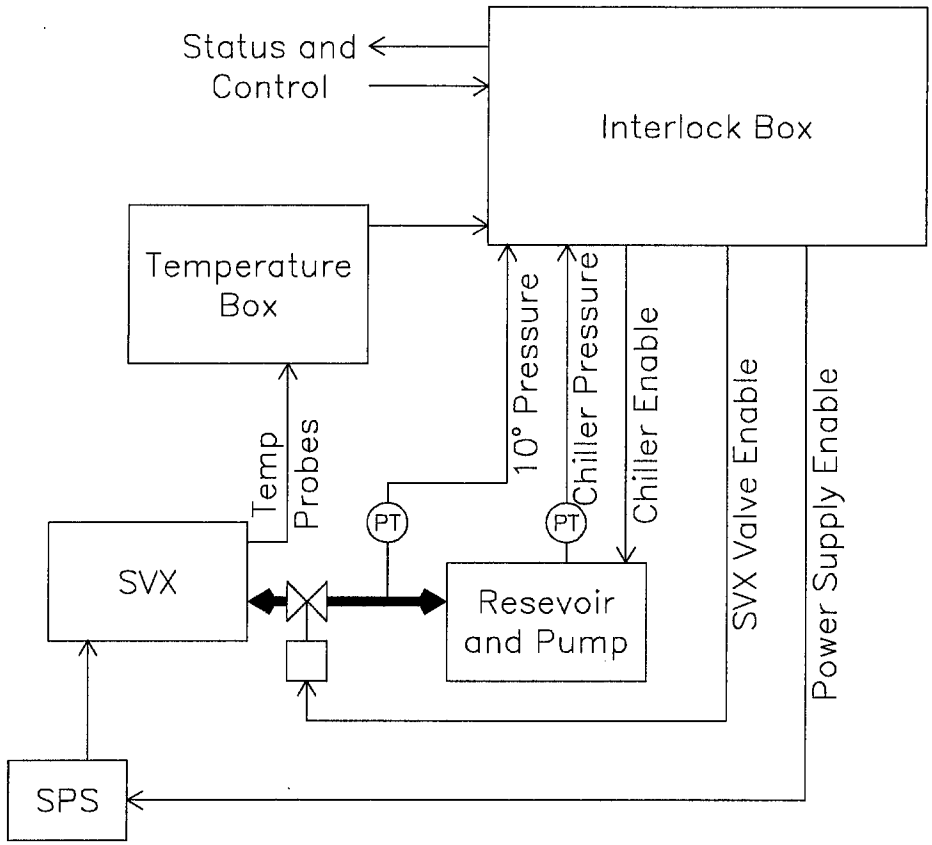

Figure A.2: Functional schematic of the SVX interlock system. The interlock system is controlled by a TI 435 RLL processor, labeled the "Interlock Box" here. It monitors SVX temperatures and pressures, and controls enables for the SVX power supplies, the SVX valve, and the chiller pump. The temperatures are measured by current devices, and the currents are converted to voltages by the "Temperature Box". Status lights and a key switch are the user interface. There is one system for each barrel, though the barrels share the Interlock Box and the Temperature Box.

The interlock system is designed to protect against the two potential catastrophes: temperature extremes and water leaks. The interlock system generates an *enable* to power the SVX wedge power supplies (SPS supplies), an enable to allow the chiller to operate, and an enable that allows the SVX valve be to opened. The 50 watts of heat generated by the onboard electronics would cause the temperature to quickly rise to a level that could damage the port card and ear electronics if the cooling were to be shut off while power remained on. Twelve AD 592C temperature sensors are used to monitor the temperature, and are distributed along the four layers of silicon as well as the beryllium bulkheads, near the heat sources (the port cards). The AD 592C varies the current as a function of temperature. The current is converted into a voltage for readout purposes by the Rochester Temperature Conversion Box. Five of the temperatures on each barrel are monitored by the interlock system, and if more than two sensors are outside the operating range of 12°C to 35°C, the SPS supply enable is removed.

Water leaks are detected by monitoring the pressure of the cooling system. Both the chiller pressure and the pressure at the entrance to the SVX (the 10° hole) are monitored. When a leak occurs the chiller pressure will slowly rise from its nominal value of 3.1 PSIA. The interlock system allows the reservoir pressure to vary between 2.4 PSIA and 3.4 PSIA before removing the SVX valve and chiller enables. The 10° hole pressure tends to vary much more during the normal course of operation, and is allowed to vary between 8.5 and 13.5 PSIA about its nominal value of 10.5 PSIA before the SVX valve and chiller enables are removed.

An orderly and safe shutdown of SVX should be possible if any single part of the cooling or interlock system fails: the system is designed to be single-mode failure-tolerant. All the controls are designed to be fail safe. When

a cable is severed or accidentally unplugged, enables to the power supplies, chiller, and valve will be removed and the devices will turn off.

The CPU for the interlock system is the Texas Instruments series 405 controller. Run by a model TI 435 central processing unit, this same system is used on many factory floors to automate manufacturing equipment and assembly lines. The TI 435 is programmable, via an attached IBM compatible computer. The TI 435 is programmed with the Relay Ladder Logic (RLL) language.

The 405 system has an expandable number of inputs and outputs. The system is configured with 24 analog inputs (0-5 volt range, 1.2 mV resolution), 16 logic inputs, 32 logic outputs, and 16 relays (not all devices are used). The relay outputs are used for the fail-safe control of the enable signals. Initial development and testing was quick and program maintenance has been very easy. The biggest feature added after the start of the run was to accommodate noise in the pressure sensors due to Motorola walkie-talkies. Other maintenance of the system has been minimal.